Investigating the Aeroacoustic Performance of the Partially Averaged Navier-Stokes Method

TECHNISCHE
UNIVERSITÄT
DARMSTADT

Fachbereich Maschinenbau

Fachgebiet Numerische
Berechnungsverfahren im
Maschinenbau

Investigating the Aeroacoustic Performance of the Partially Averaged Navier-Stokes Method

Accepted doctoral thesis by Arezoo Moosavifard

Date of submission: 28. November 2023
Date of thesis defense: 31. Januar 2024

Darmstadt, Technische Universität Darmstadt, 2024

Acknowledgments

It is with great pleasure that I present this doctoral thesis, the result of four years of research at the Institute of Numerical Methods in Mechanical Engineering (FNB) at the Technical University of Darmstadt. I extend my deepest gratitude to the remarkable individuals who have influenced my academic journey.

I extend my special appreciation to my supervisor, Professor Dr. rer. nat. Michael Schäfer, for providing me with the opportunity to contribute to the FNB. His support and trust in my work played a crucial role in shaping this research, and his guidance has been invaluable throughout the entire process. I am also thankful for the constructive advice provided by my co-referee, Apl. Prof. Dr.-Ing. habil. Suad Jakirlic, which significantly enhanced the quality of my work.

Sincere thanks are extended to Dr.-Ing. Elena Kolb for her consistent support and thorough proofreading of this thesis. Gratitude is also expressed to Peyman Rostami and Helge Meyer for their helpful proofreading. Special thanks goes to Felix Köhler for his guidance, particularly during the early stages of my research. I appreciate the collaborative and pleasant working atmosphere fostered by the FNB and CPS group. I would like to acknowledge Monika Müller, Carina Schuster, and Dr. Markus Lazanowski for their administrative support, and Michael Fladerer and Christian Schmitt for their assistance with IT-related challenges crucial to the seamless progress of my research.

My family and friends have been a constant source of support, and I am deeply grateful. I extend my deepest gratitude to my parents and my brother, Armin, for their unconditional support and constant presence. I am also thankful for my friends, Fateme Koohkan and Mahsa Gholami, who have always been there for me. Lastly, my heartfelt thanks are reserved for my husband, Iman Valizadeh, whose support and encouragement have been the driving force behind my entire PhD journey. Without the support from all of you, I would not be in the place I am today.

I acknowledge the support of the German Academic Exchange Service (DAAD) through the Graduate School of Computational Engineering Scholarship Programme at the Technical University of Darmstadt, and the role of the Lichtenberg high-performance computer at TU Darmstadt, where calculations for this research were conducted.

Abstract

Aeroacoustics is the field of research dedicated to studying the generation and propagation of sound resulting from the interaction of unsteady flows with solid structures, such as aircrafts and automobiles. As the demand for quieter vehicles continues to rise and the negative impacts of noise pollution on human well-being become more evident, it is crucial to develop accurate and efficient methods for predicting and controlling aerodynamic noise. Computational Aeroacoustics (CAA), which unites theoretical and computational techniques, has emerged as a powerful approach to effectively address these challenges.

The success of CAA relies heavily on Computational Fluid Dynamics (CFD), a numerical simulation method for studying fluid flow and its characteristics. Given the intricate interplay between unsteady flows and solid structures, it is essential to employ reliable CFD methods that capture the underlying flow dynamics and its acoustic consequences with precision. Turbulence, a common occurrence in real-world flows, plays a vital role in sound generation by inducing fluctuations and instabilities that contribute to aerodynamic noise. Among various CFD methods, Reynolds-Averaged Navier-Stokes (RANS) and Large Eddy Simulation (LES) are widely utilized for simulating turbulent flows. However, RANS models, while computationally efficient, have limitations in accurately capturing unsteady flow phenomena critical for aeroacoustic predictions. On the other hand, LES provides a more accurate representation of unsteady flow features, but its practical application is constrained by substantial computational resource requirements.

To address the limitations of RANS and LES, researchers have developed hybrid LES/RANS methods that seek to balance computational cost and accuracy by utilizing the strengths of both approaches. One prominent hybrid method is the Partially-Averaged Navier-Stokes (PANS) method, which offers a compromise between computational efficiency and the ability to capture unsteady flow phenomena. By incorporating dynamic resolution parameters and suitable turbulence models, such as the $k - \epsilon - \zeta - f$ model equation, the PANS method aims to provide a more accurate representation of flow and its acoustic characteristics.

This research focuses on investigating the aeroacoustic performance of the SSV-PANS method, a specific variant of the PANS method, by comparing it to a reference LES. The assessment considers both computational accuracy and costs. The research employs a hybrid approach, decomposing fluid variables into incompressible hydrodynamic and compressible perturbation

equations to enable the study of aerodynamic noise. The SSV-PANS method is used to compute aeroacoustic sources from the incompressible flow field.

To validate the accuracy and computational efficiency of the SSV-PANS method, extensive analyses are conducted on the flow around a circular cylinder and an Ahmed body—renowned benchmark cases in Computational Fluid Dynamics (CFD). Results obtained using the SSV-PANS method are compared against those obtained from LES as well as experimental measurements.

By advancing the understanding and capabilities of CAA methods through the evaluation of the SSV-PANS method, this research contributes to the development of quieter vehicles with reduced noise emissions. Improving the accuracy and efficiency of computational methods facilitates the optimization of vehicle designs, enabling effective noise pollution mitigation and the creation of sustainable and healthier communities.

Zusammenfassung

Aeroakustik ist ein Gebiet, das sich mit der Erzeugung und Ausbreitung von Schall beschäftigt, der durch die Wechselwirkung von instationären Strömungen mit festen Strukturen wie Flugzeugen und Autos entsteht. Da die Nachfrage nach leiseren Fahrzeugen weiter steigt und die negativen Auswirkungen von Lärmbelastung auf das menschliche Wohlbefinden zunehmen, ist es entscheidend, genaue und effiziente Methoden zur Vorhersage und Kontrolle von aerodynamischem Lärm zu entwickeln. Die Numerische-Aeroakustik (CAA), die theoretische und rechnerische Techniken vereint, hat sich als ein mächtiger Ansatz etabliert, um diese Herausforderungen effektiv anzugehen.

Der Erfolg der CAA hängt stark von der Computational Fluid Dynamics (CFD) ab, einer numerischen Simulationstechnik zur Untersuchung von Strömungsverhalten und ihren Eigenschaften. Angesichts des komplexen Zusammenspiels von instationären Strömungen und festen Strukturen ist es wesentlich, zuverlässige CFD-Methoden einzusetzen, die die zugrunde liegende Strömungsdynamik und ihre akustischen Auswirkungen präzise erfassen. Turbulenzen, die in realen Strömungen häufig auftreten, spielen eine entscheidende Rolle bei der Schallerzeugung, indem sie Schwankungen und Instabilitäten verursachen, die zum aerodynamischen Lärm beitragen. Unter den verschiedenen CFD-Methoden werden Reynolds-Averaged Navier-Stokes (RANS) Methoden und Large Eddy Simulation (LES) weit verbreitet zur Simulation turbulenter Strömungen eingesetzt. Allerdings haben RANS-Modelle, obwohl sie rechnerisch effizient sind, Einschränkungen bei der genauen Erfassung von instationären Strömungsphänomenen, die für aeroakustische Vorhersagen entscheidend sind. Auf der anderen Seite bietet LES eine genauere Darstellung instationärer Strömungsmerkmale, jedoch ist die praktische Anwendung durch erhebliche Anforderungen an Rechenressourcen eingeschränkt.

Um die Einschränkungen von RANS und LES zu adressieren, haben Forscher hybride LES/RANS-Methoden entwickelt, die versuchen, den Kompromiss zwischen Rechenkosten und Genauigkeit durch die Nutzung der Stärken beider Ansätze zu finden. Eine prominente hybride Methode ist die Partially-Averaged Navier-Stokes (PANS) Methode, die einen Kompromiss zwischen Recheneffizienz und der Fähigkeit, instationäre Strömungsphänomene zu erfassen, bietet. Durch die Verwendung dynamischer Auflösungsparameter und geeigneter Turbulenzmodelle wie der $k - \epsilon - \zeta - f$-Modellgleichungen zielt die PANS-Methode darauf ab, eine genauere Darstellung der Strömung und ihrer akustischen Eigenschaften zu liefern.

Die vorliegende Arbeit konzentriert sich darauf, die aeroakustische Leistung der SSV-PANS-Methode, einer spezifischen Variante der PANS-Methode, zu untersuchen, indem sie sie mit einer Referenz LES vergleicht. Die Bewertung berücksichtigt sowohl die Berechnungsgenauigkeit als auch die Kosten. Die Methodik verwendet einen hybriden Ansatz, in dem die Fluidvariablen in inkompressible hydrodynamische und kompressible Störungsgleichungen aufgeteilt werden, um die Untersuchung von aerodynamischem Lärm zu ermöglichen. Die SSV-PANS-Methode wird verwendet, um aeroakustische Quellen aus dem inkompressiblen Strömungsfeld zu berechnen.

Um die Genauigkeit und Recheneffizienz der SSV-PANS-Methode zu validieren, werden umfangreiche Analysen zur Strömung um einen kreisförmigen Zylinder und einen Ahmed-Körper durchgeführt - bekannte Benchmark-Fälle in der Computational Fluid Dynamics (CFD). Die mit der SSV-PANS-Methode erzielten Ergebnisse werden mit denen aus der LES sowie experimentellen Messungen verglichen.

Indem das Verständnis und die Fähigkeiten von CAA-Methoden durch die Bewertung der SSV-PANS-Methode vorangetrieben werden, trägt diese Forschung zur Entwicklung leiserer Fahrzeuge mit reduzierten Lärmemissionen bei. Die Verbesserung der Genauigkeit und Effizienz von Berechnungsmethoden ermöglicht die Optimierung von Fahrzeugdesigns, um effektive Lärmbekämpfung zu ermöglichen und nachhaltige und gesündere umstände zu schaffen.

Contents

List of Figures

List of Tables

1 Introduction

1.1 Motivation

In recent years, the field of aeroacoustics has become increasingly crucial in the design of high-speed vehicles as it addresses the pressing challenge of reducing noise emissions. The impact of aerodynamic noise generated by vehicles not only affects the well-being of individuals living near transportation corridors but also contributes significantly to overall noise pollution levels. Consequently, there is an urgent need to develop advanced methods capable of accurately predicting and controlling this noise phenomenon.

To tackle this challenge, Computational Aeroacoustics (CAA) has emerged as a promising approach, offering cost-effectiveness and versatility through computational methods. Hybrid methods, specifically employed for predicting aerodynamic noise at low Mach numbers, have gained widespread acceptance. These methods involve decomposing fluid variables into an incompressible flow field and compressible perturbation equations, connecting them through acoustic sources.

However, additional research is required to investigate novel approaches that achieve an improved equilibrium between computational efficiency and accuracy, specifically for intricate flow structures and complex geometries. The effectiveness of Computational Aeroacoustics (CAA) relies on the study of fluid flow through Computational Fluid Dynamics (CFD), where turbulence plays a crucial role in sound generation. The limitations of Reynolds-Averaged Navier-Stokes (RANS) models and the resource-intensive nature of Large-Eddy Simulation (LES) have led to the development of hybrid LES/RANS methods. The Partially-Averaged Navier Stokes (PANS) method, among these approaches, shows great promise with its ability to combine the strengths of both methods.

The PANS method represents a continuous hybrid approach that seamlessly transitions from Reynolds-Averaged Navier-Stokes (RANS) to Direct Numerical Simulation (DNS), providing improved accuracy while retaining computational efficiency. By decomposing the velocity field based on kinetic energy rather than a wave number cutoff, the PANS method offers a more faithful representation of underlying flow structures, particularly in regions characterized by flow separation or turbulence.

Leveraging the capabilities of computational fluid dynamics solver FASTEST [1], a finite-

volume solver for simulating complex flows, which is used for the implementation of the SSV-PANS method demonstrates significant promise in the realm of aerodynamic field prediction. Therefore, it is of great interest to study the applicability of this method in the field of aeroacoustics.

Among the various PANS methods, the SSV-PANS method stands out as a notable extension, incorporating an additional equation for the resolved kinetic energy. The observed promising results of the SSV-PANS method in the field of aerodynamics led to its implementation in the FASTEST [1] computational fluid dynamics solver, renowned for its ability to simulate complex flows using a finite-volume approach, with the specific intention of evaluating its performance in the realm of aeroacoustics. By bridging the gap between accurate representation and computational efficiency, this research aims to establish the SSV-PANS method as a reliable tool for predicting aeroacoustic phenomena, contributing significantly to the development of noise-reduced vehicles. Through this advancement, the primary objective of this research is to pave the way for quieter and more environmentally sustainable transportation systems, enriching the quality of living environments for individuals and communities.

1.2 State of the Art

This section provides a comprehensive analysis of the current state of Computational Aeroacoustics (CAA) and Turbulence Modeling. These fields are essential for accurately predicting aerodynamic noise from turbulent flows in various applications. The section discusses the numerical methods used in CAA to study how sound is generated and propagates in fluid motion. By reviewing the latest techniques and advancements, the aim is to provide a clear understanding of the progress and challenges in CAA and Turbulence Modeling. Ongoing research focuses on improving the accuracy and efficiency of aeroacoustic simulations, which can help address complex noise-related issues effectively.

Turbulence Modeling

Turbulent flows play a critical role in various industrial and engineering applications, especially in computational aeroacoustics. The accurate prediction and understanding of turbulence are vital for designing efficient engineering systems. To address this need, different methods have been developed to capture and characterize turbulence in distinct ways. DNS is a highly accurate method that simulates turbulent flows by directly solving the Navier-Stokes equations without employing additional modeling [2, 3]. However, the computational cost associated with DNS restricts its usage primarily to academic research and problems within a limited range of scales. As the Reynolds numbers increase, DNS becomes impractical for most engineering applications due to the substantial increase in the number of grid points required [4].

Large Eddy Simulation (LES) proposed by Smagorinsky [5], is an accurate computational method that aims to resolve the larger-scale motions of turbulence while modeling the smaller-scale motions using sub-grid scale (SGS) models. LES accurately captures the energy-containing structures of turbulence while representing the unresolved turbulent eddies through SGS models. The widely used Smagorinsky model employs a fixed value for the Smagorinsky constant to approximate the SGS turbulence. However, this fixed constant may introduce errors when dealing with flows exhibiting varying turbulence intensities. To address this limitation, Germano et al. [6] introduced a dynamic Smagorinsky model that adapts the Smagorinsky constant during the simulation based on the local flow properties, resulting in improved accuracy and better representation of the turbulent flow dynamics.

Reynolds-Averaged Navier-Stokes (RANS) models are widely used in computational fluid dynamics to simulate turbulent flows [7]. By solving the time-averaged RANS equations, RANS models capture the mean behavior of the flow while incorporating turbulence models to account for the effects of turbulent fluctuations. While computationally less demanding than other methods like LES and DNS, RANS models may exhibit lower accuracy, especially in flows with complex geometries and high turbulence intensity.

Hybrid Reynolds-Averaged Navier-Stokes/Large Eddy Simulation (RANS/LES) models aim to leverage the strengths of both RANS and LES methodologies. These models effectively resolve the large-scale structures of turbulence while simultaneously modeling the smaller-scale structures. Several approaches to hybrid RANS/LES modeling have been developed, including Detached Eddy Simulation (DES) [8, 9], Very Large Eddy Simulation (VLES) [10], Limited Numerical Scales (LNS) [11, 12], and Partially-Averaged Navier-Stokes (PANS) [13, 14].

The Partially-Averaged Navier-Stokes (PANS) method, proposed by Girimaji [13, 14], offers a robust framework that facilitates a seamless transition from RANS to DNS by decomposing the velocity field based on its kinetic energy. This decomposition ensures a balanced representation of resolved and modeled kinetic energy, leading to improved accuracy in capturing flow dynamics. Validation studies conducted on complex flows have demonstrated the effectiveness of PANS in industrial scenarios [15–17].

The PANS closure model, derived from RANS equations, incorporates the ratios of unresolved-to-total kinetic energy (f_k) and dissipation (f_ϵ). This formulation allows PANS to simulate a wide range of behaviors, covering both DNS-like and RANS-like behavior.

By combining the strengths of RANS and LES, PANS bridges the gap between accurately representing turbulence dynamics and handling complex geometries. The method has gained significant interest in the Computational Fluid Dynamics (CFD) research community, as evidenced by numerous studies conducted by researchers such as [18–23].

The PANS model, initially derived from the $k - \epsilon$ model, has been enhanced through two additional variants: one based on the $k - \omega$ formulation [24] and another based on the $k - \epsilon - \zeta - f$ model proposed by Basara et al. [25]. Basara et al. [25] introduced a near-wall

formulation for the PANS model, improving its performance in capturing near-wall turbulence effects. Their findings demonstrate the effectiveness of this formulation in accurately predicting complex flow phenomena near solid boundaries, advancing the reliability of PANS for analyzing turbulent flows.

In turbulent flow simulation, the determination of the cut-off resolution parameter is crucial in bridging methods. Basara et al. [26] presented a new approach to address this challenge by introducing the Scale-Supplying Variable (SSV) equation. This equation corrects the modeling of unresolved scales in turbulent flows and accurately determines the cut-off resolution parameter. By incorporating the SSV equation, researchers and engineers can achieve enhanced accuracy in capturing turbulent flow dynamics across various applications. The significance of the SSV equation lies in its ability to refine the modeling of unresolved scales, leading to more reliable predictions and deeper insights into the complex behavior of turbulent flows. Building upon our understanding of turbulent flow simulation and turbulence modeling, the next section explores Computational Aeroacoustics (CAA).

Computational Aeroacoustics

Aeroacoustics is a significant area of research with wide-ranging implications in various industries, particularly in the design of quieter vehicles. While experimental methods have traditionally played a role in investigating aeroacoustic phenomena, computational approaches have gained prominence due to their cost-effectiveness and ability to provide detailed insights into complex flow dynamics. Computational Aeroacoustics (CAA) has witnessed substantial advancements in recent decades, benefiting from progress in computational fluid dynamics (CFD) and computational acoustics, and finding widespread applications in industry and academia.

The foundations of CAA can be attributed to the seminal work of Lighthill, who introduced the acoustic analogy by reformulating the compressible Navier-Stokes equations into an inhomogeneous wave equation [27, 28]. Building upon Lighthill's breakthrough, other methodologies such as Curle's formulation [29] and the Ffowcs Williams-Hawkings (FW-H) formulation [30] were developed to address the limitations of the acoustic analogy, particularly in relation to stationary and moving solid bodies.

Computational Aeroacoustics encompasses a range of numerical techniques, broadly classified into two groups: direct methods and hybrid methods. Direct noise computation (DNC) methods involve solving the complete compressible flow equations without additional model approximations, making them particularly useful for analyzing highly nonlinear aeroacoustic phenomena [31, 32]. However, these methods require significant numerical resolution, rendering them inefficient for aeroacoustic problems involving low Mach number flows [33].

on the other hand, hybrid methods address the multiscale nature of aeroacoustic problems by decoupling fluid dynamics and acoustic simulations. These methods first compute the unsteady

flow field using computational fluid dynamics (CFD) schemes capable of resolving essential turbulent flow structures. Subsequently, they determine the acoustic field using acoustic sources derived from the unsteady flow field. This class of methods includes hydrodynamic/acoustic splitting methods [34, 35] and acoustic analogies.

Hydrodynamic/acoustic splitting methods are integral to Computational Aeroacoustics (CAA) as they enable the separation of hydrodynamic and acoustic components, facilitating efficient and accurate simulations of sound generation and propagation in fluid motion. By decomposing the fluid variables into hydrodynamic and acoustic parts, these techniques allow for the independent solution of the respective equations governing each component. This enhances computational efficiency by accommodating specific resolution and domain requirements.

Notably, Seo and Moon [36] proposed linearized perturbed compressible equations for predicting aeroacoustic noise at low Mach numbers, while Hardin and Pope [34] introduced an acoustic/viscous splitting technique widely used in aerospace applications to predict aerodynamic noise. Shen and Sørensen [37, 38] derived the Linearized Euler Equations (LEE) that govern aeroacoustic quantities.

The hybrid approach, incorporating acoustic analogies like Lighthill's, Curle's, and FW-H analogy, provides a cost-effective computational solution compared to direct noise computation, making it suitable for industrial applications. On the other hand, it should be noted that acoustic analogies, despite their widespread use, are not completely satisfactory for accurately capturing aeroacoustic phenomena.

Overall, while direct methods are well-suited for analyzing highly nonlinear aeroacoustic phenomena, hybrid methods are better suited for low Mach number flow problems. However, the choice of method depends on the specific characteristics of the problem at hand, and a universally applicable approach for obtaining acoustic information efficiently and accurately is currently unavailable. Ongoing research in Computational Aeroacoustics (CAA) is dedicated to improving the accuracy and efficiency of aeroacoustic simulations.

To reduce computational costs, unresolved turbulence scales are often represented using turbulence models instead of performing DNS. Baily and Juvé [39] integrated the $k - \epsilon$ RANS turbulence model with the LEE method, despite its limitations for aeroacoustic problems. The LES model has also been employed to calculate aeroacoustic sources [40]. While LES serves as a cost-effective alternative to DNS for turbulent noise evaluation [41], the significance of hybrid LES/RANS methods persists in striking a balance between accuracy and computational efficiency. In this regard, Langtry et al. [42] explored the use of the Detached Eddy Simulation (DES) model for simulating flap edge noise, contributing to the development of hybrid LES/RANS approaches.

The current research builds upon the work of Hardin and Pope [34] and adopts a splitting approach based on the formulation presented by Kornhaas et al. [40]. However, Kornhaas et

al. [40] calculated aeroacoustic sources based on LES, while the current research utilizes the Partially-Averaged Navier-Stokes (PANS) method, specifically the SSV-PANS method, to find a more efficient alternative to the extensive computational requirements of the LES model. This poses a challenge for the widespread adoption of LES in Computational Aeroacoustics (CAA) for engineering problems.

Additionally, several methods can be employed to further enhance computational efficiency. In the current study, the hydrodynamic/acoustic splitting approach is utilized to effectively handle acoustic waves in the nearby and intermediate regions. Simultaneously, the Kirchhoff method enables the determination of acoustic pressure at any given position in the far field. The combination of perturbation equations with wave extrapolation methods presents a promising opportunity for efficient assessment of sound in the far field [36, 43–45].

The field of Computational Aeroacoustics (CAA) is continually advancing, fueled by the need for precise and efficient noise prediction methods. Through the combination of direct methods, hybrid approaches, and innovative techniques, researchers and engineers can gain valuable insights into the generation and propagation of noise in fluid dynamics. Ongoing research in CAA aims to enhance the accuracy and efficiency of aeroacoustic simulations, providing valuable tools for understanding and addressing various aeroacoustic problems. One interesting approach in this regard is to investigate the performance of SSV-PANS based on the $k - \epsilon - \zeta - f$ model in the context of aeroacoustics using the acoustic/viscous splitting technique. This investigation holds promise for advancing our understanding and capabilities in aeroacoustic analysis and design.

1.3 Objectives and Outline

This thesis endeavors to enhance Computational Aeroacoustics (CAA) methods by evaluating the capabilities of the SSV-PANS method for aerodynamic noise prediction in comparison to a reference Large Eddy Simulation (LES) model. The primary objective is to improve the accuracy and efficiency of CAA techniques to facilitate quieter vehicles and effective noise pollution mitigation.

In Chapter 2, the computational fluid dynamics (CFD) and computational aeroacoustics (CAA) tools utilized to simulate the flow and acoustics around bluff bodies are thoroughly explained. Furthermore, the SSV-PANS approach is introduced. This chapter serves as a fundamental basis for comprehending the numerical methods employed throughout the present study.

Chapter 3 comprehensively explores turbulent flow simulation methods, including Direct Numerical Simulation (DNS), Large Eddy Simulation (LES), and Reynolds-Averaged Navier-Stokes (RANS), while delving into key concepts like the energy cascade and the law of the wall. It establishes the framework for subsequent chapters and provides an in-depth explanation of the SSV-PANS method, which serves as a fundamental component of the following discussions.

Chapter 4 delves into the details of the finite volume method used to discretize the governing equations, providing insights into its implementation. Additionally, the finite volume method employed in CAA simulations, is discussed in detail within this chapter.

Chapter 5 focuses on the validation and verification of the SSV-PANS method through benchmark comparisons with LES models and experimental measurements. The results obtained from the fully-developed flow in a plane channel and the periodic 2D hill test cases are presented and used to validate the numerical methods applied in this study.

Chapter 6 examines the aeroacoustic results derived from the implementation of the SSV-PANS method. Two specific scenarios are investigated: flow past a circular cylinder and flow over an Ahmed Body. The acoustic characteristics and noise generation mechanisms in these scenarios are analyzed and evaluated.

Finally, Chapter 7 concludes the thesis by summarizing the research outcomes and their implications. It highlights the contributions of the study in advancing CAA methods, improving noise prediction accuracy, and enhancing computational efficiency. Additionally, potential avenues for future research are discussed, emphasizing the opportunities for further advancements in noise reduction and sustainable vehicle design through the optimization of CAA techniques.

2 Methodology

In this chapter, the foundational aspects of Computational Fluid Dynamics (CFD) and its applications in simulating fluid dynamics are explored. First, the fundamental equations governing fluid mechanics, including the continuity and momentum equations, are introduced. Afterwards, the distinction between compressible and incompressible flows is marked by the Mach number. Afterwards, the fundamental equations for the computational aeroacoustics, direct noise computation and hybrid methods for efficient simulations are covered. Specifically, the Hydrodynamic/Acoustic Splitting Method is highlighted for accurate predictions of noise in turbulent flows. This chapter facilitates the acquisition of essential knowledge in fluid mechanics and aeroacoustics, fostering a comprehensive understanding.

2.1 Fundamentals of Fluids Mechanics

CFD is an established and influential discipline dedicated to the simulation and analysis of fluid flows through the utilization of numerical techniques. In this section, the fundamental concepts and equations governing fluid mechanics will be discussed. A detailed description of the topics in this chapter are available in [46, 47].

2.1.1 Conservation Equations for Incompressible Fluids

The behavior of a fluid can be fully described by the conservation equations of mass, momentum, and energy. The mass equation, also known as the continuity equation, is a fundamental equation in fluid mechanics that governs the conservation of mass within a fluid. The mass equation can be written as:

$$\frac{\partial \rho}{\partial t} + \frac{\partial (\rho v_i)}{\partial x_i} = 0, \tag{2.1}$$

where t is time, x_i is the spatial coordinates and v_i is the component of the velocity vector of the fluid in the i direction. The continuity equation ensures that mass is conserved within a fluid. The momentum equation is another fundamental equation in fluid mechanics that governs the conservation of momentum in a fluid. It can be expressed as:

$$\frac{\partial(\rho v_i)}{\partial t} + \frac{\partial(\rho v_i v_j)}{\partial x_j} = \frac{\partial T_{ij}}{\partial x_j} + \rho f_i. \tag{2.2}$$

Here, T_{ij} is the Cauchy stress tensor, and f_i are external forces acting on the fluid. The equation states that the rate of change of the momentum of the fluid in a given volume is equal to the net rate at which momentum is flowing into or out of that volume, plus the net force acting on that volume.

For Newtonian fluids, which is the scope of current study, the relationship between the Cauchy stress tensor and the strain rate can be expressed as:

$$T_{ij} = \mu \left(\frac{\partial v_i}{\partial x_j} + \frac{\partial v_j}{\partial x_i} - \frac{2}{3} \frac{\partial v_k}{\partial x_k} \delta_{ij} \right) - p \delta_{ij}. \tag{2.3}$$

Here, p is pressure, and δ_{ij} is the Kronecker delta (where $\delta_{ij} = 1$ if $i = j$ and $\delta_{ij} = 0$ if $i \neq j$).

The conservation equations of mass Equation 2.1 and momentum Equation 2.2 are valid for both incompressible and compressible fluids. More information on the field can be found in [46].

Mach Number

The Mach number is a vital parameter in the field of fluid dynamics. It is a dimensionless parameter that characterizes the speed of an object or fluid relative to the speed of sound. The Mach number is defined as:

$$Ma = \frac{v_\infty}{c_\infty}, \tag{2.4}$$

where v_∞ denotes the velocity of the fluid or object, while c_∞ represents the local speed of sound. The Mach number is a crucial factor in identifying the flow regime and associated phenomena. When dealing with many engineering applications, the density of the fluid remains almost constant, and compressibility effects are insignificant. If the Mach number is below 0.3, the fluid flow can be approximated as incompressible.

The continuity equation and the momentum equations for incompressible fluid flows can be expressed as follows:

$$\frac{\partial v_i^{ic}}{\partial x_i} = 0, \tag{2.5}$$

$$\frac{\rho^{ic} \partial(v^{ic})}{\partial t} + \frac{\rho^{ic} \partial(v_i^{ic} v_j^{ic})}{\partial x_j} = \frac{\partial T_{ij}}{\partial x_j} + \rho^{ic} f_i, \tag{2.6}$$

where ic indicates incompressible flow quantities. The stress tensor for incompressible flows

can be simplified as:

$$T_{ij} = \mu_f \left(\frac{\partial v_i^{ic}}{\partial x_j} + \frac{\partial v_j^{ic}}{\partial x_i} \right) - p^{ic} \delta_{ij}. \tag{2.7}$$

The conservation equations for fluids, including mass and momentum, describe fluid behavior comprehensively. These equations, along with the Cauchy stress tensor and external forces, govern mass and momentum conservation. For cases involving incompressible, isothermal, Newtonian flows where viscosity is constant, the energy conservation equation is not necessary for problem-solving [46]. By understanding and applying these fundamental principles, computational fluid dynamics (CFD) fluid flows using numerical techniques could be analyzed.

2.2 Fundamentals of Computational Aeroacoustics (CAA)

Aeroacoustics involves the study of sound generation and propagation in unsteady flow environments. It is a multidisciplinary field that combines principles of fluid dynamics, acoustics, and mathematics. Various approaches have been developed to acquire acoustic quantities, including direct noise computation and hybrid methods. Details on the methods can be found in [41, 48, 49].

2.2.1 Direct Noise Computation

Direct noise computation is a method used in aeroacoustics to acquire acoustic quantities by solving directly the governing equations This method provides accurate predictions of sound fields in turbulent flow fields but requires significant computational resources. Direct noise computation is useful for understanding the physical mechanisms of sound generation and propagation in unsteady flow fields.

2.2.2 Hybrid Methods

Hybrid methods exhibit a dual-step approach for computing acoustic variables, effectively tackling the challenge of multi-scale dynamics by separating fluid dynamics and acoustic simulations. This two-phase process involves initially employing appropriate computational fluid dynamics (CFD) methods to calculate the unsteady flow patterns within the aerodynamic source area. This step enables the precise resolution of vital turbulent flow characteristics. Subsequently, the acoustic field is determined using the acoustic sources derived from the previously computed unsteady flow field [48]. Unlike the DNC method, hybrid methods exhibit enhanced computational efficiency. This category of methods, includes various hydrodynamic/acoustic splitting techniques in addition to acoustic analogies.

Hydrodynamic/Acoustic Splitting Method

The Hydrodynamic/Acoustic Splitting Method is a commonly used technique in aeroacoustics that involves splitting the governing equations into two parts [37]. The first set of equations governs the flow field, while the second set of equations governs the propagation of sound waves in the fluid. By solving these two sets of equations separately, the computation is simplified, resulting in more efficient predictions of noise generated by turbulent flows. The approach described has proven to be effective in addressing various challenges, such as aircraft noise, wind turbine noise, and automotive noise, as documented in previous studies [48, 49].

The simulation of aeroacoustic phenomena in low subsonic flows poses significant challenges due to the large difference in scale between the flow and acoustic fluctuations [37]. The acoustic wavelength is much greater than the characteristic length scales of the flow, which leads to a large difference in magnitude between the pressure and velocity fluctuations. Capturing both the incompressible flow and small acoustic fluctuations in a single simulation is difficult, and traditional computational fluid dynamics (CFD) methods based on the Navier-Stokes equations are not well-suited for simulating aeroacoustics. As a result, specialized techniques like the Hydrodynamic/Acoustic Splitting Method have been developed to simulate both the incompressible flow and small acoustic fluctuations in a coupled manner [34, 48].

In the Hydrodynamic/Acoustic Splitting Method, the flow field is split into two components: an incompressible flow field and an acoustic field. The incompressible flow field is characterized by a constant density ρ^{ic} and a velocity field v_i^{ic}. The acoustic field, on the other hand, is characterized by small density fluctuations ρ^a and pressure fluctuations p^a that propagate at the speed of sound $C_\infty \left(= \sqrt{(\partial p/\partial \rho)_S}\right)$. The formulation used in this study to separate hydrodynamics and acoustics was formulated by Kornhaas [48]. This method which is based on the one developed by Shen and Sørensen [37], and involves breaking down the fluid field properties into an incompressible fluid dynamic part and a perturbed acoustic part:

$$\rho = \rho^{ic} + \rho^a, \tag{2.8}$$

$$v_i = v_i^{ic} + v_i^a, \tag{2.9}$$

$$p = p^{ic} + p^a. \tag{2.10}$$

The acoustic field equations describe the conservation of mass and momentum in small density and velocity fluctuations, respectively, and the propagation of pressure fluctuations through an incompressible flow field, which are given by:

Continuity equation:
$$\frac{\partial \rho^a}{\partial t} + \rho^{ic}\frac{\partial v_i^a}{\partial x_i} + v_i^{ic}\frac{\partial \rho^a}{\partial x_i} = 0. \tag{2.11}$$

Momentum equation:

$$\rho^{ic}\frac{\partial v_i^a}{\partial t} + \rho^{ic}v_j^{ic}\frac{\partial v_i^a}{\partial x_j} + \frac{\partial p^a}{\partial x_i} = 0. \qquad (2.12)$$

Acoustic wave equation:

$$\frac{\partial p^a}{\partial t} + c_\infty^2\rho^{ic}\frac{\partial v_i^a}{\partial x_i} + v_i^{ic}\frac{\partial p^a}{\partial x_i} = -\frac{\partial p^{ic}}{\partial t}. \qquad (2.13)$$

These equations constitute a type of linearized Euler equations (LEE) for acoustic wave propagation through a medium. The only source term for acoustics is the time derivative of the incompressible pressure field $-\partial p^{ic}/\partial t$. More information on the method, can be found in [34, 37, 40, 48].

The human sensation of sound is perceived on a logarithmic scale relative to acoustic pressure. To quantify sound intensity, the sound pressure level (SPL) is used, measured in decibels (dB), and it can be calculated using the following equation:

$$SPL = 10\log\left(\frac{(P_{eff}^a)^2}{(P_{ref}^a)^2}\right) = 20\log\left(\frac{P_{eff}^a}{P_{ref}^a}\right). \qquad (2.14)$$

In this equation, P_{ref}^a is the reference acoustic pressure, which has a value of 2×10^{-5} Pa. The effective acoustic pressure, denoted as P_{eff}^a, is defined as follows:

$$P_{eff}^a = \sqrt{\frac{1}{T}\int_{t=0}^{T}(P^a(t))^2 dt}. \qquad (2.15)$$

Here, T represents the total time duration of the sound signal, and $P^a(t)$ is the time-varying acoustic pressure at any given moment t. The effective acoustic pressure provides a measure of the overall intensity of the sound signal over the specified time period.

3 Turbulent Flow Simulation

The main aim of this thesis is to explore the aerodynamic noise generated by turbulent flows. In order to accomplish this objective, it is crucial to possess a thorough comprehension of turbulence, which serves as a fundamental requirement for any future studies. The following section commences with an extensive overview of turbulence, followed by a discussion on the current methodologies employed for turbulence modeling.

3.1 Turbulent Flow

Turbulent flow is a highly intricate and chaotic fluid phenomenon characterized by irregular fluctuations in velocity and pressure. It commonly occurs in high-speed flows or flows with complex geometries such as pipes, jets, and boundary layers. The concept of turbulent flow was originally explained by Osborne Reynolds, and it is commonly characterized by a dimensionless parameter called the Reynolds number (Re). The Reynolds number relates the inertial forces of a fluid to its viscous forces and can be calculated using the Reynolds number equation [50]:

$$Re = \frac{\rho v_\infty L}{\mu}. \tag{3.1}$$

In this equation, ρ represents the density of the fluid, v_∞ denotes the characteristic velocity of the flow, L signifies the characteristic length of the flow, and μ stands for the dynamic viscosity of the fluid. When the Reynolds number exceeds a certain threshold, the flow transitions from a laminar state to a turbulent state, and the irregular fluctuations in the flow become more pronounced.

Turbulence is characterized by its complex and chaotic nature, where the fluid particles move in a random and disordered manner, influenced by interactions between eddies and vortices of various sizes.

Understanding and predicting the behavior of turbulent flow is crucial in numerous engineering applications, including aerodynamics, fluid transport, and heat transfer. The subsequent content will introduce the fundamental principles of turbulence theory. For a more comprehensive understanding of this topic, readers are encouraged to consult Pope's work, which provides an in-depth overview of turbulent flow theory [51]. Additionally, references [52, 53]

offer more comprehensive theories on turbulence.

3.1.1 Energy Cascade

Once the Reynolds number surpasses a particular limit, the viscous forces in the vicinity can no longer effectively suppress arbitrary velocity fluctuations. As a result, the fluctuations in the fluid flow start to intensify, causing a previously smooth laminar flow to turn turbulent. In a turbulent flow, there are eddies of various sizes. The bigger eddies are where the majority of the kinetic energy is found, whereas the smaller ones are accountable for the dissipation of energy [51].

The energy cascade is a fundamental concept in the study of turbulent flows, and it refers to the process by which kinetic energy is transferred from large-scale eddies to smaller-scale ones, until it is eventually dissipated into heat by the viscous dissipation. The energy cascade can be visualized as a series of eddies of decreasing size, each one containing a smaller fraction of the total kinetic energy of the flow, but having a higher level of velocity fluctuations.

The transfer of energy from larger to smaller eddies occurs through via a phenomenon called vortex stretching, where the velocity gradients within an eddy cause it to deform and stretch, leading to the generation of smaller eddies. This process continues until the energy is transferred to eddies that are small enough to be affected by the action of viscosity, which dissipates the kinetic energy into heat. In Figure 3.1, the function of the energy spectrum is depicted as a function of the wave number of the eddies, illustrating the effect.
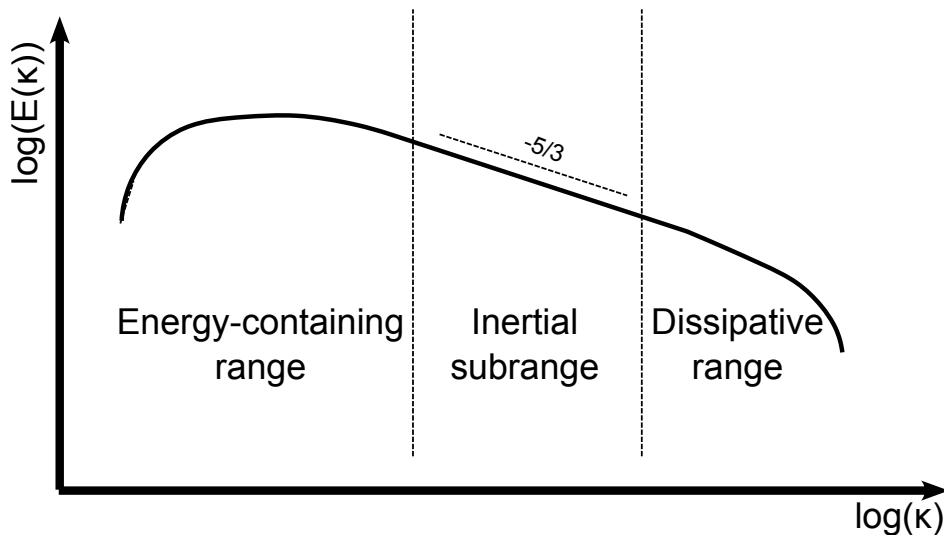
Figure 3.1 Depiction of energy cascade in the turbulence energy spectrum [54].

The Kolmogorov length scale η is the smallest length scale in a turbulent flow where viscosity dominates, representing the size of the smallest eddies given by the formula [55]:

$$\eta = \left(\frac{\nu^3}{\epsilon}\right)^{1/4}, \tag{3.2}$$

where ν represent the kinematic viscosity and, ϵ represent the rate of energy dissipation per unit mass. The Kolmogorov time scale is defined as:

$$\tau_\eta = \left(\frac{\nu}{\varepsilon}\right)^{1/2}, \tag{3.3}$$

and the Kolmogorov velocity scale is defined as:

$$u_\eta = (\nu\varepsilon)^{1/4}. \tag{3.4}$$

These scales play an important role in the statistical description of turbulence and the formulation of turbulence models.

The Kolmogorov scales are related to the Reynolds number. Specifically, the Kolmogorov length scale is related to the size of the largest eddies in the flow, characterized by a length scale l_0, by the scaling law:

$$\eta/l_0 \sim Re^{-3/4}. \tag{3.5}$$

Similarly, the Kolmogorov velocity scale is related to the characteristic velocity of the flow, denoted by u_0, by the scaling law:

$$u_\eta/u_0 \sim Re^{-1/4}, \tag{3.6}$$

and the Kolmogorov time scale is related to the characteristic time scale of the flow, denoted by τ_0, by the scaling law:

$$\tau_\eta/\tau_0 \sim Re^{-1/2}. \tag{3.7}$$

The mathematical expression relating the energy spectrum to the wave number in the inertial subrange of a turbulent flow is expressed as:

$$\kappa^{-5/3} \sim E(\kappa), \tag{3.8}$$

where $E(\kappa)$ is the kinetic energy at the wave number κ, and it is commonly referred to as Kolmogorov's 5/3 law.

3.1.2 Law of the Wall

In engineering applications involving solid structures, turbulent flows are common. Analyzing the flow near the wall is crucial for understanding turbulence, as the energy cascade theory does not account for the interaction with solid surfaces. The Law of the Wall predicts the logarithmic relationship between dimensionless velocity and distance from a solid wall in the turbulent boundary layer, and is essential for understanding turbulence near solid surfaces. Non-dimensionalization is the basis for the Law of the Wall, where physical variables are made dimensionless using scaling parameters.

The non-dimensional parameters can be expressed as follows [56]:

$$y^+ = \frac{y u_\tau}{\nu}, \tag{3.9}$$

$$u^+ = \frac{u}{u_\tau}, \tag{3.10}$$

where u represents the velocity in the tangential direction, while y corresponds to the direction normal to the wall. The friction velocity, represented as u_τ, can be calculated as $\sqrt{\tau_w/\rho}$, where the subscript w denotes the value at the wall. The wall shear stress τ_w is defined as:

$$\tau_w = \mu \left(\frac{\partial u}{\partial y} \right)_w. \tag{3.11}$$

The Law of the Wall anticipates a logarithmic correlation between the dimensionless velocity and the dimensionless distance from the wall in the logarithmic region of the turbulent boundary layer. The average velocity profile of the turbulent boundary layer can be characterized by two equations based on the dimensionless distance from the wall, y^+.

The initial equation specifies the velocity profile in the viscous sublayer, which is positioned close to the wall ($0 < y^+ < 5$):

$$u^+ = y^+. \tag{3.12}$$

The logarithmic sublayer, which is located at a greater distance from the wall ($y^+ > 30$), conforms to the logarithmic Law of the Wall for the average velocity, which is defined by the equation:

$$u^+ = \frac{1}{\kappa} \ln(y^+) + B. \tag{3.13}$$

The values of the constants κ and B depend on the flow conditions, with κ being the von Kármán constant that describes the shape of the velocity profile near the wall and is usually around 0.41.

The buffer sublayer, located between the viscous and logarithmic sublayers ($5 < y^+ < 30$), shows a transition between the linear relationship and the logarithmic Law. The Law of the

Wall is demonstrated in Figure 3.2 using direct numerical simulation data from a channel flow at $Re = 395$ [54].

The figure displays the average velocity profile in the boundary layer and exhibits the viscous sublayer, buffer sublayer, and logarithmic sublayer.
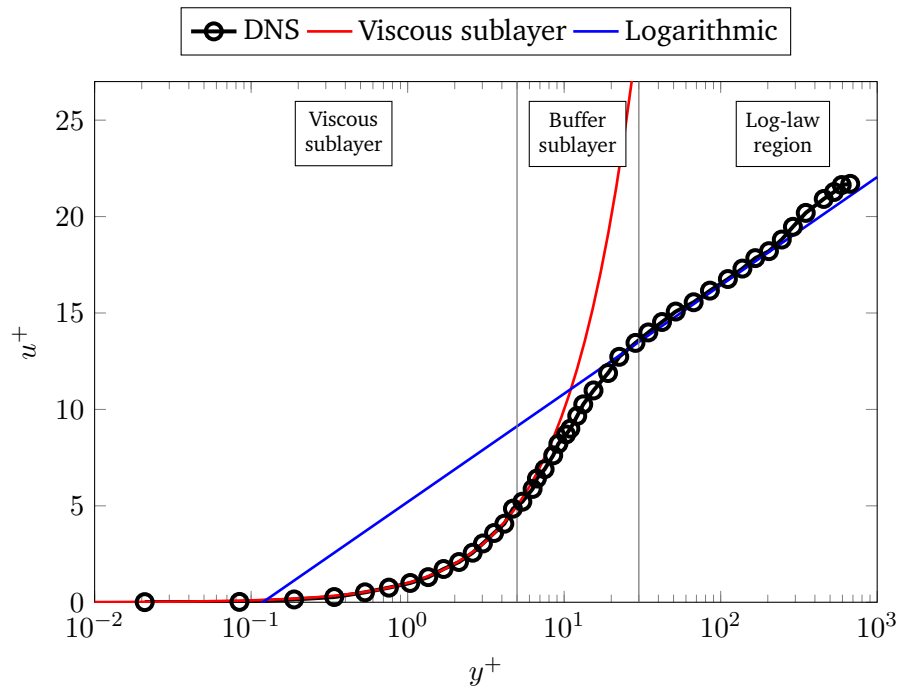
Figure 3.2 The law of the wall with data from direct numerical simulations of a channel flow with Reynolds number $Re = 395$ [54].

3.2 Direct Numerical Simulation (DNS)

Direct Numerical Simulation (DNS) is a powerful computational technique used to model fluid dynamics problems at an extremely fine scale. DNS resolves all physical parameters, including the smallest turbulent eddies, without any assumptions. To achieve this level of accuracy, DNS solves the Navier-Stokes equations directly for all scales, from the largest to the smallest, using a high-resolution numerical grid and time step [2, 3]. Therefor it is necessary to use high-performance computing methods, which require substantial computational resources.

DNS necessitates a fine grid resolution to ensure accurate results, which can be computationally expensive and limited to low Reynolds number flows. Moreover, the computational cost of DNS scales with the cube of the Reynolds number, making it presently unsuitable for many engineering applications .

Despite its high cost, DNS is an invaluable tool for comprehending the fundamental physics

of turbulence, and for developing and validating turbulence models for other computational methods.

3.3 Large Eddy Simulation (LES)

The Large eddy simulation (LES) method involves decomposing the flow into resolved and unresolved scales, where the resolved scales are computed directly and the unresolved scales are modeled using turbulence models. The idea of LES method is illustrated in Figure 3.3. The LES method is based on solving the filtered Navier-Stokes equations, which are obtained by filtering the governing equations over a length scale larger than the characteristic length of the turbulence. According to Wagner et al. [41], the large eddies drive the dominant portion of turbulent kinetic energy and flow dynamics, making this method advantageous.
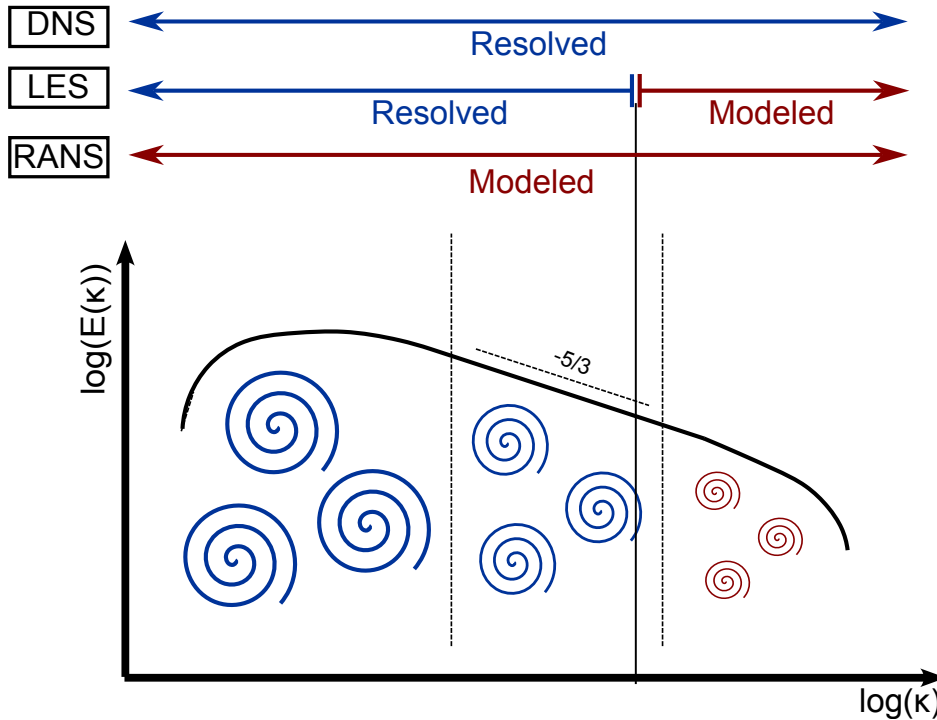
Figure 3.3 Treatment of turbulent structures: Comparing DNS, LES, and RANS through turbulent energy cascade.

The filtered variable is defined as:

$$\phi(\boldsymbol{x}, t) = \bar{\phi}(\boldsymbol{x}, t) + \phi'(\boldsymbol{x}, t), \tag{3.14}$$

where $\bar{\phi}(\boldsymbol{x}, t)$ is the filtered variable, $\phi'(\boldsymbol{x}, t)$ is the residual or subgrid-scale (SGS) variable, and $\phi(\boldsymbol{x}, t)$ is the original variable. The filtered variable can be computed using a convolution

operation:

$$\bar{\phi}(\boldsymbol{x}, t) = \int G(\boldsymbol{x}, \boldsymbol{y}) \phi(\boldsymbol{x} - \boldsymbol{y}, t) d\boldsymbol{y} = G * \phi, \tag{3.15}$$

where $G(\boldsymbol{x}, \boldsymbol{y})$ is the filter kernel. Applying a filtering process to the Navier-Stokes equations results in the filtered continuity and momentum equations:

$$\frac{\partial \overline{v_i^{ic}}}{\partial x_i} = 0, \tag{3.16}$$

$$\frac{\partial (\rho^{ic} \overline{v_i^{ic}})}{\partial t} + \frac{\partial (\rho^{ic} \overline{v_i^{ic} v_j^{ic}})}{\partial x_j} = \frac{\partial}{\partial x_j} \left[\mu^f \left(\frac{\partial \overline{v_i^{ic}}}{\partial x_j} + \frac{\partial \overline{v_j^{ic}}}{\partial x_i} \right) \right] - \frac{\partial \tau_{ij}^{sgs}}{\partial x_j} - \frac{\partial p^{ic}}{\partial x_i}. \tag{3.17}$$

In LES, the filtered Navier-Stokes equations are solved numerically using appropriate discretization schemes. To close the equations, a turbulence model is required to model the SGS stresses. The SGS stress tensor τ_{ij}^{sgs} is defined as:

$$\tau_{ij}^{sgs} = \rho^{ic} \left(\overline{v_i^{ic} v_j^{ic}} - \bar{v}_i^{ic} \bar{v}_j^{ic} \right), \tag{3.18}$$

where ρ^{ic} and $\bar{v}_i^{ic}$ are the filtered density and velocity, respectively.

The SGS stress tensor can be decomposed into an isotropic part and a deviatoric part:

$$\tau_{ij}^{sgs} = \tau_{ij}^d + \frac{1}{3} \tau_{kk}^{sgs} \delta_{ij}, \tag{3.19}$$

where τ_{ij}^d is the deviatoric part, τ_{kk}^{sgs} is the trace of the SGS stress tensor, and δ_{ij} is the Kronecker delta. The deviatoric part of the SGS stress tensor can be modeled using the eddy viscosity concept. For incompressible flow problems τ_{ij}^{sgs}, can be expressed in terms of the strain rate tensor of the resolved velocity field $\bar{S}_{ij}$:

$$\tau_{ij}^{sgs} - \frac{1}{3} \tau_{kk}^{sgs} \delta_{ij} = -2\mu_t \overline{S}_{ij}, \tag{3.20}$$

where $\bar{S}_{ij}$ is defined as:

$$\overline{S}_{ij} = \frac{1}{2} \left(\frac{\partial \bar{v}_i^{ic}}{\partial x_j} + \frac{\partial \bar{v}_j^{ic}}{\partial x_i} \right). \tag{3.21}$$

The eddy viscosity μ_t, is modeled using the Smagorinsky model:

$$\mu_t = C_s^2 \rho^{ic} \Delta^2 \left| \overline{S}_{ij} \right|, \tag{3.22}$$

where C_s is the Smagorinsky constant, Δ is the filter width, and $\left| \bar{S}_{ij} \right|$ is the magnitude of the strain rate tensor. The filter width is defined as:

$$\Delta = (\Delta_x \Delta_y \Delta_z)^{\frac{1}{3}}, \tag{3.23}$$

where Δ_x, Δ_y, and Δ_z are the filter widths in the corresponding spatial direction.

The Smagorinsky model supposes that the eddy viscosity is proportional to the square of the filter width, the magnitude of the strain rate tensor, and the density. The value of the Smagorinsky constant C_s is usually set to 0.1, although it may vary depending on the specific application [57, 58].

Meyers and Sagaut provided a theoretical evaluation of the Smagorinsky constant [59]. However, Germano developed a novel approach for calculating the Smagorinsky constant based on LES outcomes [6]. This method introduces a time- and space-dependent function for C_s, denoted as $C_s(\boldsymbol{x}, t)$, which is considered more accurate than a constant value. To evaluate C_s dynamically, a test filter with a width $\hat{\Delta}$ greater than the grid filter width Δ is defined, where $\hat{\Delta} = 2\Delta$ is commonly used.

By implementing the test filter on the filtered momentum equation, the subgrid-scale stresses τ_{ij}^{test} can be expressed as follows:

$$\tau_{ij}^{\text{test}} = \left(\widehat{\overline{v_i^{ic} v_j^{ic}}} - \overline{v}_i^{ic} \overline{v}_j^{ic} \right). \tag{3.24}$$

The Smagorinsky model is utilized to approximate the subgrid-scale and subtest-scale stresses [46]:

$$\tau_{ij}^{\text{sgs}} - \frac{1}{3} \delta_{ij} \tau_{kk}^{\text{sgs}} = -2C_g \Delta^2 |\overline{S}| \overline{S} ij =: -2C_g \alpha_{ij}^{\text{sgs}}, \tag{3.25}$$

$$\tau_{ij}^{\text{test}} - \frac{1}{3} \delta_{ij} \tau_{kk}^{\text{test}} = -2C_g \hat{\Delta}^2 |\hat{\overline{S}}| \hat{\overline{S}}_{ij} =: -2C_g \alpha_{ij}^{\text{sgs}}, \tag{3.26}$$

where the model parameter, C_g, is defined as the square of C_s. The resolved turbulent stresses can be defined by:

$$L_{ij} = \left(\widehat{\overline{v}_i^{ic} \overline{v}_j^{ic}} - \hat{\overline{v}}_i^{ic} \hat{\overline{v}}_j^{ic} \right). \tag{3.27}$$

These scales represent the length between the grid-filter length and the test-filter length.

By inserting the approximations (3.25) and (3.24) into the Germano identity, the following result is obtained as per [3]:

$$L_{ij} = \tau_{ij}^{\text{test}} - \widehat{\tau_{ij}^{\text{sgs}}}. \tag{3.28}$$

Substituting these approximations into the equation yields:

$$L_{ij} = -2C_g \alpha_{ij}^{\text{test}} + 2\widehat{C_g \alpha_{ij}^{\text{sgs}}}. \tag{3.29}$$

Employing the approximation

$$\widehat{C_g \alpha_{ij}^{\text{sgs}}} \approx C_g \widehat{\alpha_{ij}^{\text{sgs}}}, \tag{3.30}$$

where C_g is assumed to be constant over the test filter width. Simplifing the expression further gives:

$$L_{ij} = 2C_g \left(\widehat{\alpha_{ij}^{\text{sgs}}} - \alpha_{ij}^{\text{test}} =: 2C_g M_{ij} \right).$$
(3.31)

In order to solve for the unknown parameter C_g, which has one unknown and five independent equations, Lilly (1992) proposed using the least-squares method to minimize the square of the error [60]. The equation to minimize the square of the error is given by:

$$E = L_{ij} - 2C_g M_{ij}.$$
(3.32)

In the context where both sides of the equation are symmetric with zero traces, the derivative of E^2 with respect to C_g is taken and set equal to zero, resulting in:

$$\frac{\partial E^2}{\partial C_g} = 4(L_{ij} - 2C_g M_{ij})M_{ij} = 0,$$
(3.33)

which gives us the value of the unknown parameter C_g as:

$$C_g(x,t) = \frac{L_{ij}M_{ij}}{2M_{ij}M_{ij}}.$$
(3.34)

The eddy viscosity can be evaluated using the following equation:

$$\mu_t = \rho^{ic} C_g \Delta^2 |\overline{S}_{ij}|.$$
(3.35)

To prevent numerical instabilities caused by negative values of C_g, several proposals have been made. One approach involves applying time and spatial averaging or simply clipping negative values as follows:

$$C_g(x,t) = \max \left(\frac{L_{ij}M_{ij}}{2M_{ij}M_{ij}}, 0 \right).$$
(3.36)

It should be noted that the dynamic procedure can be applied to other models besides the Smagorinsky model.

3.4 Reynolds-Averaged Navier-Stokes (RANS)

Reynolds-Averaged Navier-Stokes (RANS) modeling is a widely used approach to model turbulent fluid flows. The basic idea behind RANS is to separate the fluid motion into two components: a time-averaged component and a fluctuating component [7]. The time-averaged component is assumed to be smooth and predictable, while the fluctuating component is assumed to be random and chaotic.

The RANS equations are derived by applying the Reynolds decomposition, which separates a quantity $\phi(\boldsymbol{x}, t)$ into its time-averaged component $\overline{\phi}(\boldsymbol{x})$ and its fluctuating component $\phi'(\boldsymbol{x}, t)$:

$$\phi(\boldsymbol{x}, t) = \overline{\phi}(\boldsymbol{x}) + \phi'(\boldsymbol{x}, t). \tag{3.37}$$

The time-averaged component is defined as:

$$\overline{\phi}(\boldsymbol{x}) = \lim_{T \to \infty} \frac{1}{T} \int_{t_0}^{t_0 + T} \phi(\boldsymbol{x}, t), dt. \tag{3.38}$$

The RANS equations are then obtained by time-averaging the Navier-Stokes equations. The continuity equation, which expresses the conservation of mass, is unchanged by the time averaging process. However, the momentum equation is modified to account for the time-averaged and fluctuating components of velocity, pressure, and viscosity. The continuity equation is:

$$\frac{\partial \overline{v_i^{ic}}}{\partial x_i} = 0, \tag{3.39}$$

where $\overline{v_i^{ic}}$ is the time-averaged velocity component in the i direction.

The momentum equation is:

$$\frac{\partial (\rho \overline{v_i^{ic}})}{\partial t} + \frac{\partial}{\partial x_j} \left[\rho \overline{v_i^{ic}} \, \overline{v_j^{ic}} + \rho \overline{v_i^{ic'} v_j^{ic'}} - \mu \left(\frac{\partial \overline{v_i^{ic}}}{\partial x_j} + \frac{\partial \overline{v_j^{ic}}}{\partial x_i} \right) \right] + \frac{\partial \overline{p}}{\partial x_i} = \rho f_i. \tag{3.40}$$

where $\overline{p}$ is the time-averaged pressure.

The Reynolds stress tensor is needed to solve the RANS equations but is underdetermined. Two common methods to obtain it are the Reynolds stress equation model (RSM) and eddy viscosity models using the Boussinesq approximation [61].

The Reynolds stresses, which are the products of the fluctuating velocity components, are modeled using the Boussinesq approximation. The Boussinesq approximation assumes that the Reynolds stresses are proportional to the local strain rate and can be modeled using an eddy viscosity μ_t. The Reynolds stresses can be expressed as:

$$\rho \overline{v_i^{ic'} v_j^{ic'}} = -\mu_t \left(\frac{\partial \overline{v_i^{ic}}}{\partial x_j} + \frac{\partial \overline{v_j^{ic}}}{\partial x_i} \right) + \frac{2}{3} \rho \delta_{ij} k, \tag{3.41}$$

where k is the turbulent kinetic energy. The eddy viscosity μ_t is modeled using various turbulence closure models, such as the popular $k - \epsilon$ and $k - \omega$ models.

The turbulent kinetic energy k is defined as the time-averaged kinetic energy associated with

the fluctuating velocity components:

$$k = \frac{1}{2}\overline{v_i^{ic\prime} v_j^{ic\prime}}.$$ (3.42)

The strain rate tensor S_{ij} is defined as the symmetric part of the velocity gradient tensor and represents the rate of deformation of the fluid:

$$S_{ij} = \frac{1}{2}\left(\frac{\partial \overline{v_i^{ic}}}{\partial x_j} + \frac{\partial \overline{v_j^{ic}}}{\partial x_i}\right).$$ (3.43)

In the RANS equations to achieve accurate results, the choice of turbulence model and numerical discretization scheme are crucial. While RANS simulations are less computationally expensive compared to more accurate but computationally expensive large eddy simulations (LES) and direct numerical simulations (DNS), the accuracy of RANS simulations depends heavily on the chosen turbulence model. The widely used eddy viscosity models are popular due to their lower computational cost and acceptable accuracy, but they may produce inaccurate results in anisotropic turbulent flows.

Several turbulence models have been developed to determine the dynamic turbulent viscosity, including the Spalart-Allmaras model [62], the $k - \epsilon$ model [63, 64], the $k - \omega$ model, and the SST $k - \omega$ model [65, 66]. While the k-epsilon model provides satisfactory results, the SST $k - \omega$ model combines the $k - \epsilon$ model and the $k - \omega$ model for improved accuracy. A more advanced four-equation model is the $k - \epsilon - \zeta - f$ RANS model, which includes transport equations for k, ϵ, the velocity scale ratio (ζ), and the elliptic relaxation function (f) [67, 68].

3.5 Hybrid RANS/LES Methods

Hybrid RANS/LES (Reynolds-Averaged Navier-Stokes/Large Eddy Simulation) methods are a type of computational fluid dynamics (CFD) technique that combines the advantages of RANS and LES models [69, 70]. These methods aim to capture the unsteady features of turbulent flows that are not well resolved by RANS models while still being computationally efficient.

In most of the hybrid RANS/LES methods, the flow is divided into two regions based on a filtering process. The first region, known as the RANS region, is usually where the grid filter size is larger than the characteristic size of the turbulence structures, and the RANS equations are used to model the turbulence. The second region, called the LES region, is where the grid filter size is smaller than the characteristic size of the turbulence structures, and the LES equations are used to resolve the turbulence.

The transition between the RANS and LES regions is governed by a blending function that smoothly varies between the RANS and LES models. This blending function can be based on the distance from the wall or the local turbulence intensity, among other parameters.

The hybrid RANS/LES methods have several advantages over traditional RANS or LES models. Firstly, they are more accurate than RANS models in capturing the unsteady behavior of turbulent flows. By resolving a portion of the small-scale turbulence, hybrid methods can provide improved predictions of flow features such as vortex shedding, flow separation, and turbulent mixing. Secondly, these methods are computationally less expensive than LES models since the RANS model is employed in regions where the turbulence is not as well resolved. This computational efficiency makes hybrid RANS/LES methods more accessible for practical engineering applications.

Some popular hybrid LES/RANS models include detached-eddy simulation (DES) [8, 71], very large eddy simulation (VLES) [10], limited numerical scales (LNS) model [11, 12], scale-adaptive simulation (SAS) model [72], delayed detached eddy simulation (DDES) [73] and the partially averaged Navier-Stokes equation (PANS) model [13, 14]. A detailed review about hybrid LES/RANS method is given by Fröhlich [74]. In the following, the Partially Averaged Navier-Stokes method (PANS), is explained.

3.6 Partially Averaged Navier-Stokes method (PANS)

The Partially-Averaged Navier-Stokes model (PANS) is a hybrid approach that seamlessly transitions between Reynolds-Averaged Navier-Stokes (RANS) modeling and the Direct Numerical Solution (DNS) approach for solving the Navier-Stokes equations. This approach aims to improve the accuracy of results within the limitations of available computational resources. In the RANS method, the flow is time-averaged, and statistical quantities, such as the mean flow and turbulent stresses, are solved for. Unsteady fluctuations are modeled using turbulence closure models. On the other hand, LES accurately resolves large-scale motions or energy-carrying eddies while approximating smaller-scale motions.

To illustrate the working domains of PANS, a typical energy spectrum for turbulent flow is employed, depicting the cut-off point for unresolved flow scales in RANS, PANS, and LES, as shown in Figure 3.4.

PANS establishes a relationship between the resolved and unresolved components by employing a cut-off resolution parameter that governs the transition from RANS to LES.

PANS is based on the premise that the physical phenomena necessary for accurate predictive calculations exist within flow scales that are not fully resolved in RANS but are significantly larger than the smallest LES scales. Consequently, PANS aims to resolve only those scales that significantly contribute to the desired objective function while bypassing computationally intensive small scales. Instead of attempting to merge distinct RANS and LES models in separate regions, PANS provides a closure model that can be applied at any intermediate scale resolution level.

The PANS method, as described by Girimaji [14], distinguishes itself from LES through
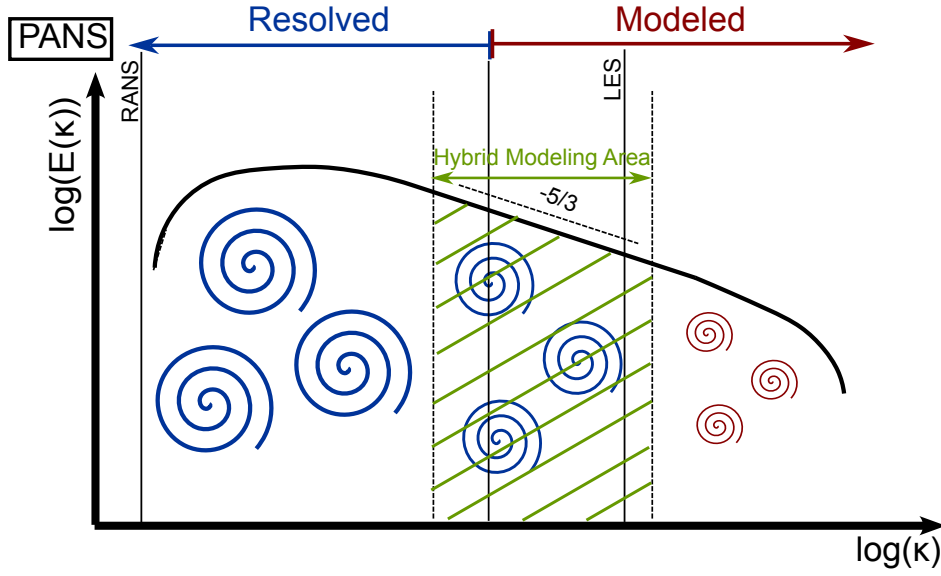
Figure 3.4 Schematic representation of PANS energy cascade.

three main characteristics. Firstly, unlike relying on a cutoff wave number, the velocity field decomposition in PANS is determined based on the kinetic energy content. Secondly, PANS incorporates a filtering operation that separates the resolved motion from the unresolved motion, eliminating the need for an additional filtering step during computation. Lastly, the constitutive relationship for the subfilter scale (SFS) in PANS remains independent of grid spacing, allowing the physical resolution or filter width to be decoupled from the numerical resolution. However, it is essential to ensure that the numerical resolution aligns with the desired filter width to achieve accurate results. These aspects offer greater flexibility in capturing the desired level of detail in the simulation while maintaining computational efficiency.

The PANS method separates the instantaneous velocity V_i into partially filtered and sub-filter components, as shown below:

$$V_i = v_i^{ic} + u_i^{ic}. \tag{3.44}$$

The PANS equations, expressed in terms of filtered velocity and pressure fields, are given by [75]:

$$\frac{\partial v_i^{ic}}{\partial t} + v_j^{ic}\frac{\partial v_i^{ic}}{\partial x_j} + \frac{\partial \tau(V_i, V_j)}{\partial x_j} = -\frac{1}{\rho}\frac{\partial p}{\partial x_i} + \nu \frac{\partial^2 v_i^{ic}}{\partial x_j \partial x_j}, \tag{3.45}$$

where p is the filtered pressure field. Using the Boussinesq approximation, the sub-filter stress is obtained as:

$$\tau(V_i, V_j) = -2\nu_u S_{ij} + 2/3k_u\delta_{ij}, \tag{3.46}$$

where k_u is the unresolved kinetic energy. The unresolved eddy viscosity ν_u is given by:

$$\nu_u = c_\mu \frac{k_u^2}{\epsilon_u}, \tag{3.47}$$

where ϵ_u is the unresolved dissipation, and the resolved stress tensor S_{ij} is defined as:

$$S_{ij} = \frac{1}{2} \left(\frac{\partial v_i^{ic}}{\partial x_j} + \frac{\partial v_j^{ic}}{\partial x_i} \right), \tag{3.48}$$

Girimaji [14], presents model equations for the unresolved kinetic energy. The equations include terms for convection of unresolved energy by resolved fluctuations and are modeled using the zero-transport model. The resolved fluctuations are defined by:

$$u_j = v_j^{ic} - \overline{v_j^{ic}}. \tag{3.49}$$

The final equations that determine the values of k_u and ϵ_u are as follows:

$$\frac{\partial k_u}{\partial t} + v_j^{ic} \frac{\partial k_u}{\partial x_j} = P_u - \epsilon_u + \frac{\partial}{\partial x_j} \left(\frac{\nu_u}{\sigma_{ku}} \frac{\partial k_u}{\partial x_j} \right), \tag{3.50}$$

$$\frac{\partial \epsilon_u}{\partial t} + v_j^{ic} \frac{\partial \epsilon_u}{\partial x_j} = C_{\epsilon 1} P_u \frac{\epsilon_u}{k_u} - C_{\epsilon 2}^* \frac{\epsilon_u^2}{k_u} + \frac{\partial}{\partial x_j} \left(\frac{\nu_u}{\sigma_{\epsilon u}} \frac{\partial \epsilon_u}{\partial x_j} \right), \tag{3.51}$$

with the model coefficients as following:

$$C_{\epsilon 2}^* = C_{\epsilon 1} + \frac{f_k}{f_\epsilon} (C_{\epsilon 2} - C_{\epsilon 1}), \tag{3.52}$$

$$\sigma_{k_u} = \sigma_k \frac{f_k^2}{f_\epsilon}, \qquad \sigma_{\epsilon_u} = \sigma_\epsilon \frac{f_k^2}{f_\epsilon}. \tag{3.53}$$

The resolution parameter for the unresolved-to-total ratios of kinetic energy is:

$$f_k = \frac{k_u}{k}, \tag{3.54}$$

and for the unresolved-to-total ratios of dissipation is:

$$f_\epsilon = \frac{\epsilon_u}{\epsilon}. \tag{3.55}$$

The resolution parameters take values between zero and one, representing the two extremes of DNS and RANS, as well as all intermediate resolutions. Girimaji and Abdul-Hamid [13] suggested calculating f_k using Equation (3.56) which must have larger values than Equation (3.54):

$$f_k \geq \frac{1}{\sqrt{C_\mu}} \left(\frac{\Delta}{\Lambda} \right)^{2/3}, \tag{3.56}$$

where $\Delta \left(= (\Delta_x \Delta_y \Delta_z)^{1/3}\right)$ is the grid cells dimension and $\Lambda \left(= k^{3/2}/\epsilon\right)$ is the integral length scale of turbulence. The parameter f_ϵ is assumed as 1, which is valid when the flow has a high Reynolds number [26].

As discussed before, accurately describing near-wall turbulence behavior is challenging at high Reynolds numbers, as the parameter f_k is high near the wall. Most PANS models are derived from two-equation RANS models, which do not capture advanced aspects of boundary layers. To improve this, Basara et al. [25] proposed a four-equation PANS model based on the RANS $k - \epsilon - \zeta - f$ model, which exhibits excellent near-wall characteristics. This variant of the $\nu^2 - f$ model includes a transport equation for the wall-normal velocity scale ratio ζ_u $\left(= \overline{\nu_u^2}/k_u\right)$ instead of velocity scale ,ν^2, and solves an elliptic relaxation equation for f. Thus:

$$\nu_u = c_\mu \zeta_u \frac{k_u^2}{\epsilon_u}. \tag{3.57}$$

The transport equation for the wall-normal velocity scale ratio is [25]:

$$\frac{\partial \zeta_u}{\partial t} + v_j^{ic} \frac{\partial \zeta_u}{\partial x_j} = f_u - \frac{\zeta_u}{k_u} P_u + \frac{\zeta_u}{k_u} \epsilon_u (1 - f_k) + \frac{\partial}{\partial x_j} \left[\left(\frac{\nu_u}{\sigma_{\zeta u}} \right) \frac{\partial \zeta_u}{\partial x_j} \right], \tag{3.58}$$

where the resolution parameter f_ζ is equal to:

$$f_\zeta = \frac{\zeta_u}{\zeta}, \tag{3.59}$$

which is integrated into the elliptic relaxation equation:

$$L_u^2 \nabla^2 f_u - f_u = \frac{1}{T_u} \left(c_1 + c_2 \frac{P_u}{\epsilon_u} \right) (\zeta_u - \frac{2}{3}), \tag{3.60}$$

where $C_\mu = 0.22$, $c_1 = 0.4$, $c_2 = 0.65$, and $C_{\epsilon 2} = 1.9$.

The length scale L_u and the time scale T_u are as following:

$$T_u = \max \left[\frac{k_u}{\epsilon}, C_\tau \left(\frac{\nu}{\epsilon} \right)^{1/2} \right], \tag{3.61}$$

$$L_u = C_L \max \left[\frac{k_u^{3/2}}{\epsilon}, C_\eta \left(\frac{\nu^3}{\epsilon} \right)^{1/4} \right]. \tag{3.62}$$

This method makes the turbulence intensity near the wall more sensitive to the wall effect and is well-suited for enhancing near-wall PANS performance.

Scale supplying variable (SSV) equation

In previous studies involving the two- and four-equation PANS models, the determination of the integral scale of turbulence relied on calculating the differences between the instantaneous filtered velocity and the averaged velocity field, as outlined in Equation 3.49. However, this approach becomes impractical in scenarios characterized by moving geometries or transient boundaries.

To overcome this challenge, Basara and Girimaji [76] proposed an alternative method of solving an additional equation for the integral scale as a supplementary variable. Their preliminary investigations demonstrated the feasibility of this approach in channel flow simulations [76] and square cylinder simulations [26]. By introducing this supplementary equation for the resolved kinetic energy, referred to as instantaneous modelled resolved turbulent kinetic energy (k_{ssv}), the accuracy and applicability of PANS models in turbulent flow simulations is enhanced, particularly in scenarios involving complex geometries and dynamic boundary conditions. This incorporation of the k_{ssv} equation holds promising prospects for advancing our understanding and modeling capabilities in turbulence simulations.

A summary of the derivation of the method is presented in the following.

To start, the total kinetic energy, k, is expressed as:

$$k = k_{ssv} + k_u. \tag{3.63}$$

The evolution of k is governed by the Reynolds-Averaged Navier-Stokes (RANS) equation, which can be expressed as:

$$\frac{Dk}{Dt} = \frac{\partial k}{\partial t} + \overline{v_j^{ic}} \frac{\partial k}{\partial x_j} = P - \epsilon + \frac{\partial}{\partial x_j} \left[\left(\nu + \frac{\nu_t}{\sigma_k} \right) \frac{\partial k}{\partial x_j} \right]. \tag{3.64}$$

To derive the k_{ssv} equation, the average velocity in the RANS equation is replaced with Equation 3.49 , and then inserting Equation 3.63 leads to:

$$\frac{\partial(k_{ssv} + k_u)}{\partial t} + v_j^{ic} \frac{\partial(k_{ssv} + k_u)}{\partial x_j} - u_j^{ic} \frac{\partial(k_{ssv} + k_u)}{\partial x_j} =$$
$$P - \epsilon + \frac{\partial}{\partial x_j} \left[\left(\nu + \frac{\nu_t}{\sigma_k} \right) \frac{\partial(k_{ssv} + k_u)}{\partial x_j} \right]. \tag{3.65}$$

After further simplifications and using the zero-transport model, Equation (3.65) can be expressed as:

$$\frac{\partial k_{ssv}}{\partial t} + v_j^{ic} \frac{\partial k_{ssv}}{\partial x_j} = -(P_u - \epsilon_u) + u_j \frac{\partial k_{ssv}}{\partial x_j} +$$
$$P - \epsilon + \frac{\partial}{\partial x_j} \left[\left(\nu + \frac{\nu_t}{\sigma_k} \right) \frac{\partial k_{ssv}}{\partial x_j} \right], \tag{3.66}$$

using the following expression:

$$P_u - \epsilon_u = f_k(P - \epsilon). \tag{3.67}$$

The final form of the k_{ssv} equation can be expressed as:

$$\frac{\partial k_{ssv}}{\partial t} + v_j^{ic} \frac{\partial k_{ssv}}{\partial x_j} = (1 - f_k)(P - \epsilon) + \frac{\partial}{\partial x_j}\left[\left(\nu + \frac{\nu}{\sigma_{ku}}\right)\frac{\partial k_{ssv}}{\partial x_j}\right]. \tag{3.68}$$

In order to make f_k responsive to the local grid, it is computed using the following relation:

$$f_k = \frac{1}{\sqrt{C_\mu}}\left(\frac{\Delta}{\Lambda}\right)^{2/3}. \tag{3.69}$$

However, in this case, the integral length scale of turbulence, Λ, is modified to incorporate the total kinetic energy as $k = k_u + k_{ssv}$. It's important to note that the values obtained for f_k through Equation (3.69) must always be larger than ku/k at the end of the time step. The complete derivation of the method as well as the preliminary results for a turbulent channel flow is presented in [76] and the results for the turbulent flow around a square cylinder is presented in the work of Basara et al. [26].

The final set of equations of the SSV-PANS method based on the $k - \epsilon - \zeta - f$ are:

$$\frac{\partial k_u}{\partial t} + v_j^{ic} \frac{\partial k_u}{\partial x_j} = P_u - \epsilon_u + \frac{\partial}{\partial x_j}\left[\left(\nu + \frac{\nu_u}{\sigma_{ku}}\right)\frac{\partial k_u}{\partial x_j}\right], \tag{3.70}$$

$$\frac{\partial \epsilon_u}{\partial t} + v_j^{ic} \frac{\partial \epsilon_u}{\partial x_j} = C_{\epsilon 1} P_u \frac{\epsilon_u}{k_u} - C_{\epsilon 2}^* \frac{\epsilon_u^2}{k_u} + \frac{\partial}{\partial x_j}\left[\left(\nu + \frac{\nu_u}{\sigma_{\epsilon u}}\right)\frac{\partial \epsilon_u}{\partial x_j}\right], \tag{3.71}$$

$$\frac{\partial \zeta_u}{\partial t} + v_j^{ic} \frac{\partial \zeta_u}{\partial x_j} = f_u - \frac{\zeta_u}{k_u} P_u - \frac{\zeta_u}{k_u} \epsilon_u (1 - f_k) + \frac{\partial}{\partial x_j}\left[\left(\nu + \frac{\nu_u}{\sigma_{\zeta u}}\right)\frac{\partial \zeta_u}{\partial x_j}\right], \tag{3.72}$$

$$L_u^2 \nabla^2 f_u - f_u = \frac{1}{T_u}\left(c_1 + c_2 \frac{P_u}{\epsilon_u}\right)(\zeta_u - \frac{2}{3}), \tag{3.73}$$

$$\frac{\partial k_{ssv}}{\partial t} + v_j^{ic} \frac{\partial k_{ssv}}{\partial x_j} = (1 - f_k)(P - \epsilon) + \frac{\partial}{\partial x_j}\left[\left(\nu + \frac{\nu}{\sigma_{ku}}\right)\frac{\partial k_{ssv}}{\partial x_j}\right]. \tag{3.74}$$

The new variable k_{ssv} represents a modeled resolved kinetic energy, enabling simultaneous computation of both unresolved and resolved kinetic energy. This advancement facilitates the continuous updating of the resolution parameter, denoted as f_k. Consequently, the need for laborious calculations of the averaged velocity field, which was previously the standard in PANS calculations, is eliminated.

In particular, when dealing with scenarios involving moving geometries, transient boundaries, and time-dependent calculations, the SSV-PANS method provides efficient and accurate

solutions [26, 76]. Encouraging preliminary results obtained from the SSV-PANS method demonstrate the practicality and accuracy of this proposed approach, making it highly promising for current research purposes.

4 Numerical Methods

This chapter is dedicated to exploring numerical methods used for solving the governing equations related to flow and acoustic problems, which were discussed in the previous chapter. Since analytical solutions are often not feasible for the partial differential equations (PDEs) that govern flow motion and acoustic propagation, it becomes necessary to establish mathematical models and discretize the problem domain in order to make progress.

Numerous numerical approaches have been developed to obtain approximate solutions, and these methods typically involve dividing the problem domain into finite cells or elements, which results in the creation of a numerical grid. Discretization techniques such as finite-volume methods (FVM), finite-element methods (FEM), and finite-difference methods (FDM) are commonly employed to discretize the conservation equations. The choice of a specific method and algorithm depends on the particular requirements of the equation being addressed.

This chapter introduces numerical methods used in the thesis, specifically for incompressible flow equations and acoustic equations. The computational fluid dynamics methods are presented first, followed by a subsequent section dedicated to computational aeroacoustics.

4.1 Computational Fluid Dynamics

In this section, the numerical framework employed to tackle incompressible flow problems is introduced. The finite-volume method is used to obtain the numerical solution, which is computed using the computational fluid dynamics solver FASTEST [1]. For further details on the topics covered in this section, readers are referred to the following references: [46, 47, 77].

4.1.1 Finite Volume Method

The Finite Volume Method (FVM) is a popular numerical technique for solving the governing equations of fluid flow. The FVM divides the computational domain into a set of control volumes, each containing a discrete set of computational nodes. The governing equations are then integrated over each control volume to obtain a set of algebraic equations that can be solved numerically.

The formulation for the transport equation of a conserved scalar variable ϕ is given by [47]:

$$\frac{\partial(\rho^{ic}\phi)}{\partial t} + \frac{\partial(\rho^{ic}v_j^{ic}\phi)}{\partial x_j} = \frac{\partial}{\partial x_j}\left(\Gamma_\phi \frac{\partial\phi}{\partial x_j}\right) + q_\phi, \tag{4.1}$$

where ρ_i^{ic} is the density, v_j^{ic} is the velocity component in the j direction, Γ_ϕ is the diffusion coefficient, and q_ϕ is the source term.

The first term on the left-hand side represents the unsteady term, which accounts for the change in ϕ with time. The second term represents the convection term, which accounts for the transport of ϕ by the fluid motion. The third term represents the diffusion term, which accounts for the diffusive flux of ϕ due to concentration gradients. The last term represents the source term, which accounts for any external sources of ϕ.

The process of using the Finite Volume Method (FVM) to solve equations involves discretizing both space and time. First, the computational domain is divided into control volumes, and the integral form of the equation is derived using the divergence theorem. The resulting discrete equations are then advanced in time using a time-marching scheme, and the algebraic equations are solved iteratively until convergence using methods such as the pressure correction or SIMPLE algorithm. For improved legibility, the section excludes the index denoting incompressible variables (ic).

4.1.2 Spatial Discretization

The current research uses block-structured grids for spatial discretization in numerical methods for solving partial differential equations. To obtain an integral equation that accounts for the conservation of mass and momentum, including convective and diffusive fluxes and the source term, the transport equation Equation 4.1 is integrated over a control volume. This integral equation is then written for each control volume by integrating over the volume and applying the Gauss integral theorem:

$$\int_V \rho \frac{\partial(\rho\phi)}{\partial t} \mathrm{d}V + \sum_c \int_{S_c} \rho v_i \phi n_i \mathrm{d}S_c = \sum_c \int_{S_c} \Gamma\phi \frac{\partial\phi}{\partial x_i} n_i \mathrm{d}S_c + \int_V q_\phi \mathrm{d}V, \tag{4.2}$$

where the subscript c can take values from e, w, n, s, t, or b, the statement describes the convective and diffusive fluxes through the faces of a control volume (CV). In Figure 4.1, a hexahedral control volume is shown that contains the center of the cell denoted by P. The faces of the control volume are named after their directional positions with respect to the neighboring control volumes containing the center points E, W, N, S, T, B, and are labeled as e, w, n, s, t, b, which stand for east, west, north, south, top, and bottom, respectively. While the later explanations specifically refers to the flux through the east face of a control volume (CV), the fluxes through the remaining faces of the CV can be obtained in a similar manner.
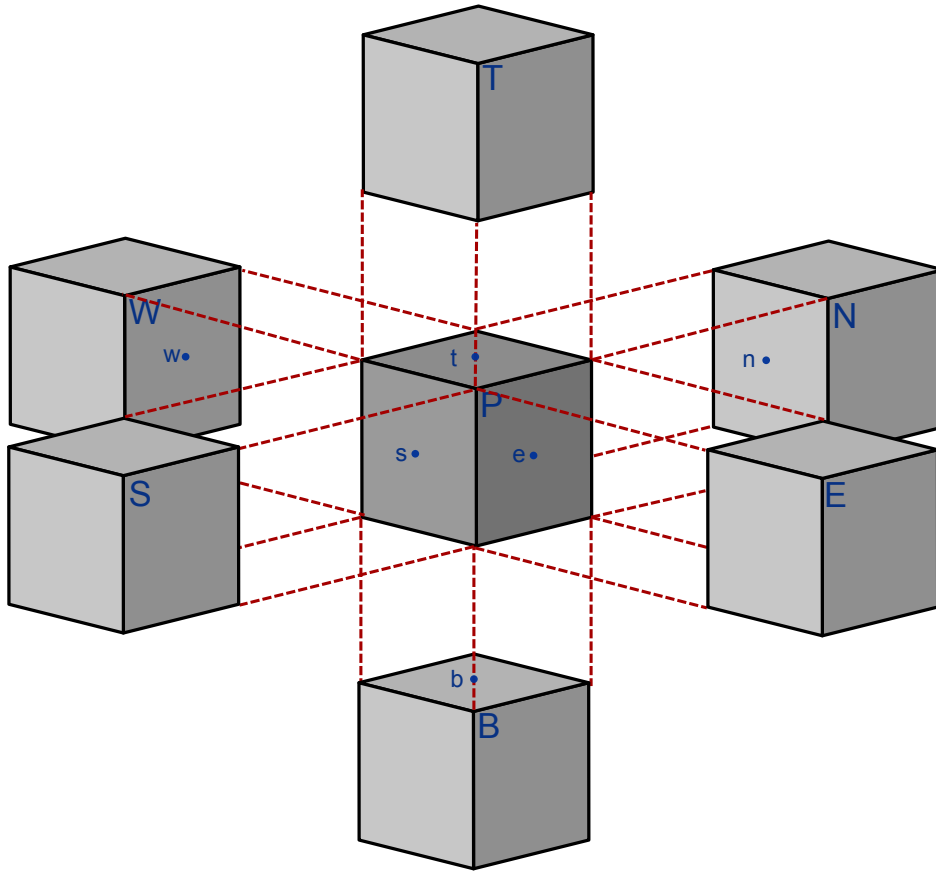
Figure 4.1 Positions and notations used for the neighboring CVs surrounding the central CV.

4.1.3 Approximation of Convective Fluxes

The convective fluxes are approximated by applying the midpoint rule through the east face, as obtained in [46]:

$$\int_{S_e} \rho v_i \phi n_i \mathrm{d}S_e \approx (\rho v_i n_i)_e \delta S_e \phi_e = \dot{m}_e \phi_e. \tag{4.3}$$

Here, $\dot{m}_e$ represents the mass flux through the east face of the control volume (CV), which has an area of δS_e. To obtain the scalar value at the surface center ϕ_e, mostly the Upwind differencing scheme (UDS), Central differencing scheme (CDS), or flux blending methods, which are explained in the following section are used.

Upwind differencing scheme

The Upwind Differencing Scheme (UDS) is a widely used numerical method for solving transport equations with advection-dominated flows. The UDS conserves mass fluxes and approximates the convective flux at the east face of a control volume by interpolating the values of the

variable at neighboring cell centers. The convective flux $\dot{m}_e\phi_e$ is calculated using values in the neighboring nodes P and E (shown in Figure 4.1) and the following formula[46]:

$$\phi_e = \begin{cases} \phi_P, & \text{if } \dot{m}_e > 0 \\ \phi_E, & \text{if } \dot{m}_e < 0 \end{cases}, \tag{4.4}$$

where ϕ_P and ϕ_E are the values of the variable at the center face and east face of the control volume, respectively.

The UDS is a simple and affordable method, but it has limitations. It provides only first-order accuracy and can generate numerical oscillations in the solution when the flow is highly skewed or discontinuous. Therefore, it is important to be aware of these limitations when applying the UDS method to numerical simulations.

Central differencing scheme

The Central Difference Scheme (CDS) approximates the convective flux at the east face of a control volume using a second-order central difference scheme that interpolates the values of the variable at neighboring cell centers. The equation 4.5 approximates ϕ_e using linear interpolation with the values in the neighboring nodes P and E (shown in Figure 4.1) using the central differencing scheme (CDS):

$$\phi_e \approx \gamma_e\phi_E + (1 - \gamma_e)\phi_P. \tag{4.5}$$

Here, the interpolation factor γ_e is determined by the following equation:

$$\gamma_e = \frac{x_e - x_P}{x_E - x_P}, \tag{4.6}$$

where ϕ_P and ϕ_E are the values of the variable at the center face and east face of the control volume, respectively.

In numerical simulations, the CDS scheme offers greater accuracy than the UDS scheme, achieving second-order accuracy in space. However, the CDS scheme can produce numerical oscillations in the solution, particularly in cases of highly skewed or discontinuous flow. To mitigate this issue, flux blending or high-resolution schemes are often employed alongside the CDS scheme. These methods provide better resolution of sharp gradients and aid in reducing numerical errors in the solution.

Flux-blending

Flux blending is a technique used to combine the advantages of different numerical schemes. It is achieved by blending the numerical fluxes obtained from different schemes in a weighted

manner. The blending can be expressed as follows:

$$\phi_e \approx (1 - \beta_\phi)\phi_e^{UDS} + \beta_\phi \phi_e^{CDS}, \tag{4.7}$$

where ϕ_e is the face value approximation, ϕ_e^{UDS} is the upwind scheme approximation, ϕ_e^{CDS} is the central differencing scheme approximation, and β_ϕ is the blending coefficient, which is a constant value between 0 and 1. By using the flux-blending technique, greater stability in calculations are achieved, which is especially useful when dealing with complex fluid dynamics problems. However, it is important to note that the blended numerical flux may still exhibit oscillations and numerical artifacts in certain flow conditions. In such cases, high-resolution schemes may be required to obtain accurate and smooth solutions.

High-resolution schemes

High-resolution (HR) schemes are a class of numerical methods used in fluid dynamics simulations to accurately capture the complex and nonlinear behavior of fluid flows. These schemes are designed to handle sharp gradients and discontinuities in the fluid flow, which are often encountered in practical applications.

One approach for developing HR schemes is the use of higher-order schemes, such as the quadratic upstream interpolation for convective kinematics (QUICK) [78]. However, these schemes can suffer from numerical instabilities, such as oscillations or overshoots, which can lead to inaccurate and unphysical results.

To overcome these issues, two numerical tools have been developed that transform the linear unbounded high-order scheme into a bounded non-linear high-resolution scheme: the total variation diminishing (TVD) approach and the normalized variable formulation (NVF).

The TVD approach, introduced by Harten [79], uses the concept of total variation to ensure that the total variation of the solution is reduced or at least conserved at each time step. The total variation is defined on the node i as:

$$TV = \sum_i |\phi_{i+1} - \phi_i|. \tag{4.8}$$

To implement the TVD approach, a flux limiter function must be proposed. One popular flux limiter function is Sweby's flux limiter function [80], which is defined as:

$$\phi_f = \phi_C + \frac{1}{2}(\phi(r))(\phi_D - \phi_C), \tag{4.9}$$

where C, D, U, and F denote center, downwind, upwind, and face, respectively, and r is defined as:

$$r = \frac{\phi_C - \phi_U}{\phi_C - \phi_D}. \tag{4.10}$$

The flux limiter function satisfies the TVD condition if the following criterion is met:

$$\phi(r) = \begin{cases} \min(2r, 2), & r > 0 \\ 0, & r \leq 0 \end{cases}. \tag{4.11}$$

The TVD approach can be expressed mathematically as:

$$TV(\phi^{n+1}) \leq TV(\phi^n). \tag{4.12}$$

The NVF approach, introduced by Leonard [81], ensures boundedness if the convection boundedness criterion (CBC) [82] is met. The normalized variable is defined as:

$$\tilde{\phi} = \frac{\phi - \phi_U}{\phi_D - \phi_U}, \tag{4.13}$$

where $\tilde{\phi}_U = 0$ and $\tilde{\phi}_D = 1$. The CBC is formulated as:

$$\begin{cases} \tilde{\phi}_C < \tilde{\phi}_f < 1, & \text{if } 0 < \tilde{\phi}_C < 1 \\ \tilde{\phi}_f = \tilde{\phi}_C, & \text{otherwise} \end{cases}. \tag{4.14}$$

In the NVF approach, the normalized variable is mapped onto a bounded function using a nonlinear mapping function, which satisfies the CBC. The mapped variable is given by:

$$\tilde{\phi}_f = f(\tilde{\phi}_C). \tag{4.15}$$

MUSCL Scheme

Another HR scheme technique, proposed by Xue, is based on the Monotonic Upstream-Centered Schemes for Conservation Laws (MUSCL) scheme , which is a popular higher-order numerical method for solving fluid dynamics problems [83]. The Xue-MUSCL scheme aims to improve the accuracy and stability of the MUSCL scheme by incorporating the TVD approach.

The flux limiter function used in the Xue-MUSCL scheme is similar to Sweby's flux limiter function, but with an additional parameter, κ:

$$\phi_f = \phi_U + \frac{1}{2}\phi(r)^{HO}(\phi_D - \phi_C), \tag{4.16}$$

$$\phi(r)^{HO} = \frac{1 + \kappa}{2} + \frac{1 - \kappa}{2}r, \tag{4.17}$$

where $-1 \leq \kappa \leq 1$. The parameter κ controls the degree of nonlinearity of the scheme, with $\kappa = 0$ corresponding to the linear upwind scheme and $\kappa = 1$ corresponding to the third-order MUSCL scheme.

The TVD condition is satisfied by the flux limiter function if it satisfies the following criterion:

$$\phi^{HO}(r) = \max\left[0, \min\left(2r, \frac{1+\kappa}{2} + \frac{1-\kappa}{2}r, 2\right)\right]. \tag{4.18}$$

The normalized variable formulation (NVF) is also used in the Xue-MUSCL scheme to ensure boundedness. The mapped variable is given by:

$$\tilde{\phi}_f^X = \begin{cases} 2\tilde{\phi_C}, & 0 < \tilde{\phi_C} < \dfrac{1+\kappa}{4+2\kappa} \\ 1 - \dfrac{\kappa}{2}\tilde{\phi_C} + \dfrac{1+\kappa}{4}, & \dfrac{1+\kappa}{4+2\kappa} < \tilde{\phi_C} < \dfrac{3-\kappa}{4-2\kappa} \\ 1, & \dfrac{3-\kappa}{4-2\kappa} < \tilde{\phi_C} < 1 \\ \tilde{\phi_C}, & \text{otherwise} \end{cases} \tag{4.19}$$

The Xue-MUSCL scheme has been shown to provide accurate and stable solutions for a wide range of fluid dynamics problems. The use of the TVD approach and NVF ensures that the scheme is capable of handling sharp gradients and discontinuities in the fluid flow while maintaining the stability and accuracy of the numerical solution. This method has been implemented in the in-house code FASTEST by Reimann [83], which contains more details on the method.

4.1.4 Approximation of Diffusive Fluxes

To approximate diffusive fluxes at cell interfaces using neighboring function values, the central differencing formula is utilized. It operates under the assumption that the function is linearly approximated between two adjacent points on the x-axis, which are represented as x_E and x_P (Figure 4.1). This leads to the following equation:

$$\left(\frac{\partial \phi}{\partial x}\right)_e \approx \frac{\phi_E - \phi_P}{x_E - x_P}. \tag{4.20}$$

Here, ϕ_E and ϕ_P represent the function values at the neighboring points on the x-axis. This formula provides an accurate estimation of diffusive fluxes and is a simple and efficient technique. It presents a second-order error for uniformly spaced grids, but for non-uniformly spaced grids, the error increases to first order [46].

4.1.5 Approximation of Integrals

To approximate the volume integral of the source term Q the midpoint rule can be used. The approximation involves evaluating the function q_ϕ at the midpoint of a control volume (CV) and multiplying it by the volume of the CV, δV. Thus, the approximation is given as:

$$Q = \int_V q_\phi dV \approx (q_\phi)_P \delta V. \tag{4.21}$$

4.1.6 Time Discretization

Numerical approximation is required for the time derivative term in Equation 4.1 when dealing with unsteady problems. The discretization involves subdividing the entire time interval $[t_0, t_f]$ into equally separated intervals of length Δt

$$t_{n+1} = t_n + \Delta t. \tag{4.22}$$

Two major types of time discretization methods are: implicit and explicit methods. Explicit methods rely on the forward difference scheme to estimate the time derivative of the unknown variable, utilizing values from the current and preceding time steps. The forward Euler method is an explicit method that utilizes the following equation:

$$\frac{\phi^{n+1} - \phi^n}{\Delta t_n} = F(\phi^n), \tag{4.23}$$

where ϕ^n represents the value of the unknown quantity at time t_n, and F represents the spatial discretization of the PDE. Explicit methods are computationally efficient, but they may suffer from stability issues and may require very small time steps to avoid numerical instability. On the other hand, implicit methods use the backward difference scheme to approximate the time derivative, which involves using values at the current and future time steps. For example, the backward Euler method is an implicit method that uses the following equation:

$$\frac{\phi^{n+1} - \phi^n}{\Delta t_n} = F(\phi^{n+1}). \tag{4.24}$$

The implicit method is more stable and can handle larger time steps, but it requires solving a system of equations at every time step, which can result in potential computational costs.

4.1.7 Assembly and Solution of the Discrete System

The momentum and continuity equations for incompressible fluids are discretized by FVM into algebraic equations. These equations are then solved by matrix algebra techniques after being

integrated over each control volume to obtain algebraic equations. The momentum equation has the form:

$$a_P^{vi} v_{i,P} + \sum_c a_c^{vi} v_{i,c} = -\delta V \left(\frac{\partial p}{\partial x_i} \right)_P + S^{v_i} = b^{v_i}.$$ (4.25)

The continuity equation is given by:

$$\sum_c \dot{m}_c = 0.$$ (4.26)

In the momentum Equation (4.25), the pressure derivative is not approximated to maintain the independence of the solution procedure from the specific numerical scheme used. This equation, along with all the control volumes (CVs) considered, forms a linear equation system that needs to be solved appropriately. However, a challenge arises in the continuity Equation (4.26) where the pressure does not appear, making it difficult to solve the equation system efficiently.

To overcome this challenge, pressure correction methods can be employed, such as the Semi-Implicit Method for Pressure-Linked Equations (SIMPLE). This widely recognized method is the standard approach in the flow solver FASTEST, which is used to solve the incompressible Navier-Stokes equations [46]. The system is typically solved iteratively until the pressure and velocity fields converge. Pressure-correction methods are based on the principle of iteratively correcting the velocities and pressure to satisfy both the continuity equation and the momentum equations.

The general procedure involves first solving the momentum equations to calculate the velocities. Subsequently, an iterative process is initiated to refine the velocities and pressure until both equations are satisfied simultaneously up to a certain threshold. This iterative approach ensures consistency between the velocities and pressure, resulting in a more accurate and reliable solution.

4.2 Computational Aeroacoustics

This section focuses on the computational approaches used in this thesis to address acoustic problems. It introduces the Finite Volume Method for Linearized Euler Equations (LEE) to provide a deeper understanding of the computational techniques utilized. Additionally, the section explores the Kirchhoff wave extrapolation method, which efficiently evaluates far-field sound. Similarly to the previous section, the computational fluid dynamics solver FASTEST is employed to compute the numerical solution.

4.2.1 Finite Volume Method for Linearized Euler Equations (LEE)

In this section, a brief description of the Finite Volume Method (FVM) used for solving the Linearized Euler Equations (LEE) is provided. The additional information on this topic can be found in [48], while [84], [85], [86] give a general overview of the FVM method for hyperbolic equations. The set of acoustic equations (2.11 - 2.13) can be expressed in matrix notation as follows:

$$\frac{\partial q}{\partial t} + A_x \frac{\partial q}{\partial x} + A_y \frac{\partial q}{\partial y} + A_z \frac{\partial q}{\partial z} = s, \tag{4.27}$$

where the vector of unknown functions, denoted as q, is defined as:

$$q = \begin{bmatrix} \rho^a \\ v_x^a \\ v_y^a \\ v_z^a \\ p^a \end{bmatrix}^T, \tag{4.28}$$

The real matrices, A_x, A_y, and A_z, take the following form:

$$A_x = \begin{bmatrix} v_x^{ic} & \rho^{ic} & 0 & 0 & 0 \\ 0 & v_x^{ic} & 0 & 0 & 1/\rho^{ic} \\ 0 & 0 & v_x^{ic} & 0 & 0 \\ 0 & 0 & 0 & v_x^{ic} & 0 \\ 0 & \rho^{ic} c_\infty^2 & 0 & 0 & v_x^{ic} \end{bmatrix}, \tag{4.29}$$

$$A_y = \begin{bmatrix} v_y^{ic} & 0 & \rho^{ic} & 0 & 0 \\ 0 & v_y^{ic} & 0 & 0 & 0 \\ 0 & 0 & v_y^{ic} & 0 & 1/\rho^{ic} \\ 0 & 0 & 0 & v_y^{ic} & 0 \\ 0 & 0 & \rho^{ic} c_\infty^2 & 0 & v_y^{ic} \end{bmatrix}, \tag{4.30}$$

$$A_z = \begin{bmatrix} v_z^{ic} & 0 & 0 & \rho_{ic} & 0 \\ 0 & v_z^{ic} & 0 & 0 & 0 \\ 0 & 0 & v_z^{ic} & 0 & 0 \\ 0 & 0 & 0 & v_z^{ic} & 1/\rho^{ic} \\ 0 & 0 & 0 & \rho^{ic} c_\infty^2 & v_z^{ic} \end{bmatrix}, \tag{4.31}$$

Furthermore, the acoustic source vector s can be expressed as:

$$s = \begin{bmatrix} 0 \\ 0 \\ 0 \\ 0 \\ -\dfrac{\partial p^{ic}}{\partial t} \end{bmatrix}. \tag{4.32}$$

By using splitting techniques, The LEE can be decomposed into 1D problems in each coordinate direction, which can be utilized in the construction of numerical methods, explained in the following section.

Homogeneous 1D LEE Solution

To solve the Linearized Euler equations for multidimensional problems, one can determine the normal and tangential acoustic velocity components using splitting techniques as detailed in [48, 84–86]. To develop FVM for hyperbolic problems, this method involves solving the one-dimensional Riemann problem normal to each cell interface. Hence, the fundamental concept of solving Riemann problems is initially addressed. The Riemann problem is an initial-boundary value problem that defines a hyperbolic differential equation with a single jump discontinuity. For instance, at the east side of a control volume at $\hat{x} = 0$:

$$\frac{\partial \hat{q}}{\partial t} + A \frac{\partial \hat{q}}{\partial \hat{x}} = 0, \tag{4.33}$$

$$\hat{q}(\hat{x}, t_0) = \begin{cases} \hat{q}_L, & \text{if } \hat{x} < 0 \\ \hat{q}_R, & \text{if } \hat{x} > 0 \end{cases}. \tag{4.34}$$

The above equation is an illustration of such a Riemann problem, as shown in Figure 4.2.

The matrix A in Equation 4.33 can be diagonalized as:

$$A = R\Lambda R^{-1}, \tag{4.35}$$

where $\Lambda = diag(\lambda_1, ..., \lambda_m)$ is the diagonal matrix of right eigenvalues, and $R = [r_1, ..., r_m]$ is the matrix of eigenvectors. The characteristic variables w are given by:

$$w = R^{-1}\hat{q}, \tag{4.36}$$

where R^{-1} is the inverse of the matrix R. This allows us to reduce the system to a set of decoupled advection equations:

$$\frac{\partial w}{\partial t} + \Lambda \frac{\partial w}{\partial \hat{x}} = 0, \tag{4.37}$$
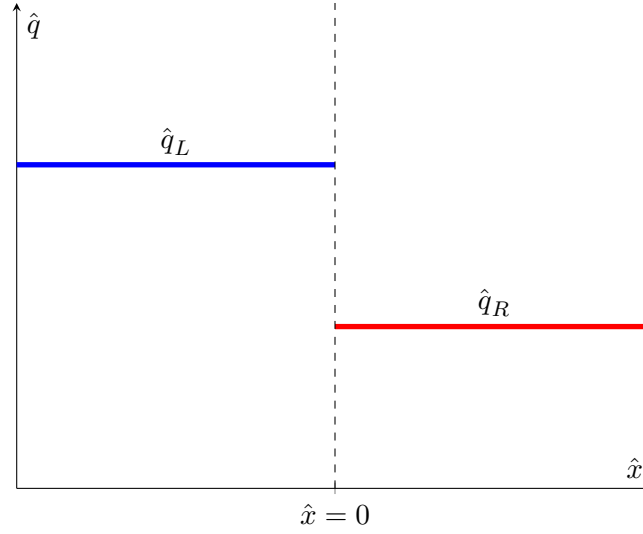
Figure 4.2 Visualizing the Riemann problem through initial data illustration.

which can be solved independently of each other. Therefore, the solution for the m-th scalar Riemann problem's characteristic variable w_m is given by:

$$w_m(\hat{x}, t) = \begin{cases} w_{m,L}, & \text{if } \hat{x} - \lambda_m t < 0 \\ w_{m,R}, & \text{if } \hat{x} - \lambda_m t > 0 \end{cases}. \tag{4.38}$$

Finally, by transforming Equation (4.38) back to physical space, the solution for the original Riemann problem Equation (4.34) is obtained as:

$$\hat{q}(\hat{x}, t) = \sum_{m:\lambda_m < \hat{x}/t} w_{m,R} r_m + \sum_{m:\lambda_m > \hat{x}/t} w_{m,L} r_m. \tag{4.39}$$

The solution of Equation (4.39) consists of m waves, each traveling at a characteristic speed λ_m. The jump in $\hat{q}$ across the m-th wave can be expressed as:

$$W_m = \alpha_m r_m, \quad \alpha = R^{-1}(\hat{q}_R - \hat{q}_L), \tag{4.40}$$

α_m represents the components of the vector α. The Equation (4.39), expressed in terms of waves, is given by:

$$\hat{q}(\hat{x}, t) = \hat{q}_L + \sum_{m:\lambda_m < \hat{x}/t} W_m = \hat{q}_R - \sum_{m:\lambda_m > \hat{x}/t} W_m. \tag{4.41}$$

Once the solution of the Riemann problem at the cell interface is known, numerical fluxes can be approximated using different methods.

In the context of a three-dimensional numerical grid, the quantity q_p^n represents an ap-

proximation of the average value over a control volume (CV) at time t_n. It can be expressed as:

$$q_p^n \approx \frac{1}{\delta V} \int_V q(x, y, z, t_n) dV. \tag{4.42}$$

The value q_p^n is stored at the midpoint of each CV, resulting in a piecewise constant distribution that represents the numerical solution at time t_n. To extend this approach to non-Cartesian, but logically rectangular grids, the capacity-form differencing [84] technique is employed. In addition to the physical grid, a computational grid with uniform grid spacing $\Delta\xi$, $\Delta\eta$, and $\Delta\zeta$ is defined. The capacity κ_P of a CV is given by:

$$\kappa_P = \frac{\delta V}{\Delta\xi\Delta\eta\Delta\zeta}. \tag{4.43}$$

Here, δV represents the volume of the CV under consideration. Since the coefficient matrix A of the augmented one-dimensional problem (referred to as Equation (4.33)) varies with spatial location, it is solved using the wave-propagation algorithm developed by Leveque [87] and also explained in [86].

The next section describes the computation of fluxes through an east side, using both an exact Riemann solver and the Lax-Wendroff method. However, the latter has a tendency to generate unphysical oscillations, hence requiring the implementation of flux limiters. Consequently, the high-resolution (HR) method is presented, which combines both techniques with appropriate flux limiters.

Godunov's method

Godunov's method is a numerical scheme used to solve hyperbolic partial differential equations (PDEs) in wave-propagation form. This first-order upwind scheme divides the computational domain into a finite number of control volumes, and computes the flux at each interface between control volumes.

The method approximates the solution using characteristic information of the PDE and calculates the flux across each interface by considering the wave propagation of the solution. To determine the numerical flux at each interface, the method uses an approximate Riemann solver, which solves the Riemann problem.

In wave-propagation form, Godunov's method can be expressed as:

$$q_P^{n+1} = q_P^n - \frac{\Delta t}{\kappa_p\Delta\xi}(A^+\Delta q_w + A^-\Delta q_e). \tag{4.44}$$

Here, A^+ and A^- are the positive and negative parts of the flux Jacobian, respectively. The solution gradient across the interface is approximated using the differences in the solution at

neighboring grid points, Δq_w and Δq_e. The positive and negative parts of the flux Jacobian are given by:

$$A^+ \Delta q_w = \sum_{m:\lambda_m > 0} (\tilde{\lambda}_m T^{-1} W_m) w, \tag{4.45}$$

$$A^- \Delta q_e = \sum m : \lambda_m < 0 (\tilde{\lambda}_m T^{-1} W_m)_e. \tag{4.46}$$

Although Godunov's method is known for its ability to accurately capture shocks, it may generate oscillations near discontinuities due to its first-order accuracy. Therefore, it is often used in combination with higher-order methods to reduce numerical errors and improve the accuracy of the solution.

Lax-Wendroff method

The Lax-Wendroff method, a second-order approach for the linear system $q_t + A q_x = 0$, employs the Taylor series expansion as follows:

$$q(x, t_{n+1}) = q(x, t_n) + \Delta t q_t(x, t_n) + \frac{1}{2}(\Delta t)^2 q_{tt}(x, t_n) + \dots . \tag{4.47}$$

Using the relationship $q_t = -A q_x$ and $q_{tt} = A^2 q_{xx}$, the following expression can be obtained:

$$q(x, t_{n+1}) = q(x, t_n) - \Delta t A q_x(x, t_n) + \frac{1}{2}(\Delta t)^2 A^2 q_{xx}(x, t_n) + \dots . \tag{4.48}$$

While the derivation presented in [84] is based on a finite difference approximation, it can alternatively be interpreted as a finite-volume method. Specifically, the method is given by [86]:

$$q_{n+1}^P = q_n^P - \frac{\Delta t}{\kappa_p \Delta \xi} \left(A^+ \Delta q_w + A^- \Delta q_e \right) + \frac{\Delta t}{\kappa_p \Delta \xi} \left(\tilde{F}_e - \tilde{F}_w \right), \tag{4.49}$$

with

$$\tilde{F}_w = \frac{1}{2} \sum_m \left(|\tilde{\lambda}_m| T^{-1} W_m \right)_w \left(\frac{\kappa_W}{\kappa_w} - \frac{\Delta t}{\kappa_w \Delta \xi} |\tilde{\lambda}\tilde{m}|_w \right), \tag{4.50}$$

where

$$\kappa_w = \frac{1}{2}(\kappa_W + \kappa_P). \tag{4.51}$$

According to [84], the correction flux $\tilde{F}$ counteracts the diffusive nature of the upwind approximation, but it exhibits an antidiffusive behavior. However, the Lax-Wendroff method can produce unphysical oscillations in the numerical solution around discontinuities, even if the solution is smooth, owing to the dispersive characteristics of the method.

High-resolution methods

To minimize oscillations near discontinuities and reduce phase errors, the high-resolution method combines the upwind method and the Lax-Wendroff method, utilizing a flux limiter function Φ to constrain the size of the second-order correction term. The value of Φ determines whether the Lax-Wendroff or upwind method is used, with $\Phi = 1$ for Lax-Wendroff and $\Phi = 0$ for upwind. To measure the degree of smoothness in the upwind direction, θ_m is assessed, and various flux limiter functions are available in the literature. The Osher and van Leer limiters have shown effective numerical performance, with the Osher limiter being symmetric only when $\beta_\Phi = 1.0$.

The high-resolution method blends the upwind and Lax-Wendroff methods using the flux limiter function Φ, expressed as:

$$\tilde{F}_w = \frac{1}{2} \sum_m \left(|\tilde{\lambda}_m| T^{-1} \tilde{W}_m \right)_w \left(\frac{\kappa_W}{\kappa_w} - \frac{\Delta t}{\kappa_w \Delta \xi} \left(|\tilde{\lambda}_m| \right)_w \right), \tag{4.52}$$

where $\tilde{W}_m$ is defined as:

$$(\tilde{W}m)_w = (\alpha_m r_m \Phi(\theta m, w))_w. \tag{4.53}$$

The degree of smoothness in the upwind direction is measured by $\theta_{m,w}$, which is given by:

$$\theta_{m,w} = \begin{cases} \dfrac{\alpha_{m,ww}}{\alpha_{m,w}}, & \text{if } \tilde{\lambda}m, w > 0 \\ \dfrac{\alpha m, e}{\alpha_{m,w}}, & \text{if } \tilde{\lambda}_{m,w} < 0 \end{cases}. \tag{4.54}$$

The van Leer limiter is expressed as:

$$\Phi(\theta) = \frac{\theta + |\theta|}{1 + |\theta|}. \tag{4.55}$$

And the Osher limiter is expressed as:

$$\Phi(\theta) = \max\left[0, \min(\theta, \beta_\Phi)\right] \quad \text{with} \quad \beta_\Phi \in [1, 2]. \tag{4.56}$$

4.2.2 Finite Volume Method for Source Term

In order to accurately model the process of acoustic generation, the source term, denoted as $\tilde{Q}$, in the general equation expressed as:

$$\frac{\partial U}{\partial t} = \tilde{Q}, \tag{4.57}$$

must be appropriately solved. One popular way to do this is by utilizing a forward Euler scheme.

Acoustic simulations require much smaller time step sizes (Δt^{CAA}) compared to fluid dynamic simulations (Δt^{CFD}), posing a challenge in computing efficiently due to the difference in time and length scales between acoustic waves and small-scale turbulence structures. The frozen fluid approach [48] is used to address this issue by updating aeroacoustic source terms every N-th acoustic time step, where $N = \Delta t^{CFD}/\Delta t^{CAA}$.

To update the acoustic variable at time t_{n+1}, the following equation can be used:

$$q_p^{n+1} = q_p^n + \Delta t^{CAA}\tilde{Q}. \tag{4.58}$$

4.2.3 Long-Span Bodies

Turbulent flow simulations over long bodies with a span length of L present a challenge in accurately capturing the spanwise-correlated flow structure. To reduce computational costs, periodic boundary conditions are often applied in the spanwise direction of the computational domain, with the simulated span length L_s typically being of the order of the turbulent length scales. However, when it comes to acoustic calculations, applying periodic boundary conditions to the same spanwise width results in unphysically correlated acoustic results due to the much larger acoustic wavelength compared to the turbulence length scales [88].

To address this issue, one approach is to use a very long span that fully covers the acoustic correlation length, which is often not feasible. Alternatively, an absorbing boundary condition can be applied at the spanwise boundaries. However, this is impossible or computationally expensive. To overcome these challenges, approximated but computationally efficient approaches has been developed [89, 90]. One approach involves calculating a two-dimensional acoustic field at zero spanwise wavenumber, in the mid-span plane [89]. The acoustic sources and hydrodynamic variables are integrated in the spanwise direction, allowing for different treatment of spanwise boundary conditions for flow and acoustics. This is achieved by integrating the pressure distribution over the spanwise direction using the following equation:

$$\tilde{s}(x, y, t) = \int_{-L_s/2}^{L_s/2} s(x, y, z, t)dz. \tag{4.59}$$

The two-dimensional pressure distribution can be transformed into the three dimensional spectral domain using the following equation:

$$p^a(x, y, 0, \omega) \approx \widetilde{p}^a(x, y, \omega)\frac{1+i}{2}\sqrt{\frac{\omega}{c_\infty \pi r}}, \tag{4.60}$$

where $r = \sqrt{x^2 + y^2}$. The full derivation of the method is available in Oberai et al. [89]. A Schematic presentation of the long span body method and span lengths is shown in Figure 4.3.
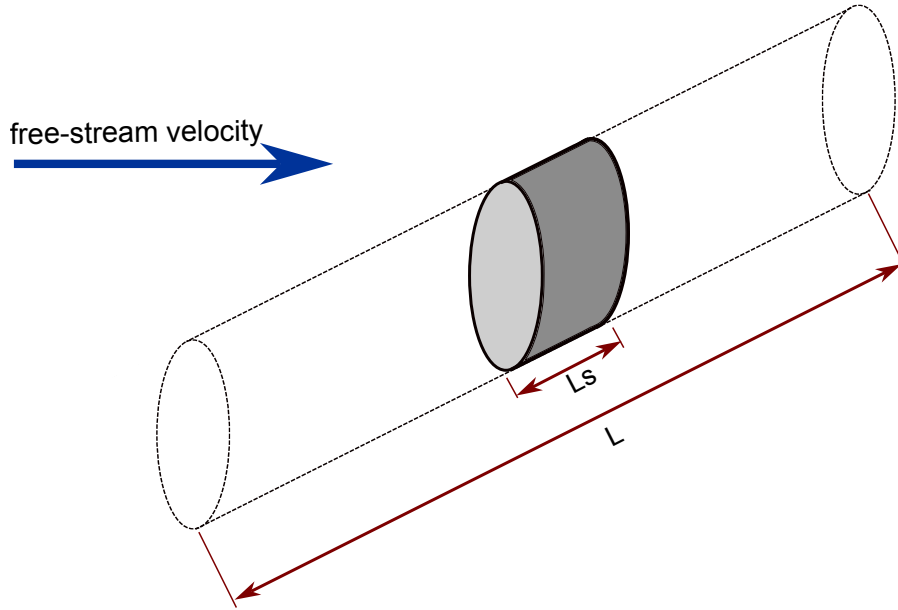
Figure 4.3 Schematic of aerodynamic noise prediction method for a Long-Span circular cylinder.

Next, the simulated spanwise pressure is used to calculate the sound pressure level (SPL) at a given receiver location using the following equation:

$$SPL_s = 20 \log \left(\frac{p^a}{p_{ref}} \right), \tag{4.61}$$

where p^a is the simulated pressure amplitude, and p_{ref} is the reference pressure amplitude, typically taken to be $20 \mu Pa$. However, the SPL_s calculated using Equation (4.61) only represents the noise generated for the simulated span L_s. To obtain the SPL for the full span L , the following equation is proposed by Seo and Moon [36]:

$$SPL = SPL_s + \begin{cases} 10 \log \left(L/L_s \right) & \text{if } L_c/L_s \leq 1/\sqrt{\pi}, \\ 10 \log \left(L_c/L_s \right) + 10 \log \left(\sqrt{\pi} L/L_s \right) & \text{if } 1/\sqrt{\pi} < L_c/L_s < L/\sqrt{\pi} L_s, \\ 20 \log \left(L/L_s \right) & \text{if } L_c/L_s \geq L/\sqrt{\pi} L_s, \end{cases} \tag{4.62}$$

where L_c is acoustic spanwise coherence length, and can be replaced by spanwise coherence length of the surface pressure at a point of interest, which is usually a known value from experimental measurements. The complete derivation of the method is available in [36].

4.2.4 The Kirchhoff Method

To accurately compute far-field noise in low Mach number turbulent flows, a method combining the hydrodynamic/acoustic splitting approach with the Kirchhoff wave extrapolation technique is employed. This method allows for precise solutions in the near and mid-field, as well as the determination of sound pressure at any point in the far-field with a computational time independent of the observer's distance.

The process involves several steps. First, an unsteady turbulent flow field is computed using methods like LES or Hybrid LES/RANS. From this solution, the acoustic sources are identified, and the resulting flow-induced acoustic field is calculated. Surface data, including the acoustic pressure and its spatial derivatives on the Kirchhoff surface (S_k), are recorded, matching the fluid dynamic time step to minimize data storage requirements. The recorded data is then transformed into the frequency domain, and the Kirchhoff formula is applied to each point on the Kirchhoff surface. This process is repeated until the simulation reaches its designated end time, and finally, the data is post-processed using the Fast Fourier Transform (FFT) algorithm in MATLAB [91].

The Kirchhoff method solves the Helmholtz equation for the sound pressure on a closed surface that encloses the the flow domain. The Kirchhoff surface, S_k, is chosen to encompass the entire domain, and the sound pressure on this surface is integrated to determine the far-field sound radiation.

One of the notable advantages of the Kirchhoff method is its efficiency in predicting far-field sound radiation from complex flow configurations. The 2-D frequency domain form of the Kirchhoff formulation, accounting for the impact of a mean flow in the observation region, is derived in [92], and its implementation in FASTEST is validated in [86]. The equation for the Kirchhoff method in the frequency domain can be expressed as:

$$
H(f)p^a(x,\omega) = \frac{i\beta}{4}\int_{S_k}\left\{\frac{\partial p_a(x',\omega)}{\partial x'_i}H_0^{(2)}\left(\frac{k\beta}{r_\beta}\right) + \frac{kp_a(x',\omega)}{\beta^2}\left[\frac{\partial r_\beta}{\partial x'_i}H_1^{(2)}\left(\frac{k\beta}{r_\beta}\right)\right.\right.
$$
$$
\left.\left. - iMa\frac{\partial x'_1}{\partial x'_i}H_0^{(2)}\left(\frac{k\beta}{r_\beta}\right)\right]\right\}e^{i\left(\frac{Mak_1r_1}{\beta^2}\right)}(n_i - Ma^2n_1)dS_k,
$$

(4.63)

with

$$
r_\beta = \sqrt{(x_1 - x'_1)^2 + \beta^2(x_2 - x'_2)^2},
$$

(4.64)

where $\beta = \sqrt{1 - Ma^2}$ is the Prandtl-Glauert factor and $k = \omega/c_\infty$ is the wave number, and $i = \sqrt{-1}$. The Heaviside step function is represented by $H(f)$, where it equals 0 if f is less than 0, and equals 1 if f is greater than or equal to 0. The unit normal vector on the Kirchhoff surface

is represented by n_i and points outward. The Hankel function of order j and second kind is denoted by $H_j^{(2)}$. The expression provides the acoustic pressure at any position outside the source region as a function of the acoustic pressure and its spatial derivatives on the Kirchhoff surface.

5 Validation and Verification

This chapter evaluates the performance of the FASTEST-Implemented SSV-PANS method in simulating the Fully Developed Turbulent Channel Flow and the periodic 2D hill test cases as benchmark test cases. The accuracy of the model is assessed by comparing its predictions with reference data through an extensive study, and the results demonstrate excellent agreement, validating the reliability and effectiveness of the implemented SSV-PANS method for simulating complex fluid flows in the context of aeroacoustics.

5.1 Test Case 1: Fully Developed Turbulent Channel Flow

The second case for validating the SSV-PANS model involves studying a fully developed turbulent channel flow (Figure 5.1). The Reynolds number based on the wall friction velocity u_τ, the channel half width δ, and the kinematic viscosity ν is $Re_\tau = 650$.

To ensure consistency with reference models [76, 93], the computational domain's size, as depicted in Figure 5.1, has been carefully chosen. The domain has a length of $2\pi\delta$ in the x direction, a height of 2δ in the y direction, and a width of $\pi\delta$ in the z direction, denoted as L_x, L_y, and L_z, respectively. This specific domain size enables direct comparison with existing results and facilitates accurate evaluation of the simulation's performance.

In the simulation, the stream-wise and span-wise directions are assumed to be periodic, while the top and bottom walls have no-slip boundary conditions. This means that the fluid's velocity is set to zero at these walls, representing the adherence of the fluid to the wall.

The simulation employs a computational grid composed of $64 \times 100 \times 64$ cells, as illustrated in Figure 5.2. The size and distribution of the grid cells have been carefully designed to ensure accurate representation of the flow. In particular, the dimensionless distance of the first cell to the wall, is $y^+ \approx 1$, which is important for resolving near-wall turbulent structures.

A stream-wise pressure gradient drives the flow in the channel, enabling its sustenance. The simulation is run for a duration exceeding 30 flow-through times to achieve statistically stable results. This extended duration allows for capturing the fully developed turbulent behavior of the flow.

The central differencing scheme is employed for the convection term and the Second-Order Fully Implicit scheme is utilized for time discretization.
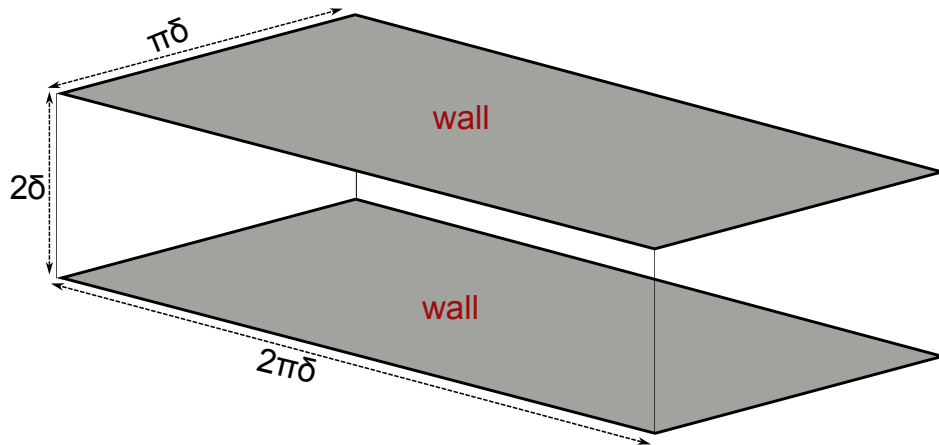
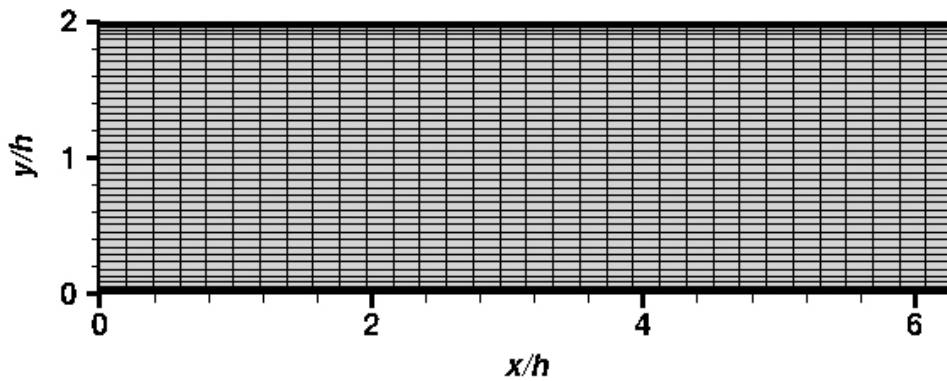**Figure 5.1** Schematic view of the channel flow.

Figure 5.2 The channel flow's computational domain discretization (every 2 lines are shown).

The results of the current test case have been compared with the findings of Girimaji et al. [76], who also employed the SSV-PANS method, as well as the direct numerical simulation (DNS) data of Iwamoto et al. [93]. This comparative analysis allows for a comprehensive evaluation of the SSV-PANS method's accuracy and reliability in capturing the behavior of fully developed turbulent channel flow. By comparing the SSV-PANS results with both the study by Girimaji et al. [76] and the DNS data of Iwamoto et al. [93], it becomes possible to assess the consistency, agreement, and performance of the SSV-PANS method in reproducing key flow features, providing valuable insights for further research in the field of aeroacoustics and related areas.

To visualize the velocity distribution in the stream-wise direction of the channel flow, obtained through the SSV-PANS method, Figure 5.3 is presented. This figure displays the instantaneous velocity field, offering insights into the unsteady flow features within the channel. It is

54

evident that the SSV-PANS simulation accurately captures these unsteady flow characteristics, highlighting its effectiveness in reproducing the complex dynamics of turbulent channel flow.
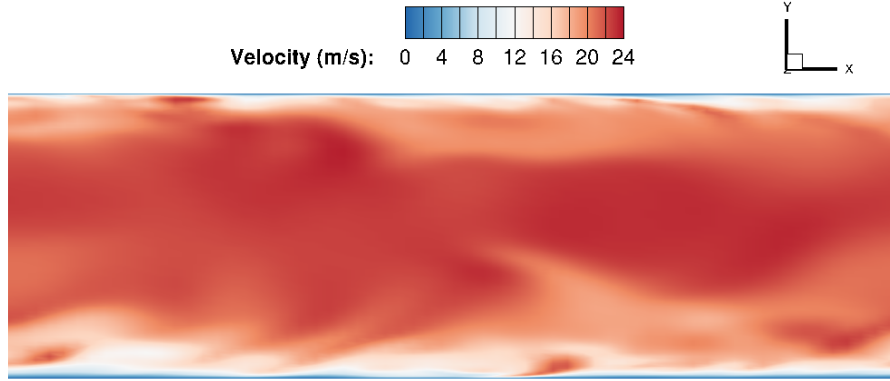

Figure 5.3 Transient velocity field obtained by SSV-PANS method.

The f_k parameter, as shown in Figure 5.4, exhibits values and behavior that are in line with the findings reported by Girimaji et al. [76]. In this analysis, it is observed that the near-wall values of f_k are equal to 1, indicating a RANS-like behavior near the wall where the flow features are modeled. As the flow moves away from the wall and progresses into the bulk region, the f_k parameter gradually decreases, reaching a minimum value of approximately 0.3. This decrease in f_k signifies an enhancement in the resolution of flow features and a more accurate representation of the turbulence characteristics, which is consistent with the observations made by Girimaji et al. [76].
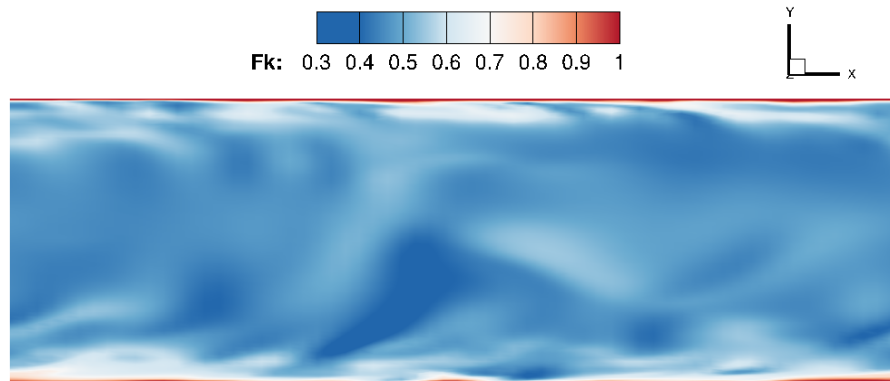
Figure 5.4 Kinetic energy resolution parameter (f_k) for the fully-developed flow in a plane channel obtained using the SSV-PANS method.

It is crucial to emphasize again that the values calculated for f_k using Equation (3.69) should consistently exceed k_u/k at the conclusion of the time step. This is demonstrated for the channel flow in Figure 5.5, and when comparing it with Figure 5.4, it becomes evident that the values of f_k are larger than the final valeus of k_u/k.
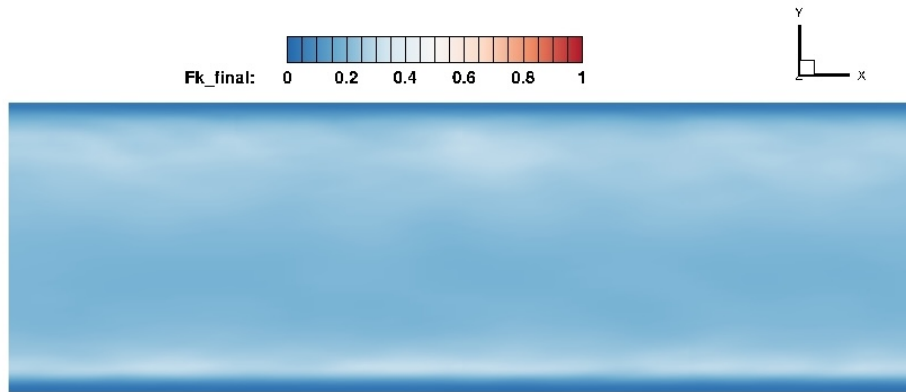
Figure 5.5 Unresolved to total kinetic energy (k_u/k) for the fully-developed flow in a plane channel obtained using the SSV-PANS method.

The log-law behavior of the mean velocity, as illustrated in Figure 5.6, provides strong evidence for the accuracy of the simulation conducted using the SSV-PANS method. This log-law behavior is a characteristic feature of turbulent flows near a wall, where the mean velocity profile follows a logarithmic trend as a function of the distance from the wall. The agreement between the simulated mean velocity profile and experimental data further strengthens the notion that the simulation captures essential flow characteristics with high fidelity. The consistency observed between the simulation results, the SSV-PANS study by Girimaji et al. [76], and the DNS data of Iwamoto et al. [93] suggests that the SSV-PANS method successfully reproduces the log-law behavior and provides an accurate representation of the flow physics.

Furthermore, the normalized root-mean-squared (r.m.s) velocity fluctuations are presented in Figure 5.7, compared with the references by Girimaji et al. [76] and Iwamoto et al. [93]. This figure provides valuable insights into the spatial distribution of the various r.m.s. components and enables an assessment of their expected behavior. The observed patterns of the r.m.s. velocity fluctuations align with anticipated trends, demonstrating consistency with previous studies. The comparison with the SSV-PANS results by Girimaji et al. [76] and the DNS data by Iwamoto et al. [93] further confirms the accuracy and reliability of the SSV-PANS method in capturing and representing the turbulent characteristics of the channel flow. These results highlight the capability of the SSV-PANS method to accurately reproduce the spatial distribution of velocity fluctuations, thus providing valuable insights for understanding the turbulent behavior within the channel flow.

Figure 5.8 displays semi-log profiles of normalized r.m.s velocity fluctuations as a function of the dimensionless wall distance for fully developed turbulent channel flow. This plot offers valuable insights into the behavior of turbulence near the wall in comparison with the data obtained from DNS results of Iwamoto et al. [93] and the SSV-PANS simulations conducted by
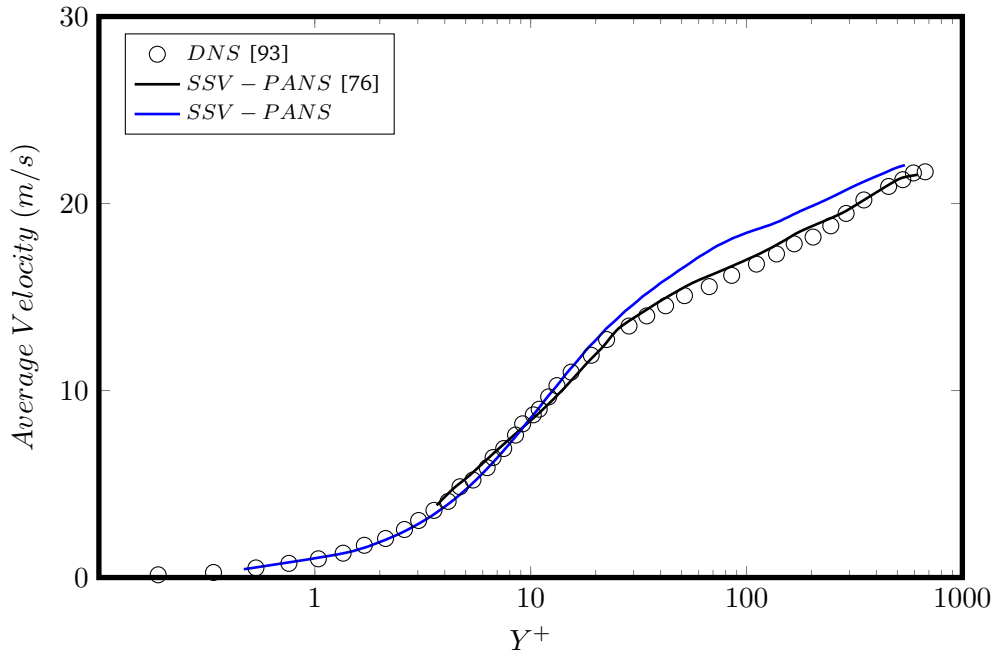
Figure 5.6 Normalized mean velocity in channel flow in comparison with SSV-PANS [76] and DNS[93].
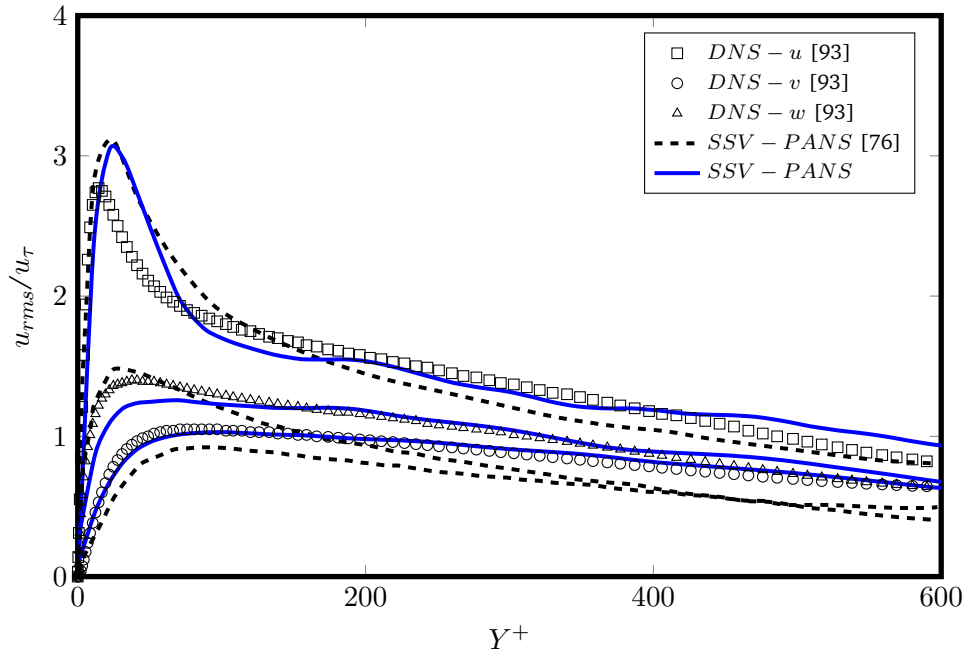

Figure 5.7 Normalized r.m.s velocity fluctuation in comparison with SSV-PANS[76] and DNS [93].

Girimaji et al. [76]. The SSV-PANS results closely match both the DNS data and the SSV-PANS data in terms of the log-law trend and overall accuracy. This agreement is a clear indication of

the accuracy of the SSV-PANS method in capturing the turbulence characteristics near the wall. Nevertheless, the slight deviation from the DNS data is expected, as near-wall turbulence is challenging to model accurately due to the complex interactions between the flow and the wall. Nonetheless, the overall agreement between the SSV-PANS results and the DNS data indicates that the SSV-PANS method is a reliable tool for simulating turbulence in fully developed channel flow.
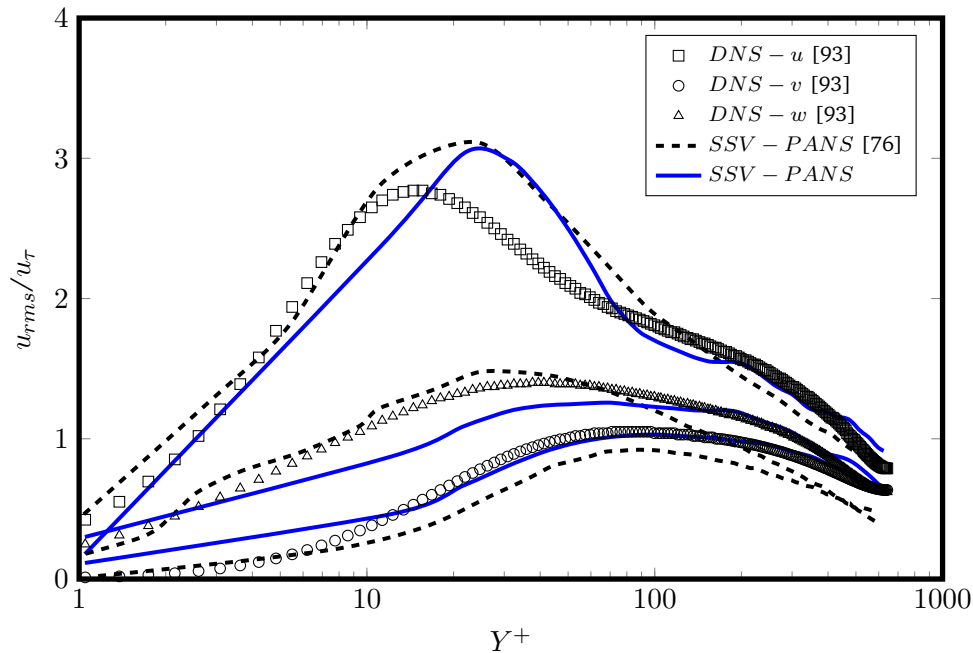

Figure 5.8 Semi-log profiles of normalized r.m.s velocity fluctuation in comparison with SSV-PANS[76] and DNS [93].

Figure 5.9 and Figure 5.10 showcases the behavior of normalized Reynolds stress profiles in relation to the dimensionless wall distance. This illustration allows for a direct comparison with DNS data from Iwamoto et al. [93]. The agreement between the SSV-PANS simulations and the DNS data underscores the proficiency of the SSV-PANS method in faithfully capturing the subtleties of near-wall turbulence characteristics.

In conclusion, the implemented SSV-PANS method has demonstrated its capability to accurately replicate flow details with a high level of precision in the context of fully developed turbulent channel flow. The observed agreement between the simulation results and the reference data of previous studies by Girimaji et al. [76] and Iwamoto et al. [93], highlights the effectiveness of the SSV-PANS method in capturing key flow features and turbulence phenomena. These findings not only validate the accuracy and reliability of the SSV-PANS method but also establish its suitability for further research in the field of aeroacoustics and related areas. Accurate characterization of flow behavior is crucial for in-depth analysis and understanding,
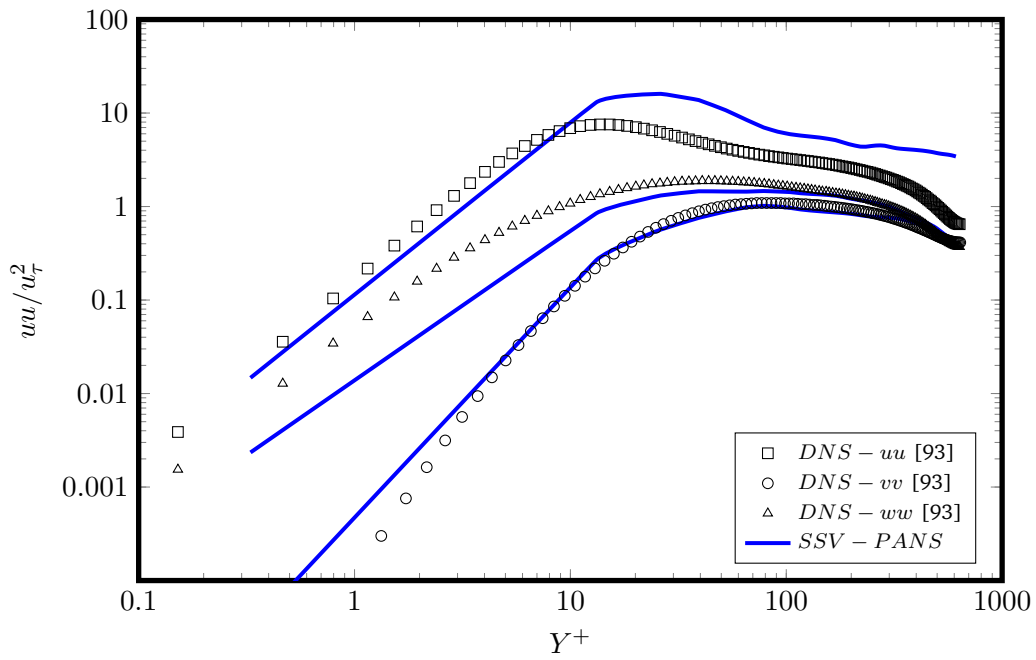
Figure 5.9 Normalized Reynolds stress profiles of $\overline{u'u'}/u_\tau^2$ in comparison with DNS [93].
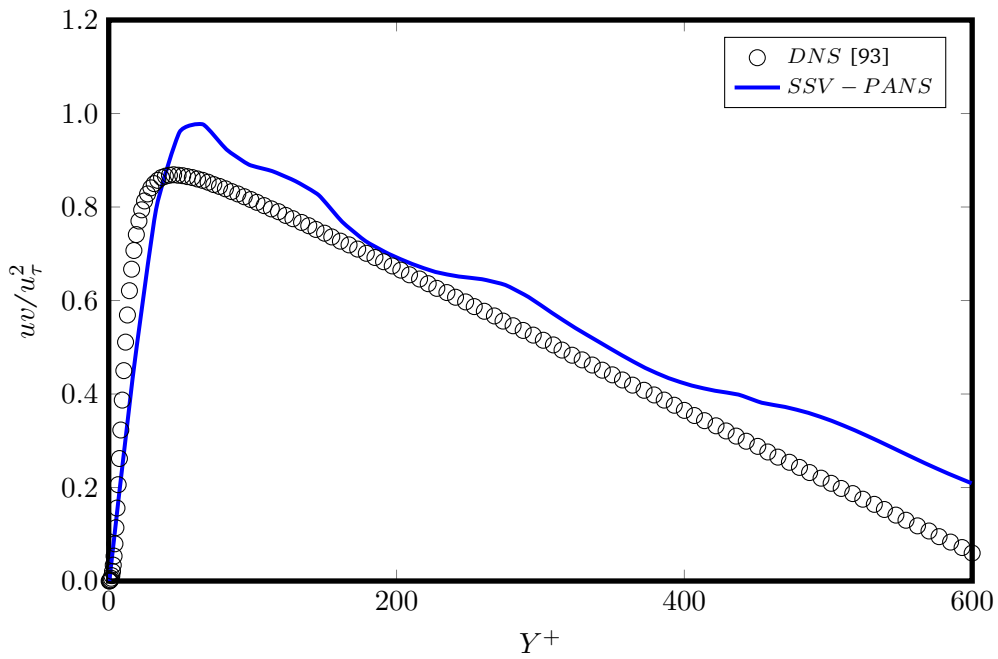

Figure 5.10 Normalized Reynolds stress profiles of $\overline{u'v'}/u_\tau^2$ in comparison with DNS [93].

and the SSV-PANS method provides a valuable tool for achieving these goals.

59

5.2 Test Case 2: Periodic 2D Hill

To evaluate the accuracy of the SSV-PANS model implementation in the FASTEST flow solver, the periodic 2D hill test case is employed as a benchmark. This widely used test case serves as a rigorous validation scenario due to its complex flow pattern, making it an ideal choice for assessing the model's capability to accurately predict flow separation and reattachment points. The comparison of the SSV-PANS model's results with the reference LES data by Fröhlich et al. [1] provides a robust validation metric, ensuring the reliability and effectiveness of the implemented SSV-PANS method in simulating complex fluid flows.

The computational domain for this test case is defined as a channel with specific dimensions: a length of $L_x = 9h$, a height of $L_y = 3.035h$, and a span-wise length of $L_z = 4.5h$, where h represents the height of the hill. The top and bottom edges of the channel are considered as no-slip wall boundary conditions, while the stream-wise and span-wise directions are treated as periodic boundaries. The entire computational domain is discretized into 0.7×10^6 control volumes (CVs), as illustrated in Figure 5.11.

It is important to note that the first cell near the wall lies within the viscous sublayer, with a non-dimensional wall distance $y^+ \approx 1$.
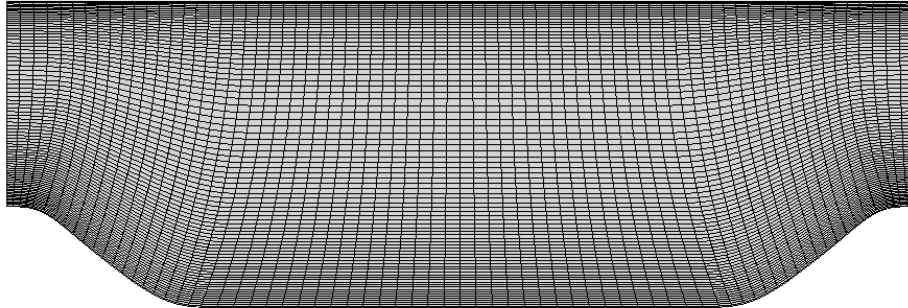
Figure 5.11 Computational grid for the 2D periodic hill test case (every 2 lines are shown).

To ensure accurate results, the simulation is carried out for 50 flow-through cycles, allowing sufficient time averaging to obtain the mean flow quantities. These mean flow quantities are then compared with the reference LES results provided by Fröhlich et al. in their study [1]. The reference LES simulation employs 4.6×10^6 CVs and serves as a reliable metric for comparing the accuracy of the SSV-PANS model. The Reynolds number, which is defined based on the bulk velocity, can be calculated as:

$$\mathrm{Re}_b = \frac{u_b h}{\nu} = 10595. \tag{5.1}$$

Here, u_b represents the bulk velocity, h is the hill height, and ν denotes the kinematic viscosity. To achieve the desired bulk velocity, a pressure gradient is applied to the flow.

The averaged stream-wise velocity contour obtained using the SSV-PANS method is shown in Figure 5.12.
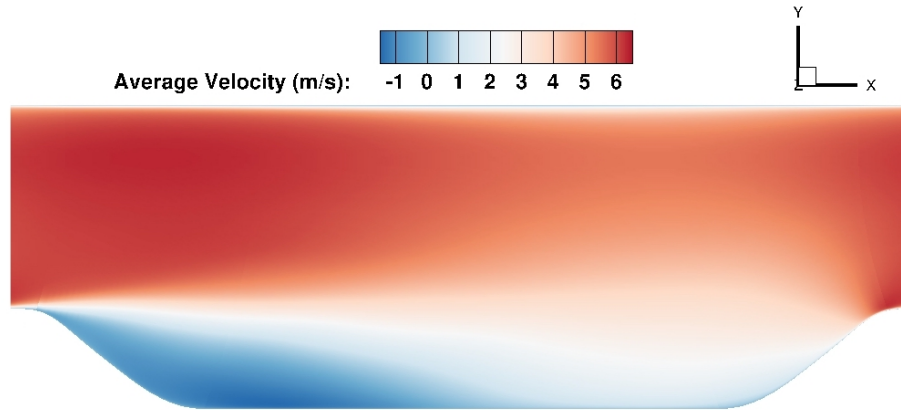
Figure 5.12 Average velocity field of the flow past the periodic 2D hills obtained using the SSV-PANS method.

In addition to the stream-wise velocity contour, the streamlines in Figure 5.13 reveal perfectly the flow pattern. At the inflow, there is a re-circulation region separated from the mainstream, followed by reattachment in the middle of the bottom wall. This intricate flow behavior poses a significant challenge for accurate prediction and serves as an ideal benchmark for testing the performance of computational fluid dynamics (CFD) models.
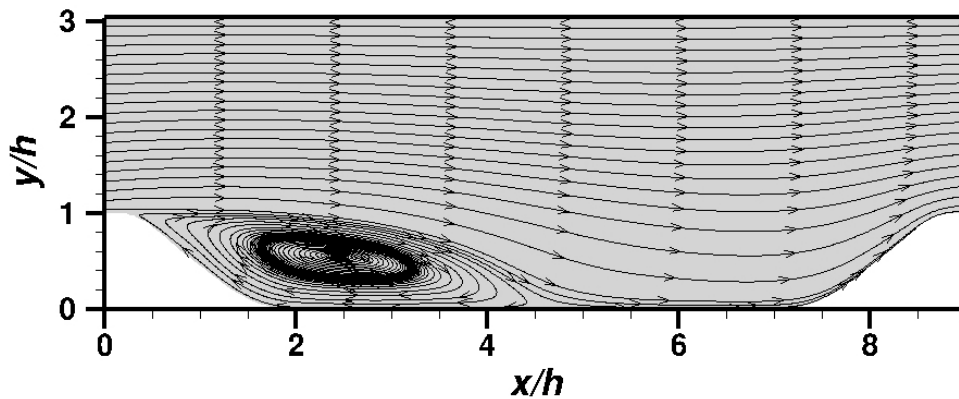
Figure 5.13 Streamlines of the flow past the periodic 2D hills obtained using the SSV-PANS method.

Furthermore, the calculated values of the kinetic energy resolution parameter, f_k, are depicted in Figure 5.14, ranging from 0.3 to 1. Notably, the values near the wall are equal to 1.

It's important to note that the comparison of f_k values has been carried out once again for the 2D Hill. When comparing it with Figure Figure 5.14, it becomes evident that the values of f_k are greater than the final values shown in Figure 5.15.
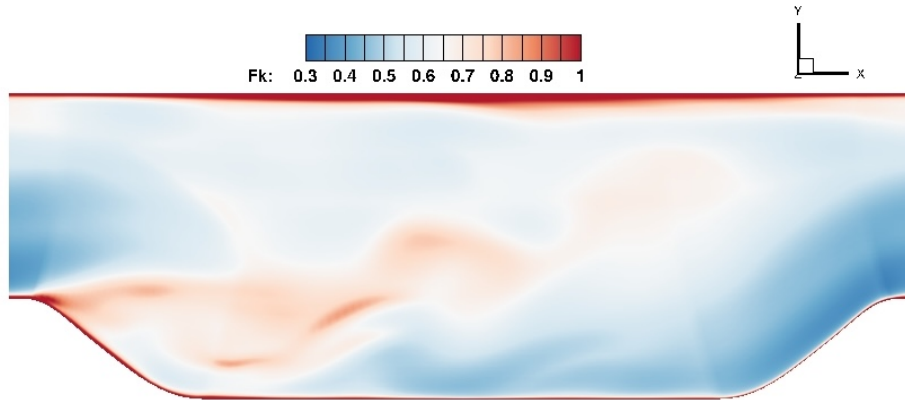
Figure 5.14 Kinetic energy resolution parameter (f_k) for the flow past the periodic 2D hills obtained using the SSV-PANS method.
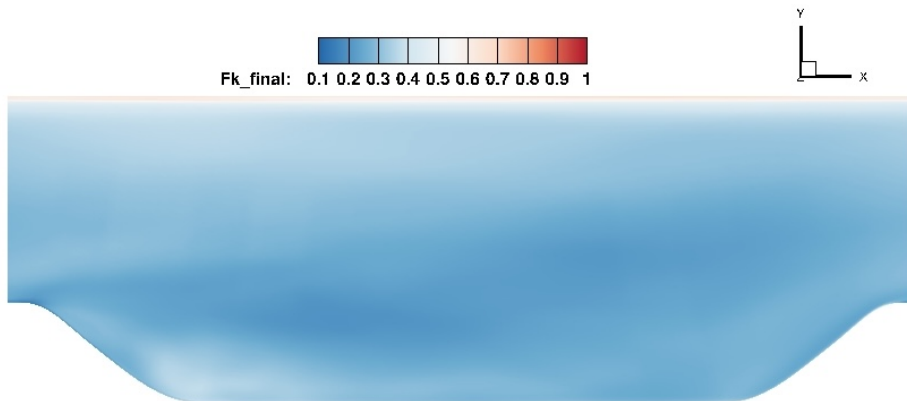
Figure 5.15 Unresolved to total kinetic energy (k_u/k) for the flow past the periodic 2D hills obtained using the SSV-PANS method.

To assess the accuracy of the SSV-PANS results, a comparison was made with the LES results obtained by Fröhlich et al. [94]. The skin friction coefficient, $C_f = \tau_w / \frac{1}{2}\rho U_0^2$, which is a crucial parameter indicating flow separation and reattachment from the bottom wall, was analyzed. The results are presented in Figure 5.16. The point where the skin friction coefficient first becomes zero represents the location of flow separation from the bottom wall. Conversely, the second time it becomes zero indicates the point of flow reattachment to the wall. Accurately predicting these separation and reattachment points is crucial for evaluating the model's capability. Table 5.1 provides the locations of these points.

Based on the comparison of the SSV-PANS model's results with the reference data, it can be confidently concluded that the model is capable of accurately predicting the flow separation and reattachment points, as well as the distribution of the skin friction coefficient along the bottom
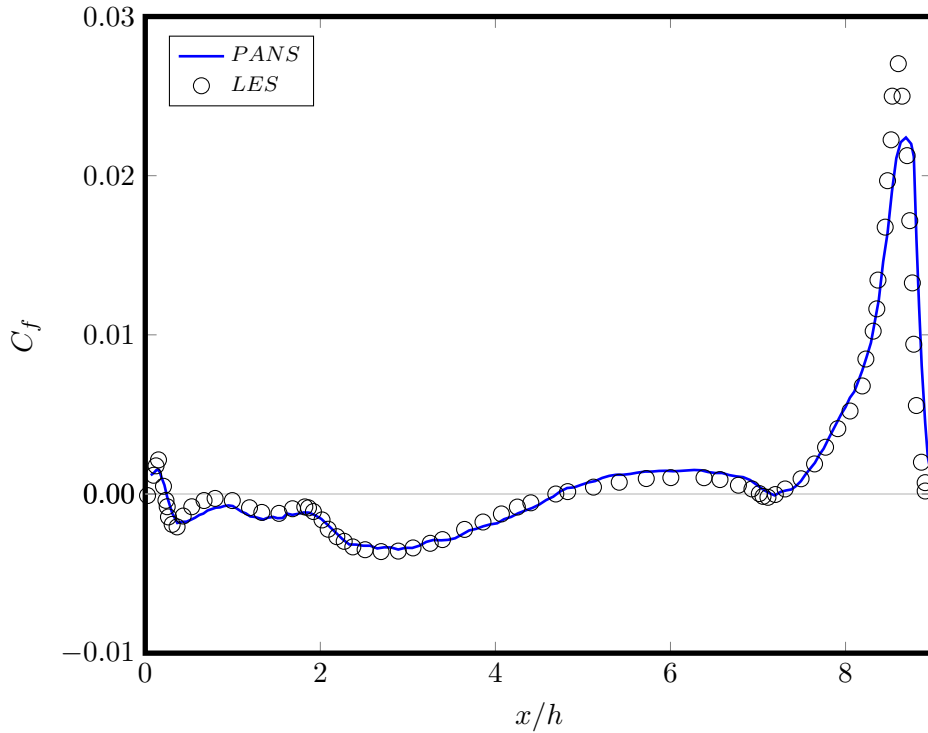
Figure 5.16 2D hill's skin friction coefficient obtained by SSV-PANS in comparison with LES [94].

Table 5.1 Separation and reattachment points obtained by SSV-PANS in comparison with LES [94].

	LES[94]	SSV-PANS
Separation point (x_s/h)	0.22	0.24
Reattachment point (x_r/h)	4.72	4.70

wall. These findings strongly indicate that the SSV-PANS model is a reliable and effective tool for simulating complex fluid flows, such as the periodic 2D hill test case.

To further verify the accuracy of the SSV-PANS model, the time-averaged streamwise and wall-normal velocities were thoroughly investigated and compared with the LES results at six different positions in the x-direction. The streamwise velocity profiles were compared with reference LES data [94], and it was observed that the SSV-PANS simulation results exhibited excellent agreement with the reference LES data. Additionally, the wall-normal velocity profiles, as depicted in Figure 5.18, also demonstrated good agreement with the reference LES data [94]. Only, for the position $x/h = 0.5$, negligible variances can be observed.

Furthermore, the SSV-PANS simulations were utilized to obtain Reynolds stress profiles $\overline{u'u'}$ and $\overline{u'v'}$, which exhibited very good agreement with the reference LES data [94], as shown in Figures 5.19 and 5.20. These results further support the conclusion that the SSV-PANS model is a reliable and effective tool for simulating complex fluid flows.

In conclusion, the newly implemented SSV-PANS model provides satisfactory simulation outcomes and has been successfully validated for further investigations. It demonstrates strong agreement with reference LES data and can be relied upon for accurate predictions in similar flow scenarios.

(a) $x/h = 0.05$

(b) $x/h = 0.5$

(c) $x/h = 2$

(d) $x/h = 4$

(e) $x/h = 6$

(f) $x/h = 8$
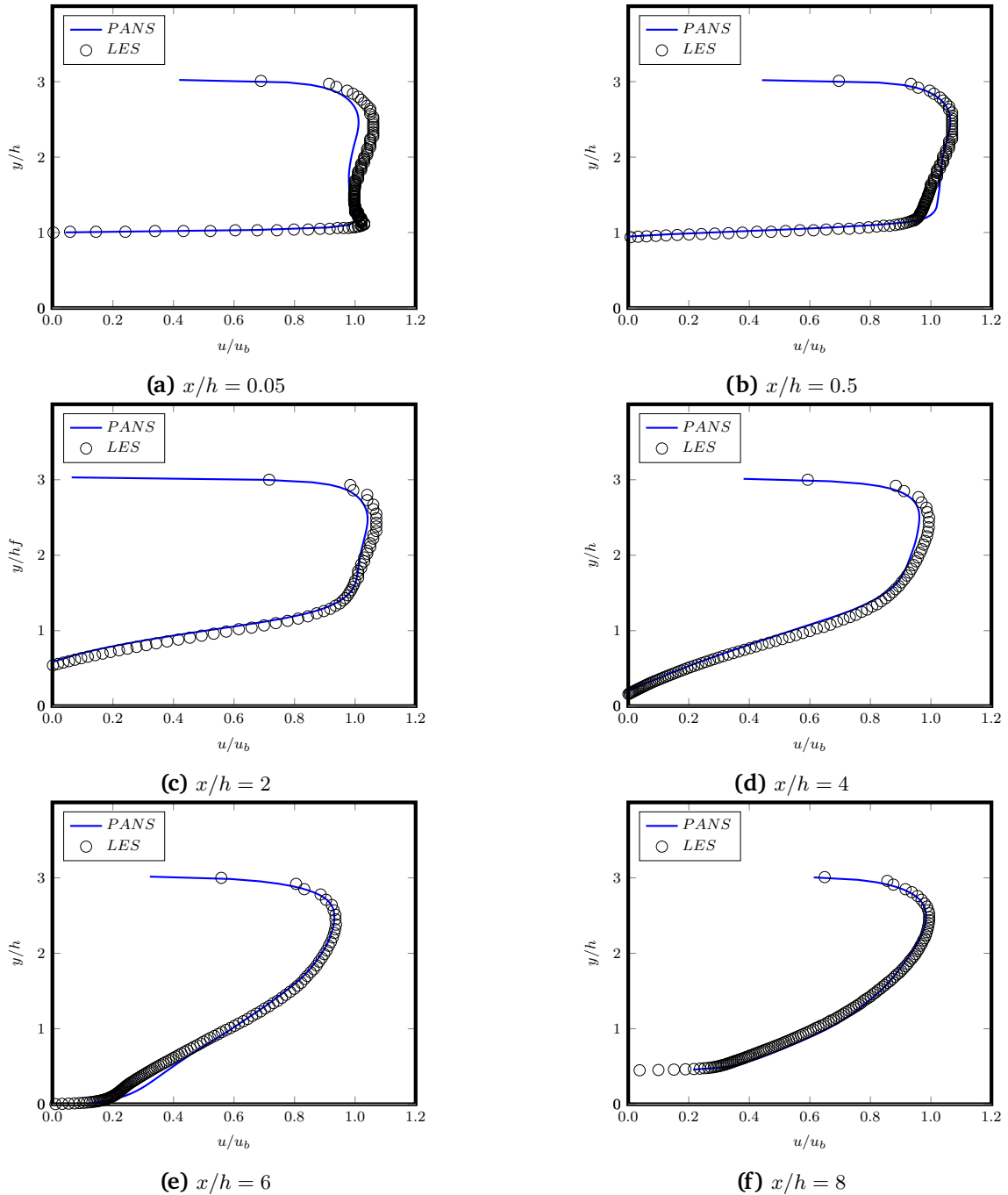
Figure 5.17 Mean velocity profiles along the streamwise direction in comparison with LES [94].

(a) $x/h = 0.05$

(b) $x/h = 0.5$

(c) $x/h = 2$

(d) $x/h = 4$

(e) $x/h = 6$

(f) $x/h = 8$
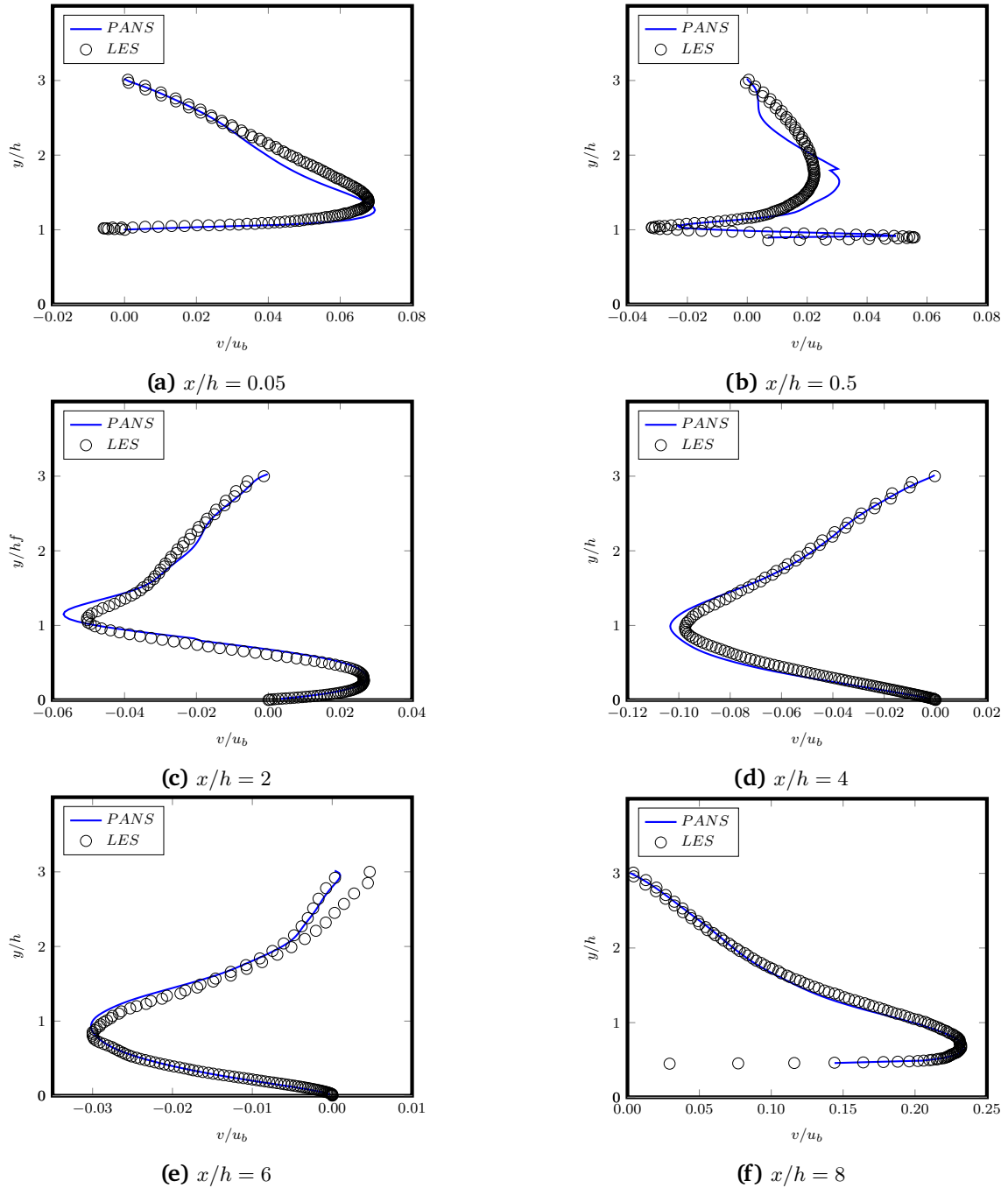
Figure 5.18 Mean velocity profiles along the wall normal in comparison with LES [94].

(a) $x/h = 0.05$

(b) $x/h = 0.5$

(c) $x/h = 2$

(d) $x/h = 4$

(e) $x/h = 6$

(f) $x/h = 8$
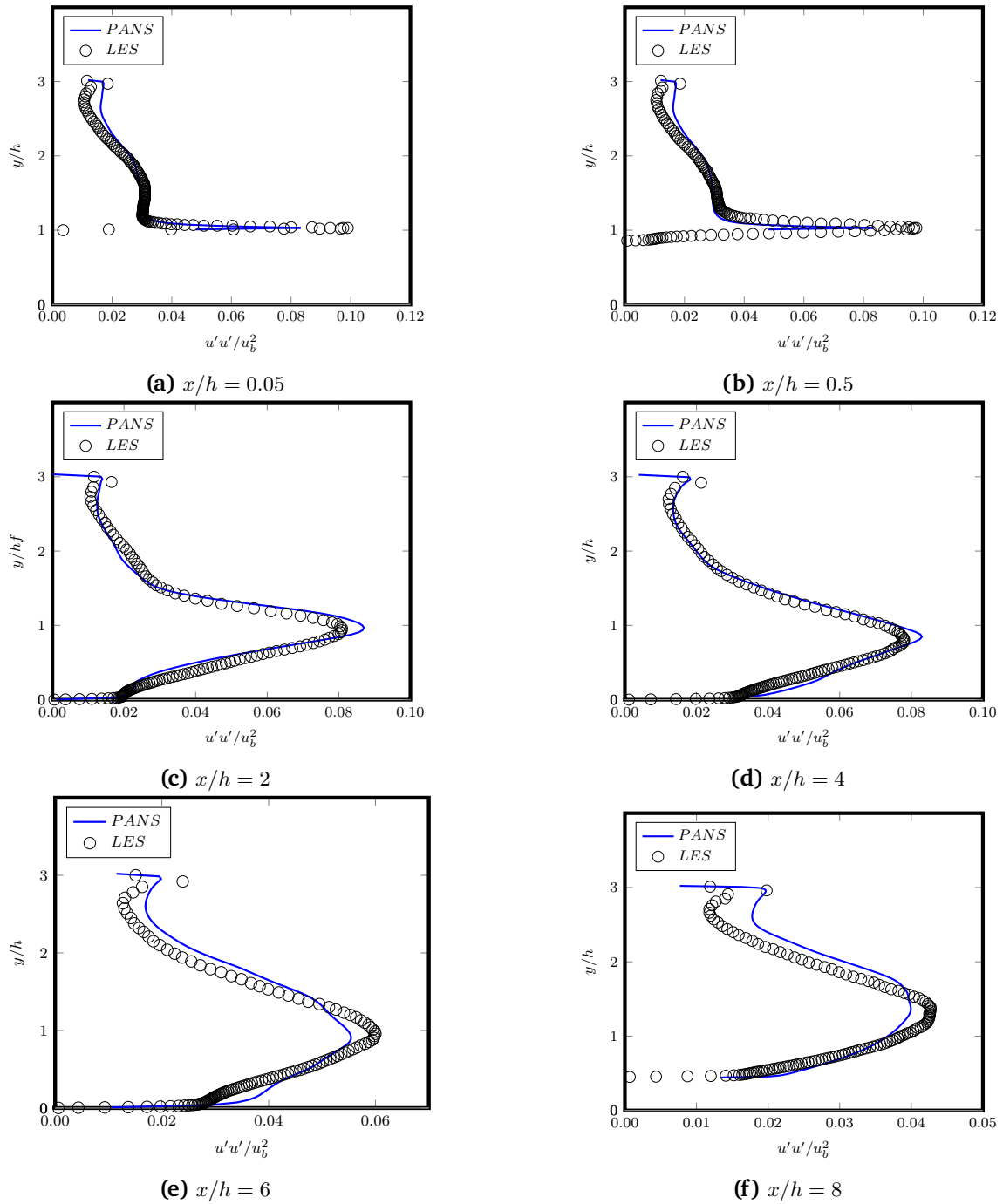
Figure 5.19 Normalized Reynolds stress profiles of $\overline{u'u'}/u_b^2$ in comparison with LES [94].

(a) $x/h = 0.05$

(b) $x/h = 0.5$

(c) $x/h = 2$

(d) $x/h = 4$

(e) $x/h = 6$

(f) $x/h = 8$
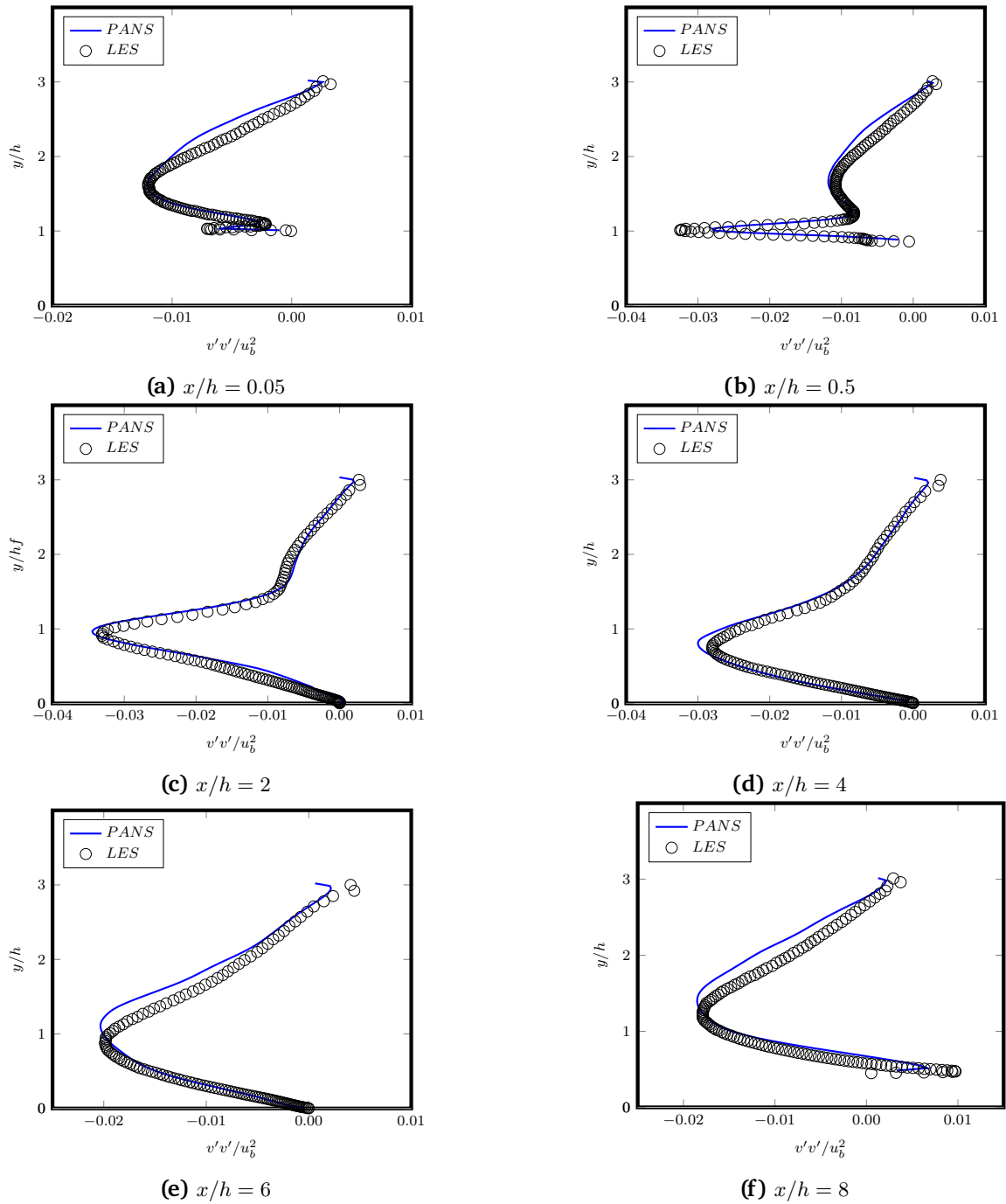
Figure 5.20 Normalized Reynolds stress profiles of $\overline{u'v'}/u_b^2$ in comparison with LES [94].

6 Aeroacoustic Results of PANS Method

This chapter presents a comprehensive examination of the aeroacoustic performance of the SSV-PANS method and LES, with a primary focus on their applications in two distinct test cases. The first test case involves an in-depth analysis of acoustic phenomena arising from turbulent flow around a circular cylinder, with particular attention to the sound radiation resulting from vortex shedding. The second test case explores the applicability of the SSV-PANS method in aeroacoustics, especially in the context of the Ahmed body, a renowned benchmark in fluid dynamics. Together, these analyses contribute to a deeper understanding of the capabilities and performance of the SSV-PANS method in the field of aeroacoustics.

6.1 Flow Past a Circular Cylinder

This study aims to compare the aeroacoustic performance of two turbulence models, the Partially-Averaged Navier-Stokes (SSV-PANS) method and Large Eddy Simulation (LES). The investigation focuses on analyzing the generation of acoustic quantities caused by turbulent flow around a circular cylinder. The specific aspect of interest is the sound radiation resulting from vortex shedding behind the cylinder. The simulations consider a Reynolds number of $\mathrm{Re} = 48,000$ and a Mach number of $\mathrm{Ma} = 0.21$ ($C_\infty = 343$ m/s) based on the cylinder diameter ($D = 0.01$ m).

To accurately capture the intricate flow dynamics, a circular computational domain is employed with a radius of 60 times the cylinder diameter ($60D$) and a span-wise length of πD. The grid is carefully designed to have a high resolution near the cylinder's surface and in the wake region to ensure a $y^+ \approx 1$, which promotes accurate turbulence modeling. Three O-type grids are utilized for the simulations, containing approximately 2.21, 4.42, and 9.55 million control volumes (CVs), respectively. The reference LES results are obtained using 17.7 million CVs with the same test setup as the one employed in the work by Kolb et al. [45]. For visual reference, the computational domain and the grid configuration are illustrated in Figure 6.1.

The simulations are conducted with specific boundary conditions. At the inlet, a constant inflow velocity of $U_0 = 72$ m/s is specified. The outlet is set with a constant pressure condition. On the surface of the cylinder, a no-slip condition is applied, ensuring that the fluid velocity is zero at the cylinder's boundary. In the spanwise direction, a periodic boundary condition
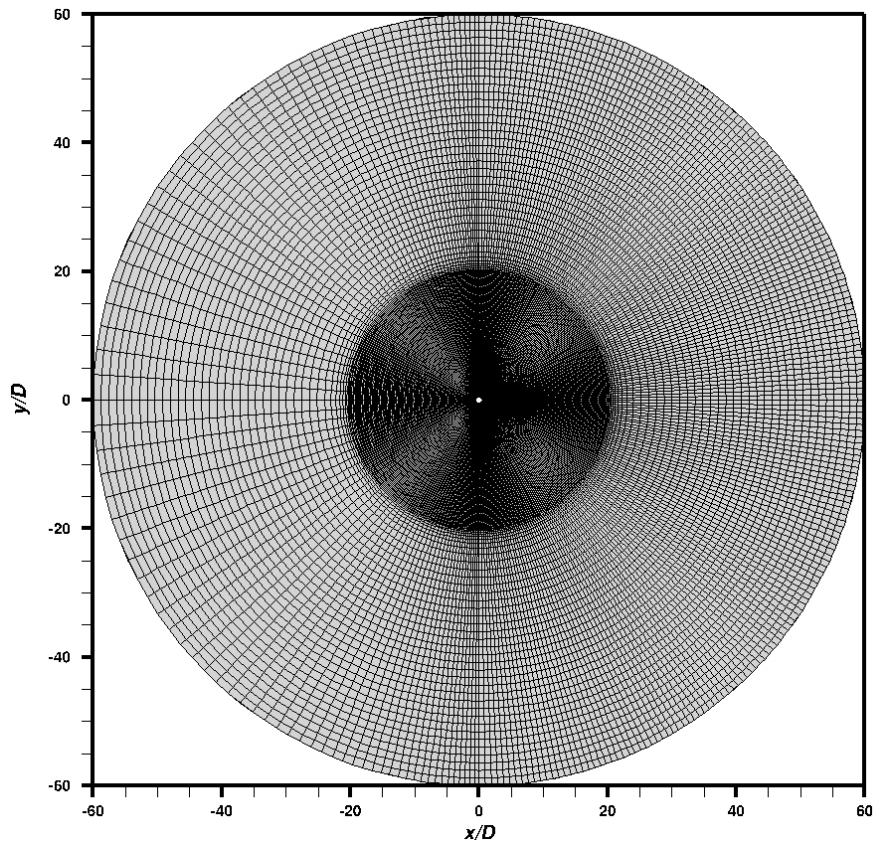
Figure 6.1 The cylinder's computational domain discretization (every 2 lines are shown).

is employed, assuming that the flow pattern repeats itself. A summary of these boundary conditions can be found in Table 6.1.

Table 6.1 Boundary conditions for the cylinder simulation.

Boundary	Inlet	Outlet	Sides	Body
Condition	Inlet Velocity	Pressure	Periodic	No-slip

To ensure numerical stability and accuracy, the fluid dynamic CFL (Courant-Friedrichs-Lewy) number is maintained at approximately 1.0. A Second-Order Fully Implicit time discretization scheme is utilized. The convective fluxes are approximated using the flux-blending scheme with β being 0.8.

To reduce computational costs, the acoustic field is computed in the mid-span plane of the grid as a two-dimensional problem, known as Long-Span Bodies method explained in subsection 4.2.3 . This approach assumes a frozen fluid, where flow variables are assumed to remain constant in time during acoustic computations explained in subsection 4.2.2. This

simplification significantly reduces computational effort while accurately capturing essential acoustic characteristics.

The aeroacoustic setup utilizes the combined splitting/Kirchhoff method to investigate the flow characteristics across the cylinder, considering a single observer in the far-field. This configuration is aligned with the acoustic measurements conducted by Jacob et al. [95], which serve as a recognized benchmark for evaluating noise prediction techniques. To enable a comprehensive comparison between the SSV-PANS method and LES, the same test setup as the one employed in the LES results by Kolb et al. [45] is adopted.

The sound generated by the flow across a cylinder is an important aeroacoustic phenomenon that arises due to the complex fluid dynamics involved. The behavior of the flow can be classified into distinct regimes characterized by different Reynolds numbers, offering valuable insights into the evolving flow patterns.

At low Reynolds numbers, the flow remains stable, and there is steady flow separation. As the Reynolds number increases, disturbances propagate, leading to the formation of well-defined vortices with laminar cores trailing behind the cylinder. This transitional regime exhibits intriguing flow dynamics. With further increases in Reynolds number, the flow enters the subcritical regime, where turbulent vortex cores become prominent, causing a transformation in the separated shear layer. The interaction between turbulent boundary layers and the cylinder's surface gives rise to an irregular vortex structure. This captivating phenomenon highlights the complex interplay between the flow and the cylinder, resulting also in distinctive acoustic characteristics.

An essential parameter for characterizing the flow oscillations is the Strouhal number (St). It quantifies the relationship between the shedding frequency (f_s), which represents the periodic detachment of vortices from the cylinder surface, and the inflow velocity (v_∞), normalized by the cylinder diameter (D). The Strouhal number serves as a dimensionless frequency that captures the dynamic behavior of the flow and its acoustic characteristics and is defined as:

$$St = \frac{C_\infty}{f_s D}.$$
(6.1)

The shedding of vortices behind the cylinder induces oscillating forces on its surface, which in turn contribute to the generation of sound. At the shedding frequency (f_s), an oscillating lift force is produced, while a drag force oscillates at twice the shedding frequency ($2f_s$). These alternating forces, combined with the turbulence in the wake region, result in the emission of broadband sound. The sound produced exhibits a rich soundscape, characterized by distinct frequencies and unique acoustic characteristics, providing valuable insights into the aeroacoustic nature of flow-cylinder interactions [96].

To ensure the accuracy of the data and minimize potential inaccuracies caused by boundary conditions beyond a certain radius, the computation of the acoustic source is limited to a radius

of $39D$. This approach helps reduce the influence of boundary conditions, leading to more reliable and accurate results. After an initial quasi-periodic stage, the flow field and acoustic field are evaluated over a duration of 30 vortex shedding cycles. This extended evaluation period allows for capturing the unsteady behavior of the flow, ensuring a comprehensive analysis of the aerodynamic and acoustic characteristics.

Table 6.2 provides a comprehensive comparison of various aerodynamic quantities obtained for the flow around a cylinder, aiming to validate the accuracy of the obtained results. The validation process involves comparing the results obtained using the SSV-PANS approach with reference data from previous studies. To ensure the credibility of the SSV-PANS results, they are compared with reference data obtained from different sources. The comparison includes data from Seo and Moon's LES study [36] conducted at a Reynolds number of Re $= 46,000$. Furthermore, data from Kolb's work [86] and experimental measurements conducted by Jacob et al. [95] at a Reynolds number of Re $= 48,000$ are used for validation. Additionally, data from Szepessy and Bearman [97] at a Reynolds number of Re $= 43,000$ is employed for further verification.

Table 6.2 Hydrodynamic quantities of flow past a cylinder compared to reference data.

		PANS	PANS	PANS	LES[45]	LES[36]	DNS[97]	Experiment[95]
CVs (million)		2.21	4.42	9.55	17.69	-	-	-
Strouhal number	**St**	0.18	0.19	0.19	0.19	0.19	0.19	0.19
Mean drag coefficient	$\bar{c}_d$	1.31	1.40	1.39	1.33	1.24	-	-
r.m.s drag coefficient	c_l'	0.11	0.12	0.14	0.06	0.10	0.11-0.18	0.08-0.09
r.m.s lift coefficient	c_d'	0.65	0.78	0.74	0.88	0.54	0.44-0.79	0.75-0.85

Table 6.2 summarizes the comparison, presenting various hydrodynamic quantities. These quantities include the number of control volumes (CVs), the Strouhal number (St), the mean drag coefficient ($\bar{c}_d$), the root-mean-square (r.m.s) drag coefficient (c_l'), and the r.m.s lift coefficient (c_d'). The comparison between the SSV-PANS results and the reference data reveals a good agreement in terms of mean quantities, such as the Strouhal number and mean drag coefficient. The Strouhal number consistently falls within the range of 0.18-0.19 for all simulation cases, which is also consistent with the reference data. Similarly, the mean drag coefficient shows a close agreement between the SSV-PANS results and the reference data.

It is important to consider that the fluctuating drag and lift coefficients exhibit significant variations depending on the experimental setup. The SSV-PANS results fall within the range of experimental uncertainties, indicating that the fluctuations observed in the simulations are

consistent with the nature of the flow-cylinder interactions. This suggests that the SSV-PANS approach captures the inherent fluctuations in the flow and accurately represents the turbulent characteristics.

Figure 6.2 provides a dynamic representation of the lift and drag coefficients over time, offering valuable insights into the aerodynamic behavior of flow around a circular cylinder. These coefficients oscillate with distinct Strouhal numbers, reflecting the periodic detachment of vortices from the cylinder's surface, a characteristic of flow-cylinder interactions. The consistency of the Strouhal numbers across different simulations underscores the reliability and robustness of the numerical approach. The significant impact of grid resolution is evident, with finer grids yielding more detailed and refined oscillations, emphasizing the importance of accurate numerical grids in capturing the nuances of aerodynamic forces. Moreover, these time variations are crucial for understanding the generation of aerodynamic noise, as lift and drag fluctuations lead to the emission of broadband sound in the wake of the cylinder.

The pressure coefficient (C_p) is a crucial parameter used to assess the aerodynamic characteristics of flow around a cylinder. In this study, an analysis was conducted using different grid configurations, including a coarse grid, a medium grid, and a fine grid, to evaluate the C_p values. These values were then compared with reference data from Seo et al.'s LES results [36] and experimental data from Szepessy and Bearman [97]. The results, depicted in Figure 6.3, demonstrate a good agreement between our obtained C_p values and the reference data.

Interestingly, it was observed that the coarse grid outperformed the medium and fine grids, particularly at an angle of 180 degrees. The inconsistency in the accuracy of the pressure coefficient between the grids can be attributed to the specific flow features and physical phenomena present in the high Reynolds number flow around a cylinder, with the coarse grid's larger cell size acting as a natural filter, effectively smoothing out fine-scale noise and capturing large-scale features like shock waves and vortices. However, for the study of aerodynamic noise, which relies on precise representation of small pressure fluctuations, finer grids are generally preferred. Therefore, while the coarse grid showed better performance at the angle of 180 degrees, the use of a fine grid is recommended for detailed aerodynamic noise analysis, with further accuracy analyses being vital to balance resolution and computational cost effectively.

The velocity contours shown in Figure 6.4 provide valuable insights into the flow characteristics around the cylinder, specifically when considering different numbers of control volumes (CVs). Increasing the number of CVs from 2.21 million to 4.42 million and further to 9.55 million leads to a progressive refinement and a more accurate representation of the flow behavior.

In Figure 6.4a, corresponding to the lowest number of CVs, the contours display a relatively coarse representation of the flow. The smoother profiles and less pronounced gradients indicate limited resolution. However, despite these limitations, it is still possible to discern the primary flow pattern and the formation of the wake region behind the cylinder. This suggests that even with a lower number of CVs, the major flow features can still be captured to some extent.

(a) 2.21 million CVs

(b) 4.42 million CVs
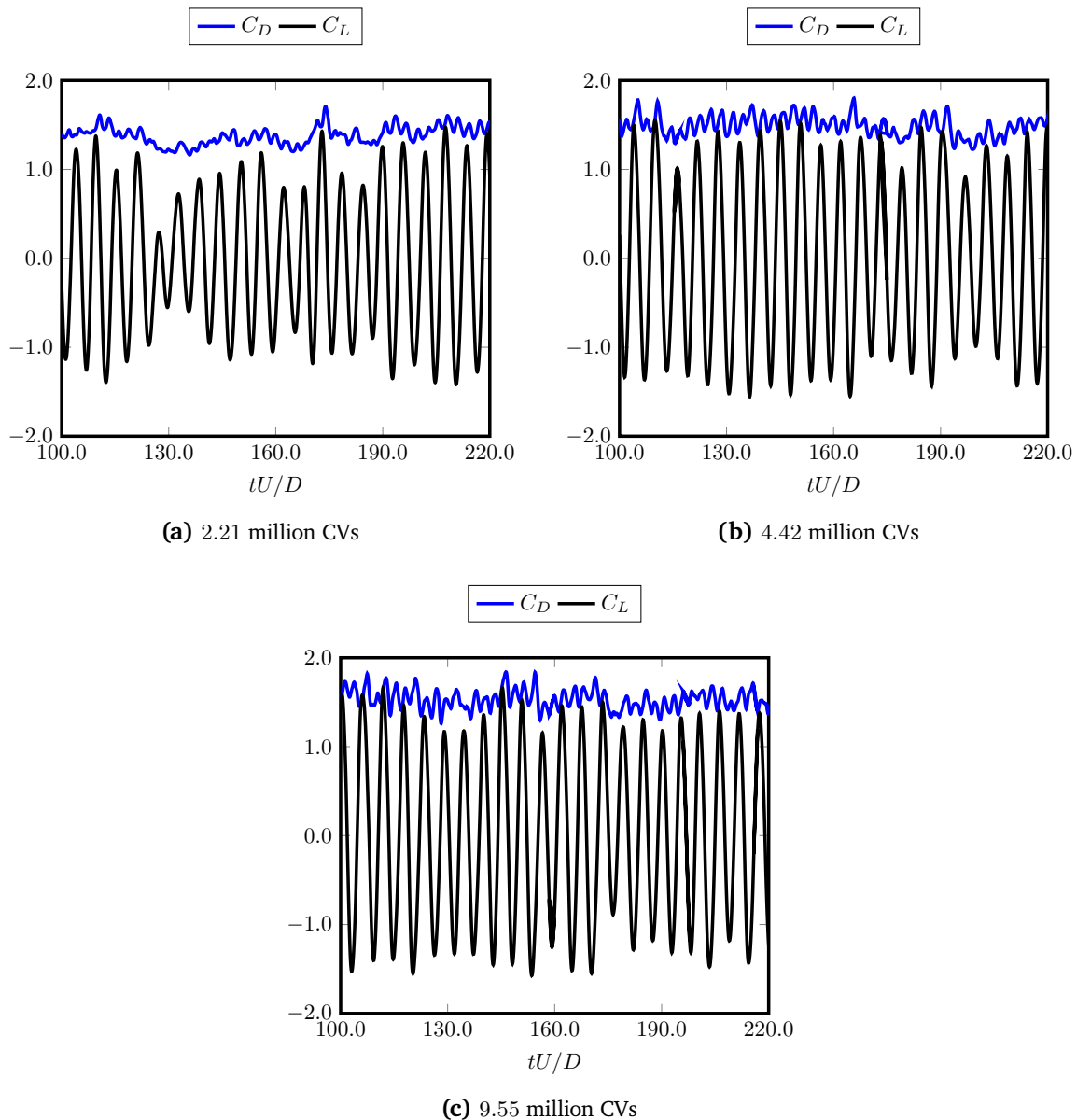
(c) 9.55 million CVs

Figure 6.2 Cylinder's time variation of lift and drag coefficients obtained by SSV-PANS different Cvs.

Moving on to Figure 6.4b, where 4.42 million CVs are employed, a significant improvement in visualizing the flow structure becomes apparent. The contours exhibit sharper gradients, providing a more detailed representation of the flow behavior. The wake region is better defined, showcasing distinct vortical structures formed by the shedding process. This enhancement in resolution enables a more accurate depiction of the flow physics near the cylinder, facilitating a deeper understanding of the flow phenomena.

Finally, in Figure 6.4c, the highest number of CVs at 9.55 million is utilized, resulting in the most refined and detailed representation of the flow behavior. The contours exhibit even sharper

Figure 6.3 Cylinder's pressure coefficient obtained by SSV-PANS in comparison with LES [36] and experiment [97].

and more localized gradients, capturing fine-scale flow features with increased precision. The well-defined vortical structures in the wake region indicate the shedding process with greater clarity. This level of resolution provides a c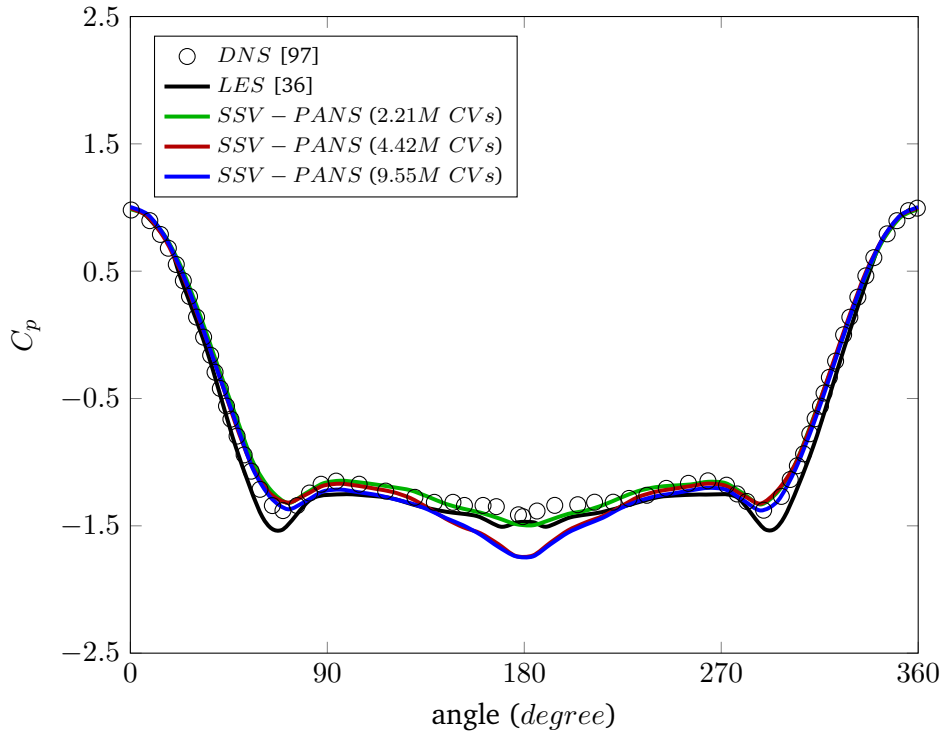omprehensive understanding of the flow dynamics around the cylinder, allowing for more accurate analysis and predictions.

The progression from lower to higher numbers of CVs highlights the significance of grid refinement in accurately capturing the flow behavior. The improved visualization of the velocity contours with increasing CVs enables a more precise characterization of the flow patterns and emphasizes the importance of grid resolution in computational simulations.

The distribution of f_k depicted in Figure 6.5, which was originally published by Moosavifard [98] and presented here, provides valuable insights into the relationship between grid resolution and the corresponding values of f_k. The figure effectively demonstrates this relationship and highlights a discernible trend. Specifically, it is evident that as the grid becomes finer, f_k values tend to decrease. The figure visually captures the impact of grid density on the behavior and characteristics of f_k, with smaller values observed for finer grids. This correlation highlights the crucial role of grid density in shaping the behavior of f_k and emphasizes the need for careful grid selection in accurate analysis and simulations.

Figure 6.6 provides a visualization of vortical structures in the wake of the cylinder using
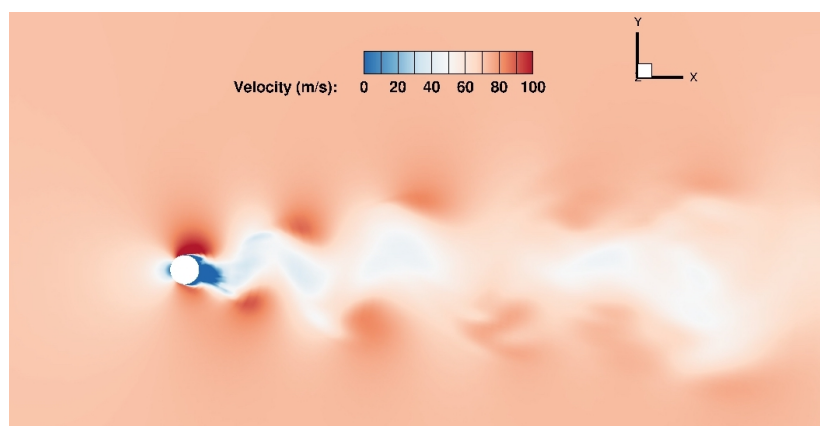
(a) 2.21 *million CVs*
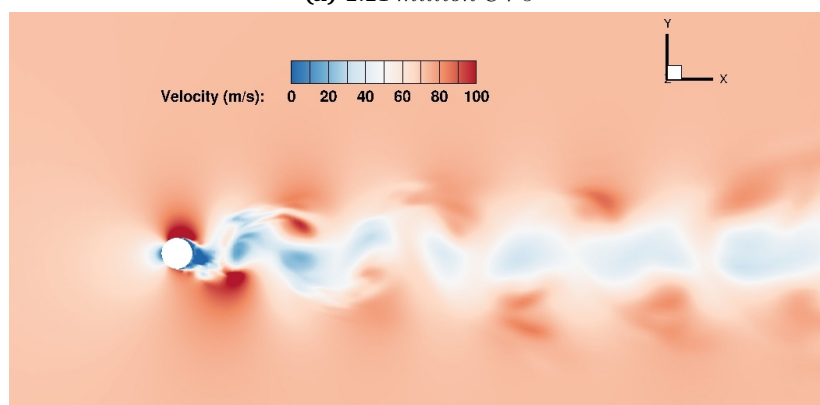
(b) 4.42 *million CVs*
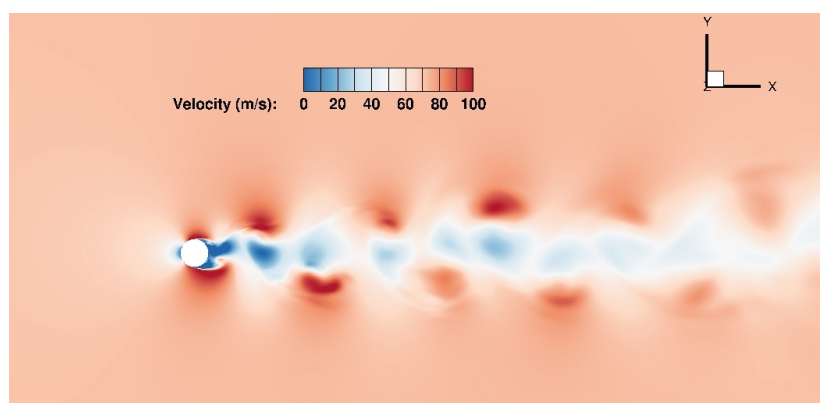
(c) 9.55 *million CVs*

Figure 6.4 Average velocity contours for different numbers of Control Volumes (CVs) obtained by SSV-PANS.

(a) $2.21\ million\ CVs$

(b) $4.42\ million\ CVs$

(c) $9.55\ million\ CVs$
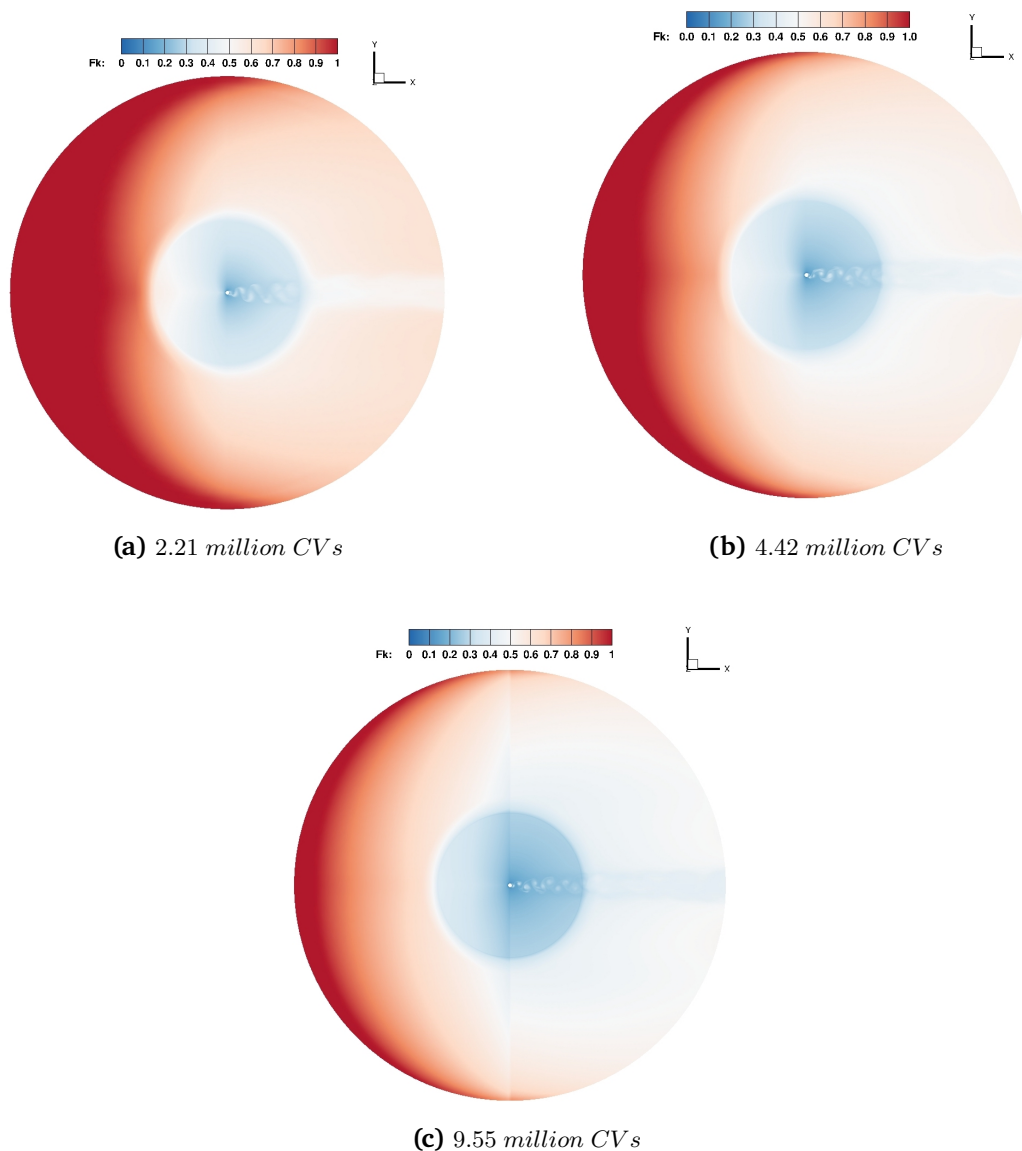
Figure 6.5 Turbulent kinetic energy resolution parameter for different numbers of Control Volumes (CVs) obtained by SSV-PANS.

the Q-criterion, which is based on the second invariant of the velocity gradient tensor. This visualization technique offers valuable insights into the complex flow dynamics, revealing the formation of large coherent vortex structures resulting from the roll-up of the shear layer. These structures contribute to momentum mixing and transport within the flow. The Q-criterion also highlights the presence of small-scale turbulent structures within the separated boundary layer, indicating the three-dimensional nature of the flow.

The subfigures in Figure 6.6, corresponding to different numbers of control volumes (CVs), allow for a comparative analysis. Increasing the number of CVs from 2.21 million to 9.55 million

results in improved resolution and detail. The vortical structures appear relatively coarse and less detailed in Figure 6.6a, while Figure 6.6b exhibits more intricate patterns with clearer boundaries. Figure 6.6c showcases the highest level of detail, revealing smaller turbulent structures within the separated boundary layer. These findings emphasize the importance of grid resolution for accurately capturing and analyzing the flow features in the wake of the cylinder.

The hydrodynamic/acoustic splitting approach is utilized in this study, as discussed in section 4.2, to accurately capture and analyze acoustic waves. This approach effectively resolves acoustic waves in the near- and mid-field regions. At the Strouhal frequency St, periodic lift fluctuations on the cylinder's surface generate dipole-like patterns in the acoustic pressure field, resulting in the emission of acoustic waves perpendicular to the flow direction of the cylinder. To visually demonstrate this phenomenon, Figure 6.7 presents a compelling visualization of the dipole characteristics exhibited by the radiated sound. These characteristics arise from the shedding of vortices at the rear of the cylinder. As the fluid flows around the cylinder, vortices form and periodically detach, creating alternating regions of high and low pressure in the surrounding medium. These pressure variations give rise to a distinct dipole pattern in the radiated sound field, characterized by discernible areas of compression and rarefaction. The presence of this dipole pattern signifies the fundamental mechanisms governing sound generation in the wake of the cylinder.

Furthermore, Figure 6.7 (consisting of Figure 6.7a, Figure 6.7b, and Figure 6.7c) showcases the influence of the number of control volumes (CVs) on the resolution and level of detail in capturing the acoustic pressure field. The sequence of images demonstrates the improvement in resolution as the number of CVs increases. In Figure 6.7a, relatively coarse dipole structures are observed, while Figure 6.7b exhibits more intricate patterns with clearer boundaries. Finally, the highest level of detail is revealed in Figure 6.7c, providing insights into smaller-scale variations within the dipole pattern.

The investigation of acoustic sources obtained from various turbulence models provides valuable insights into the process of sound generation. In this regard, Figure 6.8 depicts the acoustic source of the cylinder using the SSV-PANS model.

Figure 6.8a, utilizing 2.21 million control volumes (CVs), presents an overview of the sound generation characteristics, highlighting regions with significant acoustic activity. In this figure there are some oscillations in the sources. Moving to Figure 6.8b, with an increased number of 4.42 million CVs, a more detailed representation of the acoustic source is observed. There osciclations available in the 2.21 million CVs are not visible in this case . This allows for capturing finer details and variations in its distribution. Finally, Figure 6.8c utilizes the highest number of CVs, 9.55 million, offering a comprehensive view of the intricate features of the acoustic source with the highest level of detail.

The Kirchhoff method is utilized to determine the acoustic pressure in the far-field region.
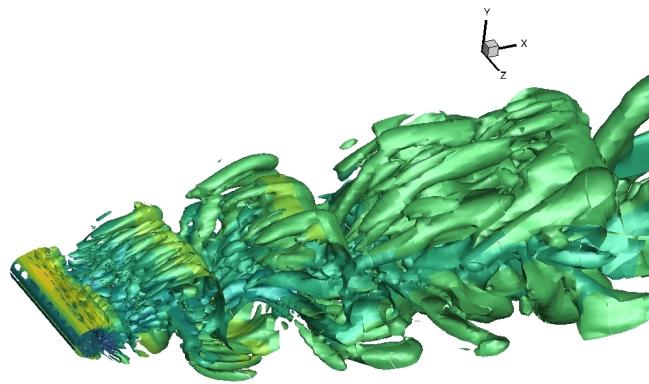
(a) $2.21 \ million \ CVs$
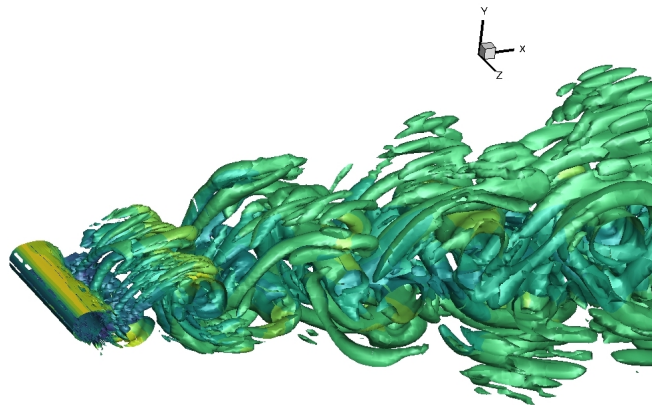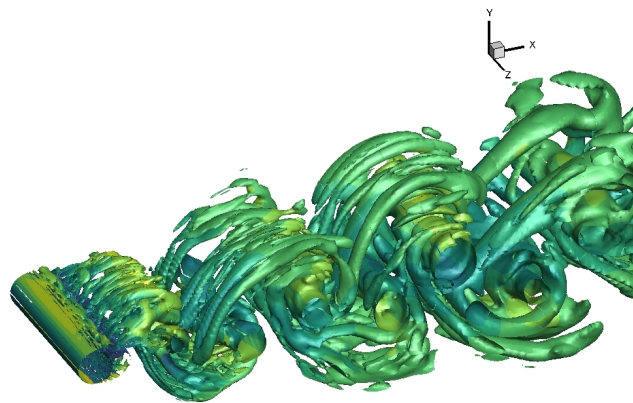
(b) $4.42 \ million \ CVs$

(c) $9.55 \ million \ CVs$

Figure 6.6 Iso-surface of the Q-criterion showing three-dimensional flow structures for different numbers of Control Volumes (CVs) obtained by SSV-PANS.

(a) $2.21 \; million \; CVs$

(b) $4.42 \; million \; CVs$

(c) $9.55 \; million \; CVs$
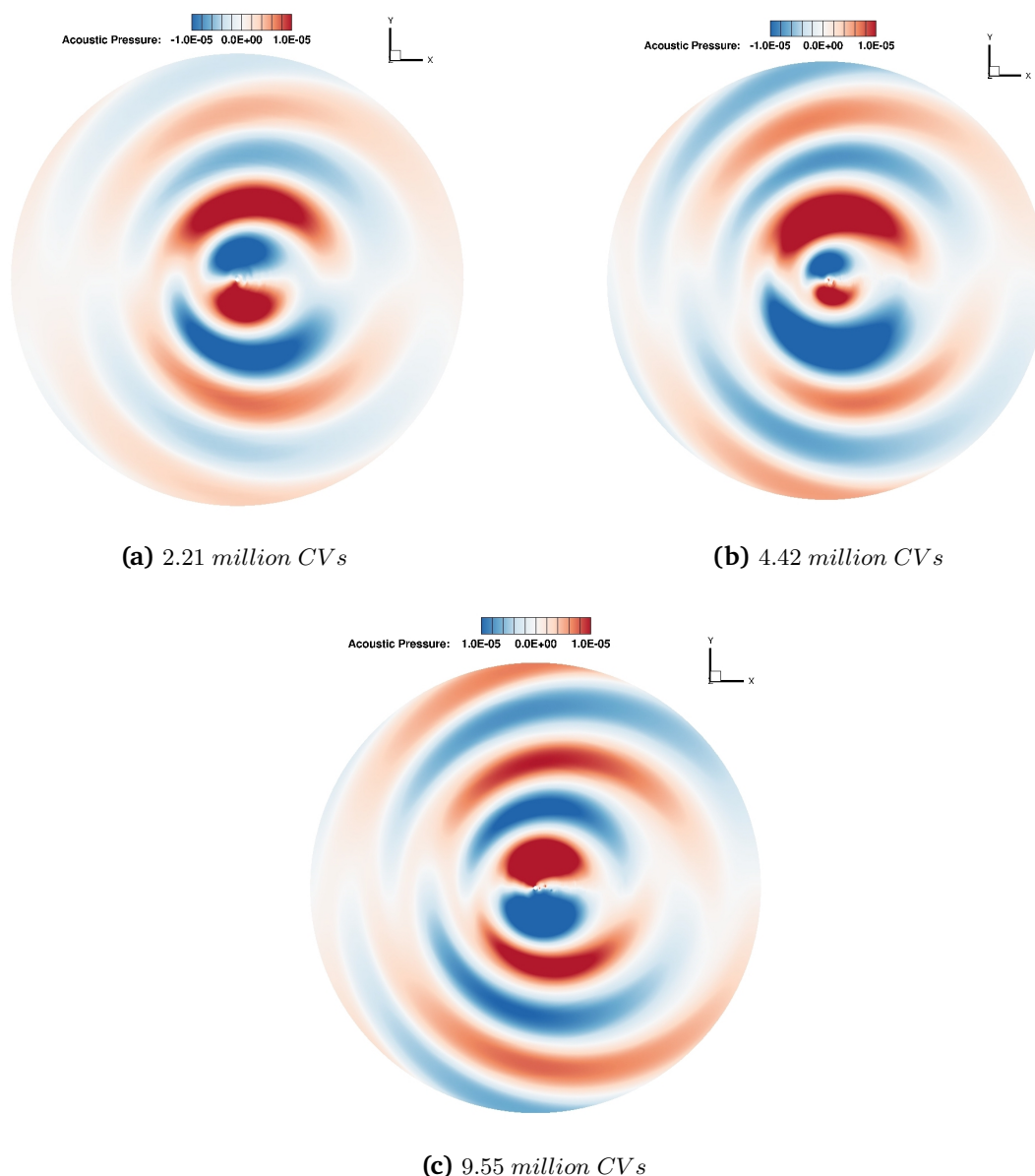
Figure 6.7 Acoustic pressure field of the cylinder. Non-dimensionalised by $\rho^{ic} c_\infty^2$.

This method has been explained in subsection 4.2.4. In the study conducted by Kolb et al. [45, 86], as well as in the experimental investigations carried out by Jacob et al. [95], an observer point located at a distance of $185D$ from the center of the cylinder, perpendicular to the flow direction, was used. At this specific position, Sound Pressure Level (SPL) data were collected and depicted in Figure 6.9 after appropriate corrections.
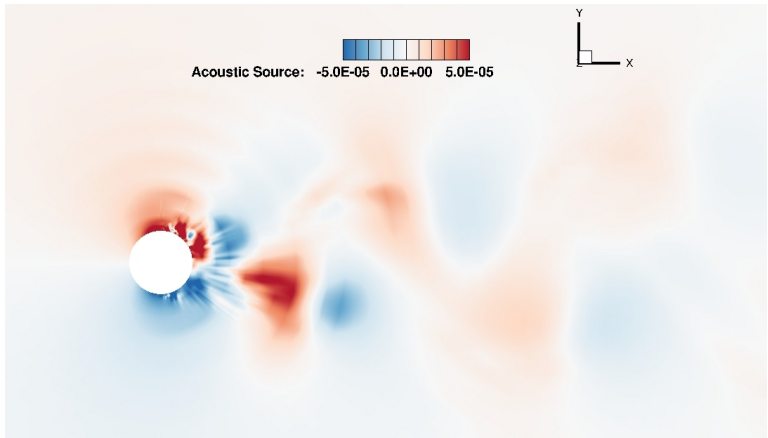
(a) $2.21\ million\ CVs$
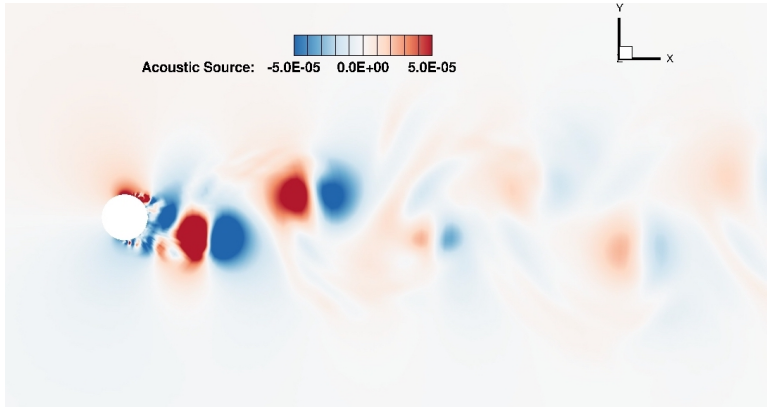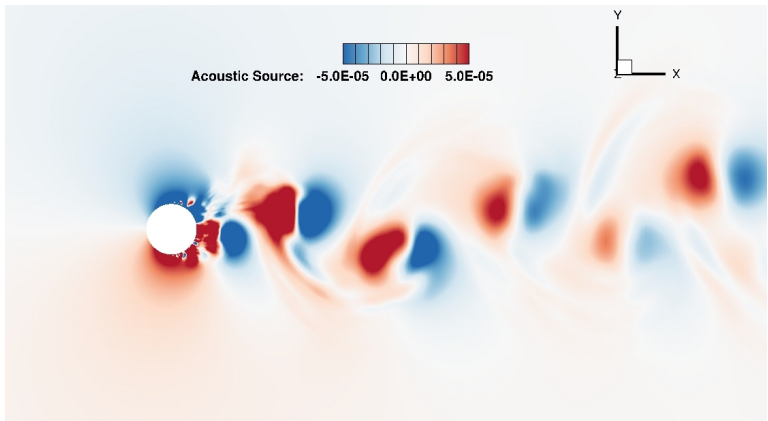
(b) $4.42\ million\ CVs$

(c) $9.55\ million\ CVs$

Figure 6.8 Acoustic source of the SSV-PANS model for the cylinder Non-dimensionalised by $\rho^{ic}c_\infty^3/D$.

To record the acoustic pressure and its spatial derivatives over a period of 30 vortex shedding cycles, the Kirchhoff surface was employed. The Kirchhoff surface had a radial extension of $40D$. Subsequently, the acquired far-field acoustic pressure was transformed from a 2D representation to a 3D representation using Equation 4.60. Furthermore, a correction was applied to account for the finite span length of $L = 30D$ using Equation 4.62. Experimental measurements by Jacob et al. indicated an acoustic coherence length of $Lc = 2.7D$ at the vortex shedding frequency [95]. For the remaining frequency range, the ratio L_c/L_s did not exceed $1/\sqrt{\pi}$. To ensure a fair comparison, the simulation closely replicated the setup described by Kolb et al. [45, 86]. For additional simulation details, it is recommended to refer to their work.

In order to validate the obtained results, the SPL of the final acoustic signal is compared with experimental reference data from Jacob et al. [95], as shown in Figure 6.9. The frequencies in the comparison are normalized with respect to the shedding frequency St. This comparison provides a means to assess the accuracy of the simulated acoustic signal in comparison to the experimental measurements. Additionally, Figure 6.9 reveals the presence of two additional harmonics that correspond to the oscillations in lift and drag. Initially, these harmonics were less noticeable, but as the grid resolution was increased, their prominence time became more evident. This finding suggests that refining the grids improves the visibility and accuracy in capturing these oscillations.

The results obtained from both the LES and experimental studies were summarized and compared in Table 6.3. Notably, there was a strong agreement between the computed results and the experimental data reported by Jacob et al. [95]. In particular, the broad peak observed at the vortex shedding frequency, as indicated in Table 6.3, was specifically compared with the LES study by Kolb et al. [45] and the experiments conducted by Jacob et al. [95].

The aeroacoustic method based on the SSV-PANS approach demonstrated a reasonable level of accuracy in predicting broadband noise, as evident from the results. These findings emphasize the effectiveness of the SSV-PANS method in aeroacoustic analysis and its potential for practical applications.

Table 6.3 Comparison of Strouhal frequency.

Model	St	Error (%)
SSV-PANS	0.182	8.5
SSV-PANS	0.184	7.5
SSV-PANS	0.189	5.0
LES[45]	0.195	2.0
Experiment[95]	0.199	-

In addition, the computational efficiency of the SSV-PANS method was evaluated by conducting a comparative analysis with the Large Eddy Simulation (LES) employing 17.7 million

(a) 2.21 million CVs

(b) 4.42 million CVs

(c) 9.55 million CVs
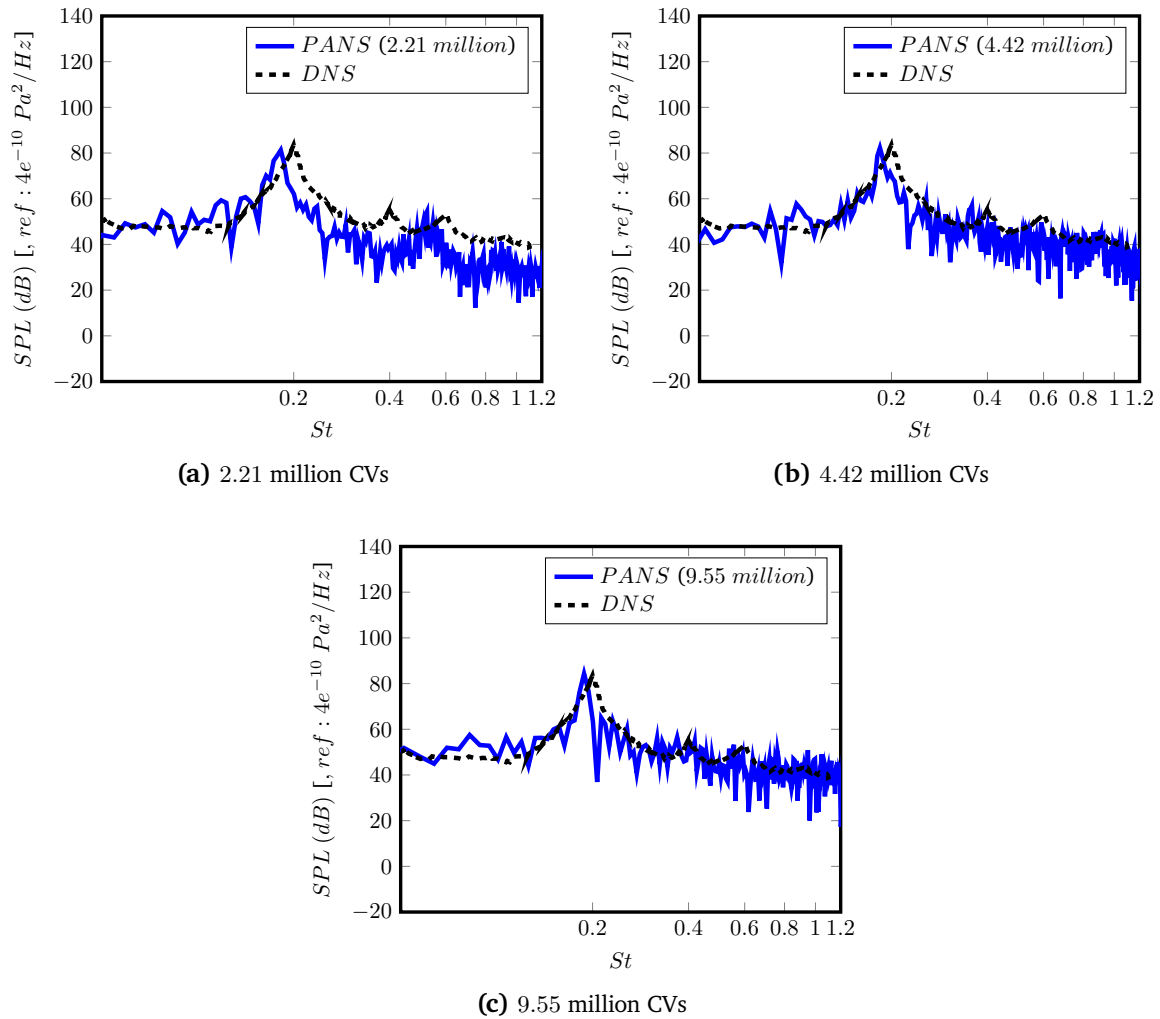
Figure 6.9 Comparison of acoustic Sound Pressure Level (SPL) at $R = 185D$ with Jacob et al. [55].

control volumes (CVs). The primary objective of this analysis was to assess the computational time required to simulate the same physical duration for all the cases. The resulting total computational time, measured in terms of "$core \times hours$", is presented in Table 6.4 for each respective test case. These comparisons have provided valuable insights into the computational advantages offered by the SSV-PANS method compared to traditional LES simulations.

The table presented provides clear evidence of the significant computational time reduction achieved through the utilization of the SSV-PANS method in simulations, while maintaining a satisfactory level of accuracy in predicting acoustic behavior. This computational advantage positions the SSV-PANS method as a highly promising approach for the analysis of complex flow-induced noise problems, enabling more efficient and practical investigations.

Figure 6.10 illustrates a distinct and non-linear increase in computational time as the number of control volumes (CVs) grows. This observation highlights an imbalanced relationship

Table 6.4 Comparison of computational time.

Model	CVs (million)	Time ($core \times hour$)	CVs ratio	Time ratio
SSV-PANS	2.21	110.8	0.13	0.07
SSV-PANS	4.42	377.5	0.25	0.25
SSV-PANS	9.55	1099.1	0.54	0.73
LES[45]	17.69	1508.8	1.00	1.00
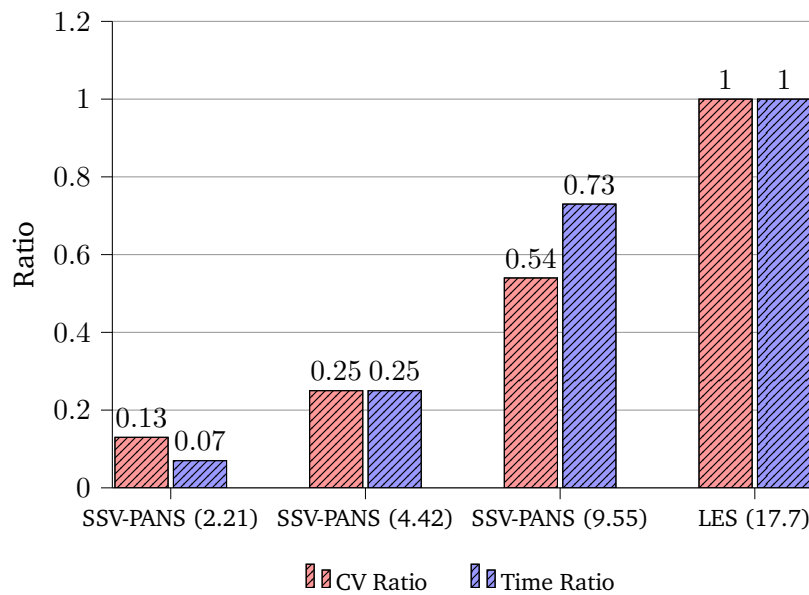
Figure 6.10 Comparison of computational ratios.

between the number of CVs and the associated computational time. Several factors contribute to this outcome.

Foremost, the incorporation of the $k - \epsilon - \zeta - f$ equation within the SSV-PANS model necessitates the solution of two additional equations, resulting in increased computational time. However, it is important to mention that the SSV-PANS model takes advantage of the SSV equation, which reduces the computational load to some extent. By utilizing the SSV equation, the model achieves better computational efficiency without compromising the accuracy of the simulations.

Additionally, the parameter f_k in the SSV-PANS model is influenced by the grid size and tends to exhibit higher values for coarser grids. This implies that coarser grids capture a greater portion of the underlying physics through modeling, rather than relying on fine-scale resolution, thereby reducing the computational time required. The use of coarser grids, with their higher f_k values, facilitates a trade-off between accuracy and computational efficiency.

The results and analysis obtained indicate that the aeroacoustic method employing the

SSV-PANS model possesses highly favorable characteristics. It effectively strikes a desirable equilibrium between computational efficiency and accuracy, establishing it as an advantageous approach for conducting aeroacoustic simulations. Consequently, the SSV-PANS method holds significant potential to enhance the computational performance of aeroacoustic simulations substantially, without compromising the reliability of the obtained results.

6.2 Flow Over an Ahmed Body

This chapter presents a comprehensive investigation into the performance of the SSV-PANS method in the field of aeroacoustics, specifically focusing on the Ahmed body—a simplified car-shaped structure. The Ahmed body, originally introduced by Ahmed [99], features a rectangular box with rounded edges at the front and a sloping face at the back, as depicted in Figure 6.11. Due to its simple yet representative design, the flow around the Ahmed body serves as an ideal test case for validating turbulence modeling methods. However, accurately modeling the airflow around this body remains challenging due to its complex flow characteristics, such as the wake region and separated flow region. As a result, the Ahmed body has been widely adopted as a benchmark case in various workshops and research programs aimed at refining flow modeling techniques. Notably, the "ERCOFTAC/IAHR Workshops on Refined Flow Modelling" held in 2001 and 2002 have extensively utilized the Ahmed body as a central focus [100–102].

To ensure the fidelity of the computational setup, the geometry of the car model was carefully examined, referring to the experiments conducted by Lienhart et al. [103]. The dimensions of the car model were designed to match those of the Ahmed body, which features a length (L) of 1044 mm, a height (H) of 288 mm, and a width (W) of 389 mm. In this study, the Ahmed Body was positioned 50 mm above the ground, as depicted in Figure 6.11. The slant angle of the car model was set to 25 degrees ($\phi = 25$), a critical parameter for the analysis. The computational domain used for the simulations consists of a fine region extending up to $8L \times 7W \times 6H$. Beyond this region, the grids are gradually coarsened. The total domain size is $57L$ in length and $29L$ in width, which is suitable for conducting aeroacoustic studies. To capture the complex flow characteristics near the surface of the Ahmed body, the grid is intricately designed with high resolution. The objective is to achieve a wall distance (y^+) of approximately 1. This low y^+ value ensures accurate modeling of turbulence, which is crucial for reliable simulation results.

Ahmed [99] emphasized that the primary source of drag on the body is pressure drag, primarily originating from the rear end. The wake structure exhibits a high level of complexity, characterized by a separation zone and counter-rotating vortices that emerge from the slanted edges. The extent of flow separation is influenced by the slant angle in a relatively intricate manner. At a critical slant angle of $\phi = 30$, the maximum drag occurs. Beyond this angle, the pressure gradient between the slant and the roof becomes so pronounced that the flow
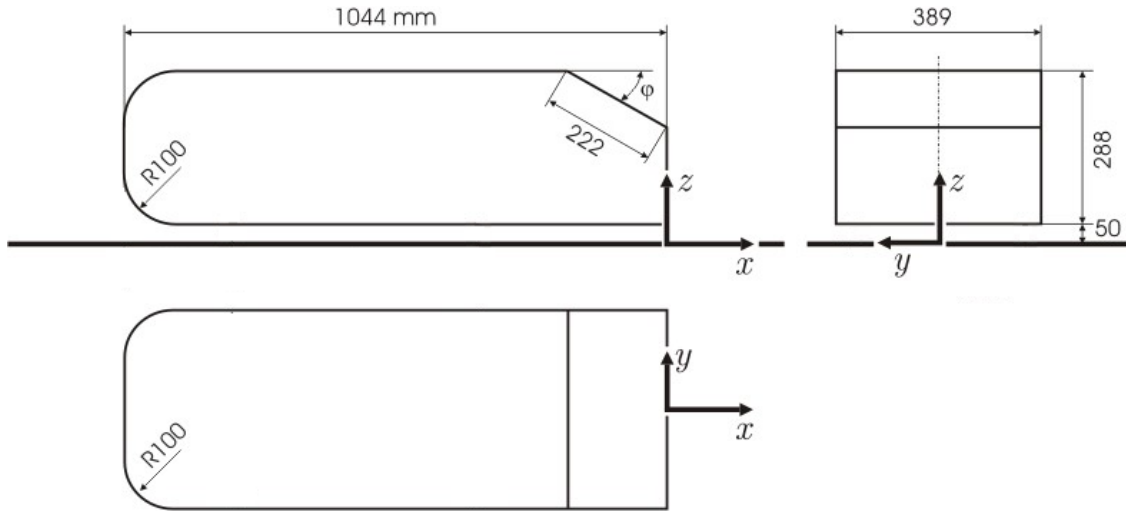
Figure 6.11 Ahmed body with slant angle $\phi = 25$, in three views with coordinate system (mm), slant angle $\phi = 25$ in current analysis.

completely detaches over the slant surface. In contrast, when the slant angle is below $\phi = 30$, the flow still undergoes separation, but the pressure differential between the slant and the side walls generates robust streamwise vortices along the lateral slant edges. These vortices induce a downward motion over the slant, primarily in the downstream region. Consequently, the wake region exhibits a complex flow pattern that varies with the slant angle, posing challenges for accurate modeling using computational fluid dynamics (CFD) simulations.

The experimental measurements were conducted with a free stream velocity of $U_0 = 40$ m/s, resulting in a Reynolds number of Re $= 768,000$ and a Mach number of Ma $= 0.12$ ($C_\infty = 343$ m/s) based on the body height H. Although this Reynolds number is of the same order of magnitude as the value of 1.2×10^6 used in Ahmed's initial experiment [99], it is slightly lower. Therefore, for comparison, the current simulations are referenced against the work of Lienhart et al. [103]. Lienhart et al. performed experiments on the Ahmed body at slant angles of $\phi = 25$ and $\phi = 35$, obtaining precise LDA measurements of mean velocity fields and turbulence statistics , which serve as a benchmark for this study.

Additionally, the results of this study are compared with the research conducted by Serre et al. [104]. Serre et al. involved four research teams using three different Large Eddy Simulation (LES) methods (LES-NWM, LES-NWR, and LES-SVV) and one Detached Eddy Simulation (DES) method (DES-SST).

The boundary conditions for the simulations are defined as follows: at the inlet, a uniform laminar velocity of U_0 is enforced, while at the outlet, a pressure boundary condition is specified. Slip surfaces are applied on both sides of the simulation domain in the spanwise direction, where the top surface is considered as slip and the Ahmed body itself is treated as a wall. A summary of the boundary conditions is presented in Table 6.5.

Table 6.5 Boundary conditions.

Boundary	Inlet	Outlet	Sides	Ground	Top	body
Condition	U_0	Pressure	Slip	No-slip	Slip	No-slip

The simulations were performed using the FASTEST software [1]. To approximate convective fluxes the Xue-MUSCL scheme is employed. For time discretization, the Second-Order Fully Implicit scheme was utilized. The coupling of pressure and velocity was achieved using the SIMPLE algorithm.

For the LES, a grid consisting of 48×10^6 control volumes (CVs) was employed. On the other hand, for the SSV-PANS method, medium and coarse grids were utilized, with CV values of 25×10^6 and 14.5×10^6, respectively. The grid structure can be visualized in Figure 6.12, and the grid surface is illustrated in Figure 6.13.
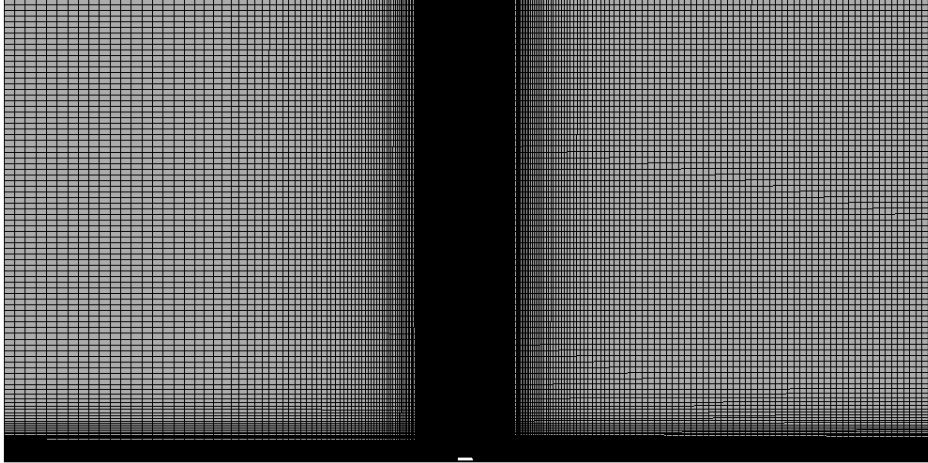
Figure 6.12 Grid structure for the Ahmed body in the simulation (every second grid line shown).

The simulations were carefully conducted to ensure that the Courant number remained below one. The computations were efficiently distributed across 240 CPUs, resulting in well-balanced workloads for all three cases.

The drag coefficient, denoted as C_D, is given by the formula:

$$C_D = \frac{2F_D}{\rho U_0^2 A_x},\tag{6.2}$$

where A_x represents the cross-sectional area of the Ahmed body aligned with the flow direction, and F_D represents the associated drag force which is time-averaged by integrating surface pressure and shear stress over the body. Table 6.6 presents a comparative analysis of the drag coefficient for the Ahmed body obtained through various simulation methods and experimental
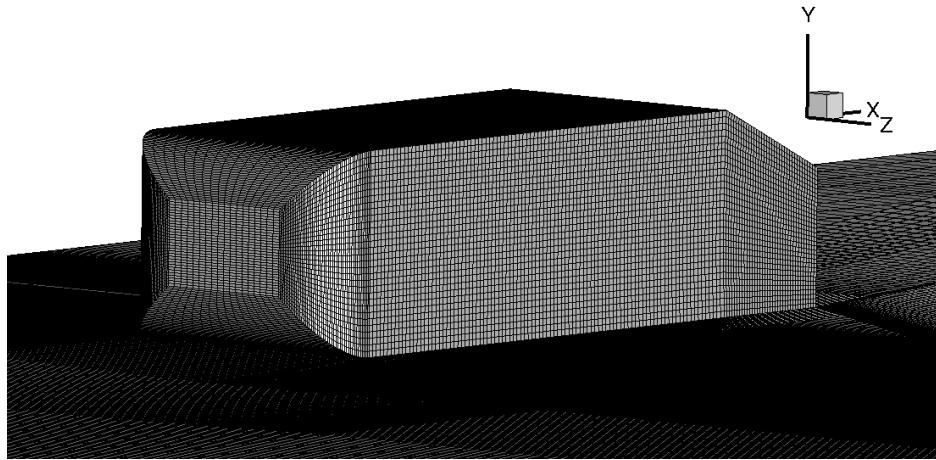
Figure 6.13 Surface mesh for the Ahmed body in the simulation (every second grid line shown).

data by Ahmed et al. [99]. The simulations include SSV-PANS with two different grid resolutions, LES, and DES utilizing the SST turbulence model. Additionally, for analysis purposes, LES-NWR, LES-NWM, and LES-SVV are included [104]. The Reynolds number used for all simulations, except for the Ahmed experiment, is Re $= 768,000$. The experiments conducted by Ahmed et al. [99] had a Reynolds number of Re $= 1.2 \times 10^6$, which were employed for comparison as corresponding data for Lienhart's experiments were unavailable [103]. It is worth noting that comparing drag results at slightly different Reynolds numbers is valid due to the insignificant variation of the drag coefficient with Reynolds number in this type of flow [104].

The computational simulations with grid resolutions of 14.5×10^6 and 25×10^6 cells exhibit similar drag coefficients. In the context of industrial applications, these simulations exhibited a tendency to slightly overestimate the drag coefficient. However, when employing LES with a more refined grid of 48×10^6 cells, the results showed better accuracy when compared to experimental data. The utilization of LES coupled with the Near-Wall Model (LES-NWM) yielded outcomes that closely aligned with the experimental measurements, displaying only a minor deviation in the calculated drag coefficient arising from flow interactions with the body under study [104]. Conversely, the LES-NWR and DES-SST approaches demonstrated the propensity to produce higher drag coefficients than those observed in the experiments. Notably, the LES-SVV method stood out as having the most significant divergence from the experimental data, as documented by Serre et al. research [104].

The ability to make accurate predictions about airflow separation and reattachment is crucial for comprehending intricate aerodynamics. Employing simulations of the Ahmed body helps to elucidate methods for modeling turbulence. according to Figure 6.14, through SSV-PANS simulations at varying grid resolutions (14.5×10^6 CVs, 25×10^6 CVs) and LES (48×10^6

Table 6.6 Drag coefficient of the Ahmed body compared to reference data.

Simulation Method	Reynolds Number (Re) $\times 10^6$	Drag Coefficient (C_d)
SSV-PANS (14.5M)	0.768	0.370
SSV-PANS (25M)	0.768	0.366
LES (48M)	0.768	0.301
DES SST [104]	0.768	0.343
LES-NWR [104]	0.768	0.346
LES-NWM [104]	0.768	0.317
LES-SVV [104]	0.768	0.431
Experiment [99]	1.2	0.298

CVs), a consistent depiction of airflow characteristics emerges, thereby enhancing our insights. Both SSV-PANS simulations accurately capture the flow structures around the Ahmed body, including coherent separation and reattachment near the rear end, matching experimental observations [103]. This indicates the successful representation of essential flow features by both SSV-PANS simulations. Additionally, the LES (48×10^6) results exhibit similar flow behavior, further supporting the agreement between SSV-PANS and LES simulations. Despite using a significantly lower grid resolution, the SSV-PANS (25×10^6) simulation achieves a comparable level of accuracy as seen in the velocity contours of the LES (48×10^6) simulation.

Figure 6.15 provides a comprehensive view of velocity profiles and vectors in the wake of the Ahmed body at varying streamwise positions (x/h) of 0, 1.12, and 1.24, illustrating the downstream evolution in the wake of the Ahmed body. The top row displays outcomes from the SSV-PANS model with 14.5 million CVs. The middle row, utilizing 25 million CVs, provides a more detailed view of velocity profile distribution. The bottom row showcases results from LES with 48 million CVs. This allows for a detailed comparison of flow dynamics and highlights the influence of grid resolution on simulation results. The figure serves as a valuable reference for assessing the accuracy of the simulations and their ability to capture intricate features in the wake region. It underscores the importance of computational grid density in achieving more faithful results and provides insights into the strengths and limitations of each approach.

The streamline visualization in Figure 6.16 provides insights into the flow behavior around the Ahmed body, particularly regarding the vortex structures at its rear. Both SSV-PANS simulations show reasonable accuracy compared to the LES simulation and the experimental data by Lienhart et al. [103]. The vortex structures observed in the SSV-PANS simulation with 25×10^6 CVs closely resemble those in the experimental data [103], indicating a good

(a) SSV-PANS (14.5×10^6 CVs)

(b) SSV-PANS (25×10^6 CVs)

(c) LES (48×10^6 CVs)
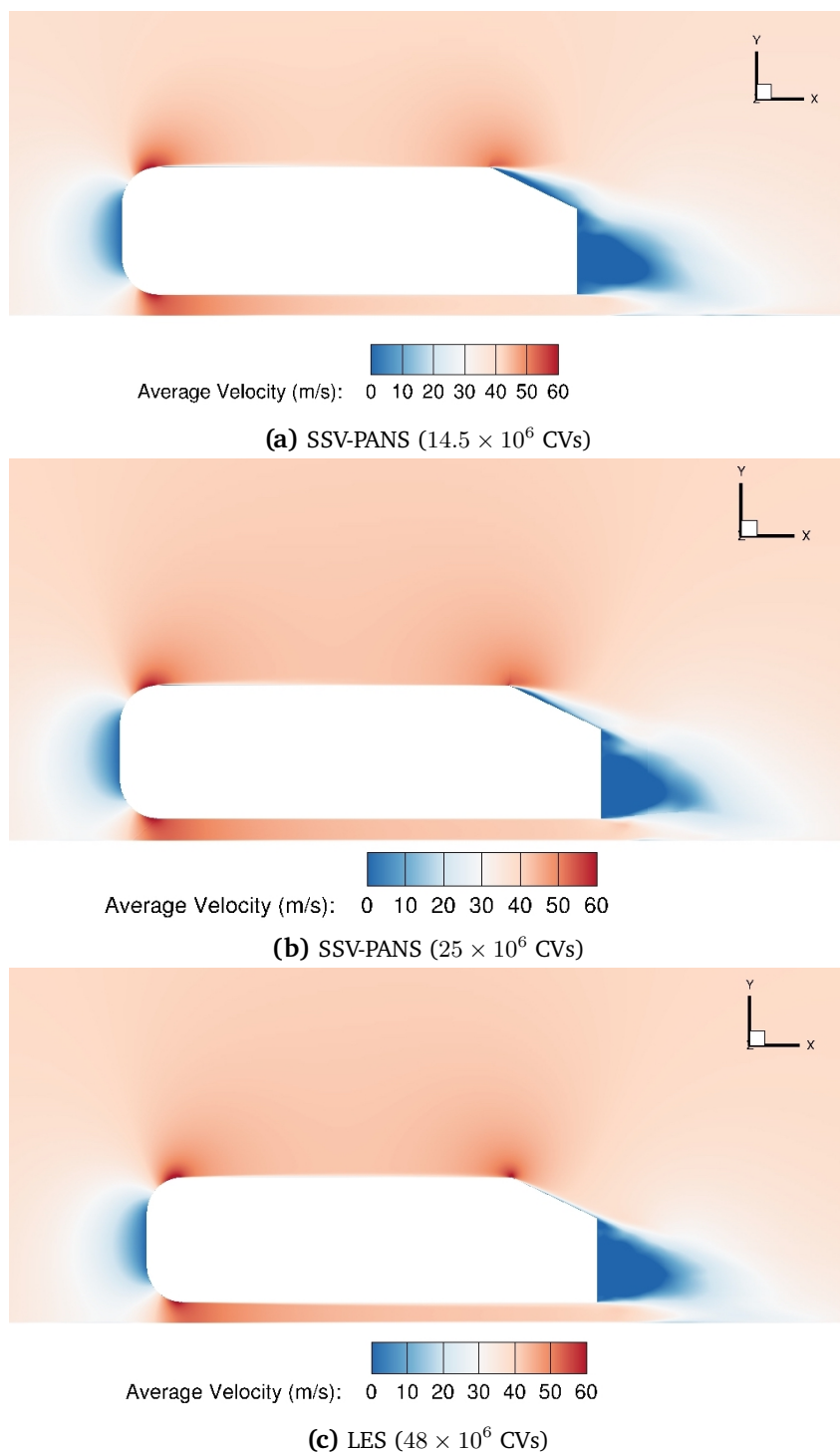
Figure 6.14 Mean velocity field around the Ahmed body for different numbers of CVs obtained by SSV-PANS and LES.

(a) $x/h = 0$ **(b)** $x/h = 1.12$ **(c)** $x/h = 1.24$

(d) $x/h = 0$ **(e)** $x/h = 1.12$ **(f)** $x/h = 1.24$

(g) $x/h = 0$ **(h)** $x/h = 1.12$ **(i)** $x/h = 1.24$
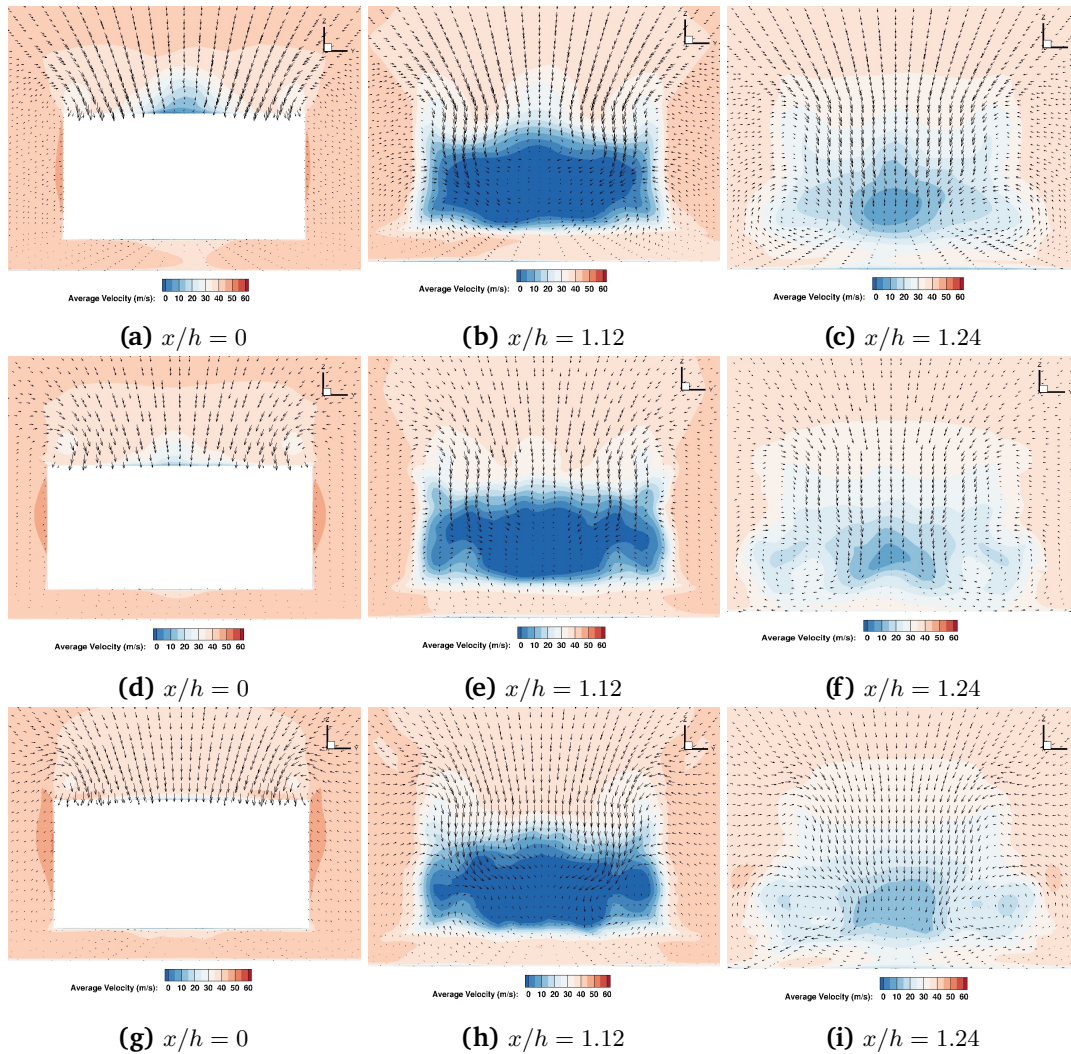
Figure 6.15 Velocity profiles and vectors in the wake of the Ahmed body. From top to bottom: results of SSV-PANS (14.5 $\times 10^6$ CVs), SSV-PANS (25 $\times 10^6$ CVs) and LES (48 $\times 10^6$ CVs).

representation of the flow behavior.

In the SSV-PANS simulation with 14.5×10^6 CVs, the upper vortex appears larger, suggesting that the coarser grid resolution affects the flow behavior. This discrepancy implies that the SSV-PANS simulation with 14.5×10^6 CVs may be less accurate in capturing the intricate flow details. The SSV-PANS simulations can be effectively compared to other simulation methods, such as DES-SST [104], LES-NWM [104], LES-NWR [104], and LES-SVV [104], in terms of their ability to reproduce vortex structures in comparison to the LES simulation and experimental observations. While the simulation outcomes generally correspond with experimental discoveries, challenges remain in achieving a precise forecast of the partial detachment of the average flow over the slant. SSV-PANS reproduces the airflow over the

Ahmed body similarly to experiments [103], whereas LES (48×10^6 CVs) encounters difficulties, same as the LES-NWR. Both simulations predict attached flow along the entire slant, without any separation or reattachment [104]. LES-SVV successfully captures the reattachment of the flow over the slant, exhibiting partial recirculation that aligns with the experimental results [104]. This suggests even with less refined grids, the SSV-PANS simulations provide a reasonable representation of the flow behavior, especially when compared to the LES simulation, and achieve comparable performance to LES-SVV in capturing the reattachment phenomenon.

In Figure 6.17, profiles of kinetic energy in the wake of the Ahmed body are presented, utilizing various turbulence modeling approaches and mesh resolutions. The top row displays results obtained with the SSV-PANS model employing 14.5 million CVs. Kinetic energy is visualized at positions (x/h) of 0, 1.24, and 1.54. The middle row features SSV-PANS with 25 million CVs, providing a more detailed view of the kinetic energy distribution. The bottom row presents results from LES using 48 million CVs. This plot illustrates the downstream evolution of kinetic energy in the wake of the Ahmed body.

The highest kinetic energy values are observed in the central section formed by the under-body flow of the vehicle and within the recirculation region behind the model. The comparison between different turbulence modeling approaches and mesh resolutions emphasizes the trade-off between computational cost and accuracy. While LES provides the most detailed representation of wake turbulence, some inaccuracies are still noticeable over the slant of the Ahmed body, underscoring the challenge of accurately predicting separation in this region. Notably, the results obtained with the SSV-PANS model using a medium grid demonstrate good agreement with experiments conducted by Lienhart [103]. The coarse grid simulation with SSV-PANS exhibits the least agreement with experiments. Therefore, this analysis reveals that accurately simulating the airflow around the Ahmed body demands a careful balance between computational resources and the intricacies of the model. Achieving a high level of precision often requires more refined grid resolutions, particularly in regions where complex flow separation occurs.

Figure 6.18 presents a comparative analysis between the SSV-PANS model and LES in terms of their effectiveness in capturing flow structures in the near-wake region. This analysis is conducted by visualizing iso-surfaces of the second invariant of the velocity gradient, denoted as Q, and color-coding them based on the streamwise average velocity. In LES, the near-wake flow structures are accurately resolved by using a fine grid resolution in the vicinity of the object being studied. Conversely, the SSV-PANS model employs a coarser grid and represents the partially-averaged velocity field. As a result, the SSV-PANS model relies more on modeling the flow scales near the near-wake region while resolving fewer of these scales compared to LES. By improving the grid resolution, additional instantaneous flow structures emerge within the wake region. Both the 14.5×10^6 and 25×10^6 SSV-PANS simulations successfully reproduce the C-pillar trailing vortices along the lateral edges. However, the 25×10^6 SSV-PANS simulation,
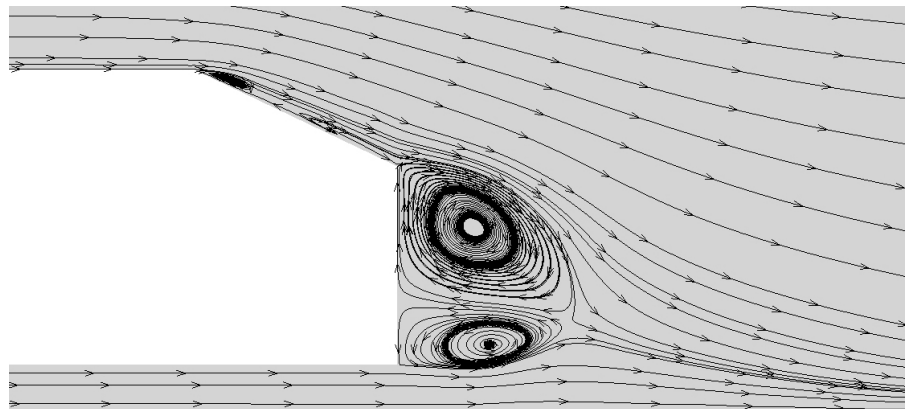
(a) SSV-PANS (14.5×10^6 CVs)
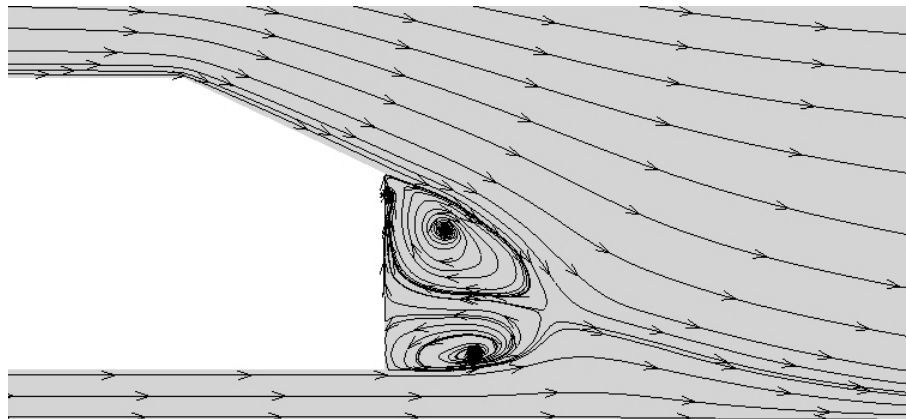
(b) SSV-PANS (25×10^6 CVs)

(c) LES (48×10^6 CVs)

Figure 6.16 Time-averaged streamlines around the Ahmed body for different numbers of CVs obtained by SSV-PANS and LES.
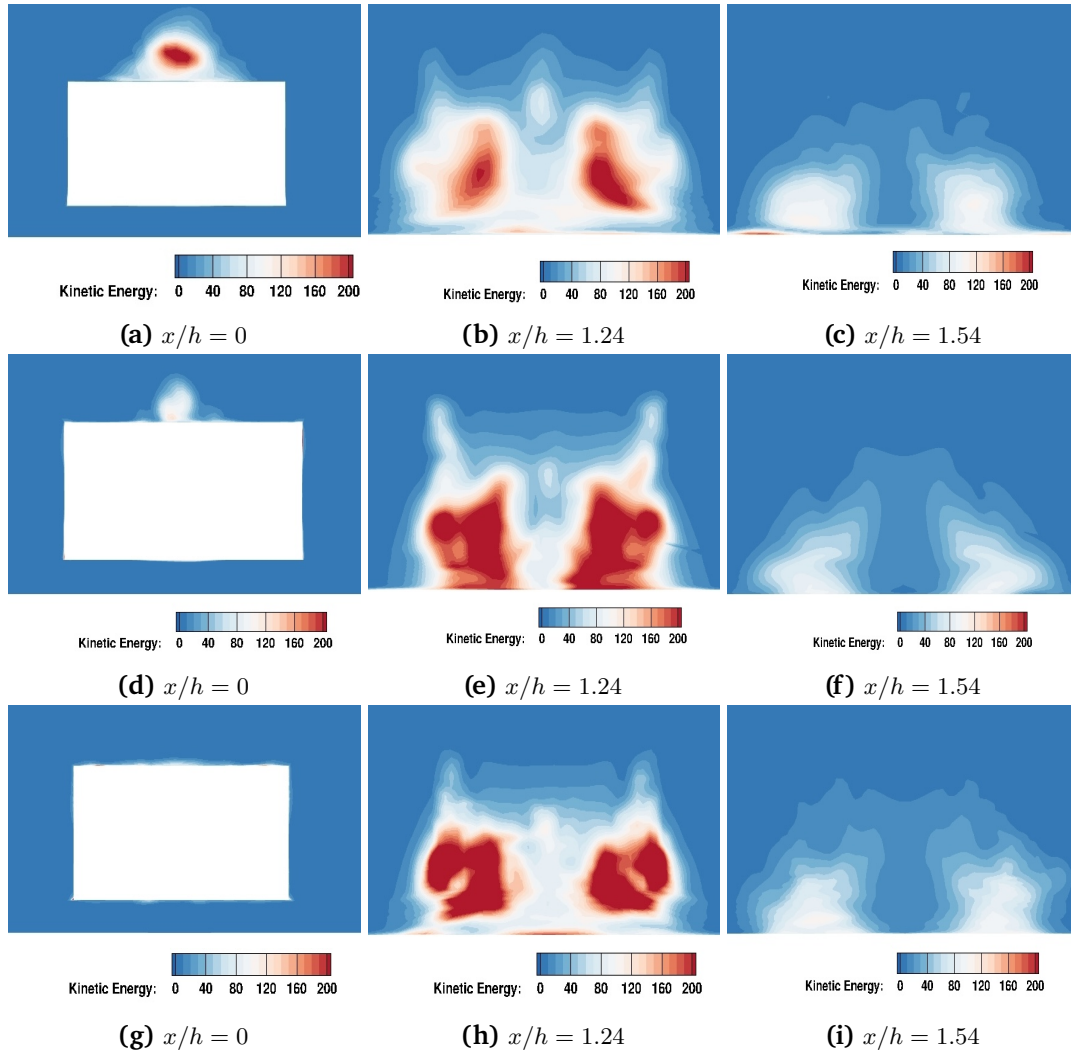
Figure 6.17 Kinetic energy in the wake of the Ahmed body. From top to bottom: results of SSV-PANS (14.5 $\times 10^6$ CVs), SSV-PANS (25 $\times 10^6$ CVs), LES (48 $\times 10^6$ CVs).
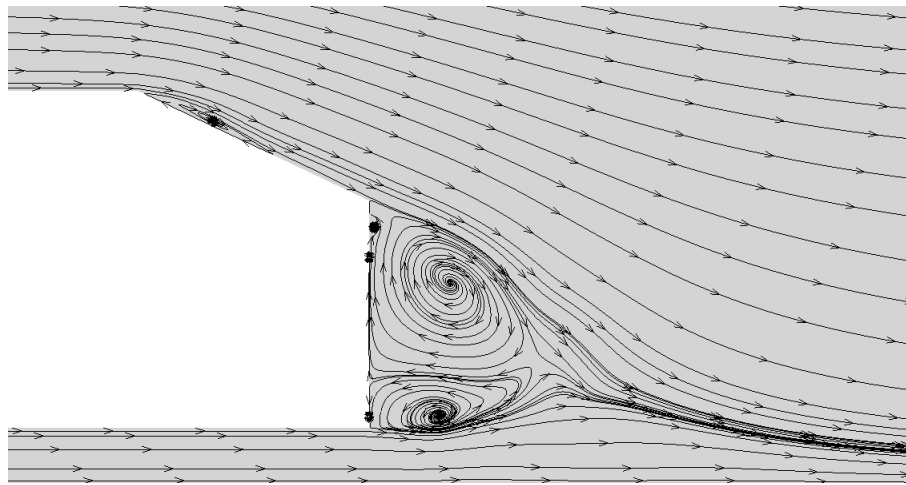
benefiting from a higher grid resolution in the wake region, captures a more comprehensive range of flow structures and demonstrates results that exhibit greater agreement with LES.

The average flow along vertical lines at different positions along the stream is compared to the reference simulations shown in Figure 6.19. Initially, the SSV-PANS method with 25×10^6 CVs is examined. Along the upper roof, the boundary layer profile exhibits less rigidity compared to the experimental observations. However, the central flow away from the object shows good agreement when compared to other approaches. Importantly, it shows good agreement with the Lienhart experiments [103] conducted under similar conditions, as well as LES-SVV [104]. The SSV-PANS method with 14.5×10^6 CVs also shows good agreement with the Lienhart experiments [103] however due the coarseness the accuracy is not as good as the

(a) SSV-PANS (14.5×10^6 CVs)

(b) SSV-PANS (25×10^6 CVs)

(c) LES (48×10^6 CVs)
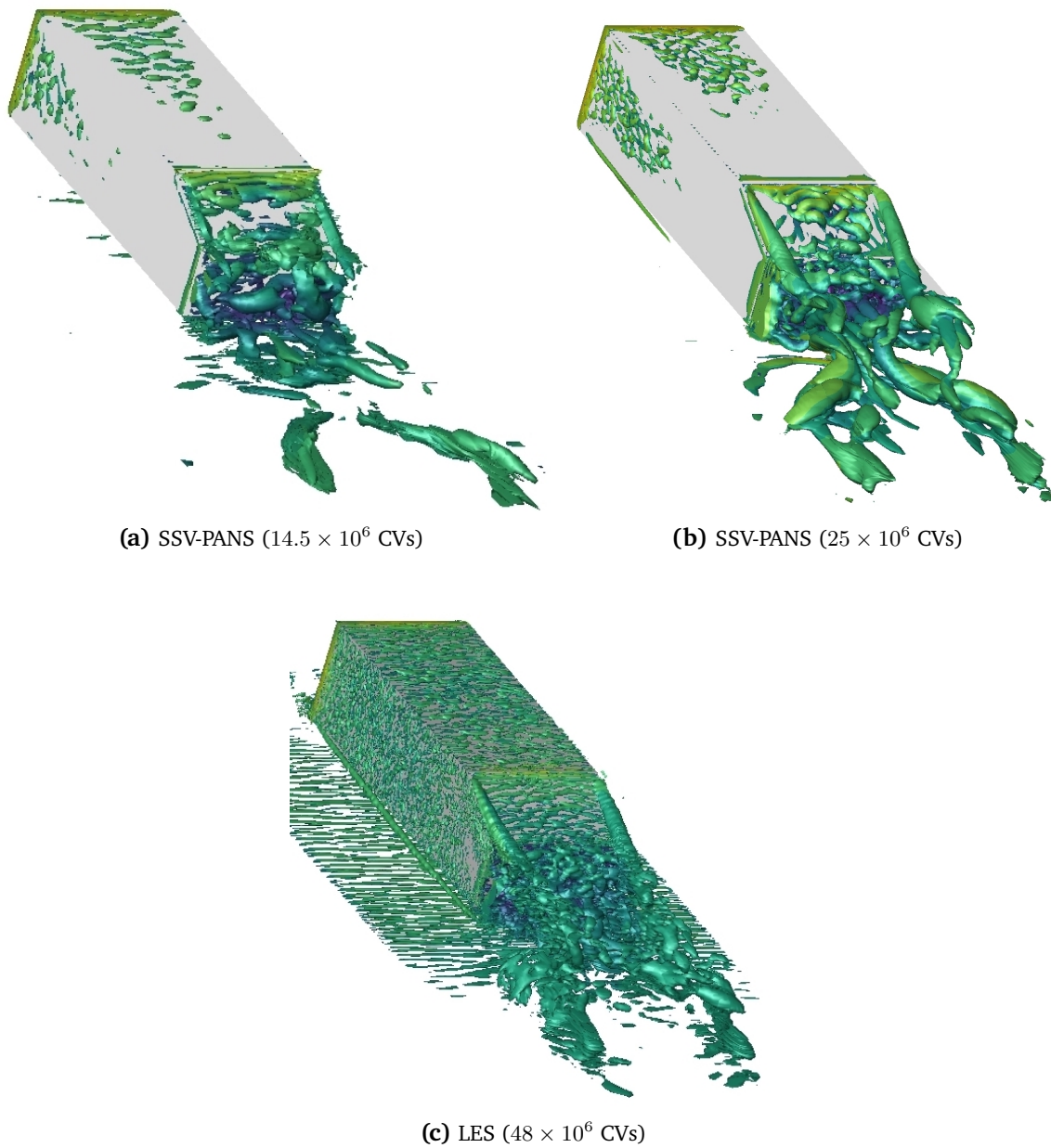
Figure 6.18 Iso-surfaces of instantaneous $Q = 100000(1/S^2))$ colored by streamwise velocity for different numbers of CVs obtained by SSV-PANS and LES.

finer resolution. Thus, the analysis reveals that the SSV-PANS method demonstrates reliable and impressive performance, even with a coarser resolution in the context of hydrodynamic results.

In the LES simulation with 48×10^6 CVs, which predicts a fully attached flow, a deviation from the reference data is observed. The fluctuations along the inclined surface are reduced, resulting in diminished magnitudes and significantly lower intensity downstream compared to

the reference data. This trend is also evident in the LES-NWR simulation [104], confirming previous findings.

The consistent accuracy demonstrated across various cross-validation resolutions underscores the robustness of the SSV-PANS method in predicting the mean streamwise velocity distribution for the intricate aerodynamics of the Ahmed body. This also highlights its performance concerning results obtained from LES.
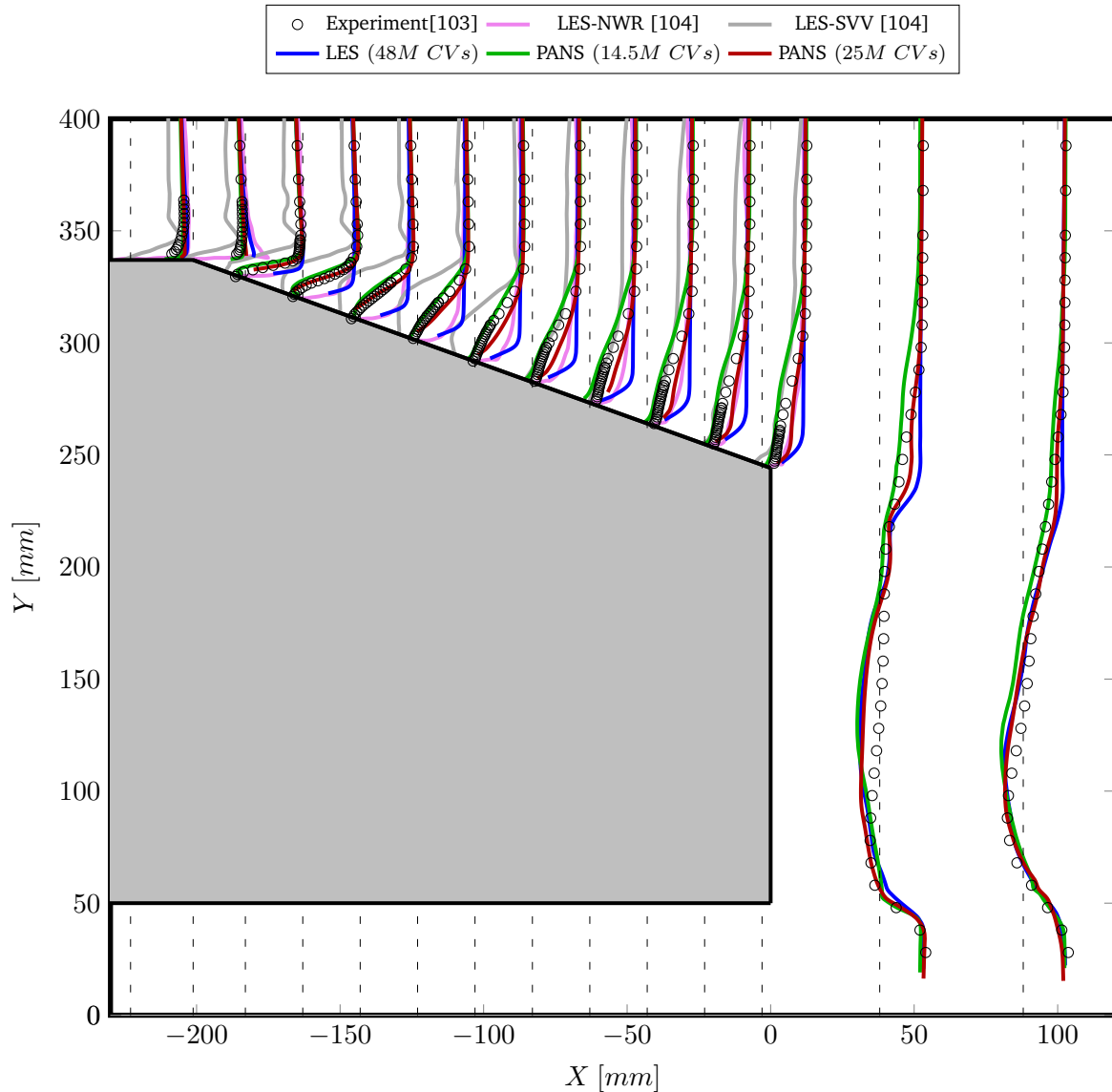
Figure 6.19 Profiles of the mean streamwise velocity over the slant of the Ahmed body for different numbers of CVs obtained by SSV-PANS in comparison with refrence data [103, 104].

The plot shown in Figure 6.20 depicts the Reynolds stresses in the flow over the Ahmed body.

The Reynolds stresses are key components of the flow's turbulence characteristics, reflecting the anisotropic nature of turbulence in the flow field. In this plot, the Reynolds stresses are presented at various locations along the body's surface, allowing a detailed comparison between experimental measurements [103] and results obtained from LES and SSV-PANS simulations. This comparison serves as a critical step in assessing the accuracy and performance of the turbulence models in predicting essential aspects of the flow behavior over the Ahmed body.

An interesting observation from the results is the behavior of turbulence over the slant within the boundary layer. Turbulent kinetic energy plays a significant role in maintaining flow attachment to the slant, aligning with what was observed in the velocity profiles of the LES simulation with 48 million CVs. The reasons behind this behavior will be discussed in the following. On the other hand, the SSV-PANS simulation with 14.5 million CVs exhibits a notable deviation from the experimental data, highlighting the limitations of this specific simulation setup. In contrast, the SSV-PANS simulation with 25 million CVs demonstrates remarkable agreement with the experimental results, indicating that a finer grid resolution significantly enhances the model's predictive capabilities, enabling a more precise capture of the flow phenomena.

Evaluating uncertainty in LES is a complex task, primarily due to the influence of grid-dependent numerical discretization and subgrid-scale modeling. Various approaches can be employed for LES assessment, and different quality indexes have been proposed, categorized based on parameters such as subgrid viscosity, Kolmogorov scale, and turbulent kinetic energy.

The LES criteria, as depicted in Figure 6.21 and Figure 6.22, are indispensable tools for evaluating the performance of LES. This is especially relevant in the context of simulating flow over the Ahmed body, where discrepancies between LES results and experimental data became evident, particularly over the slant region. These criteria provide valuable insights into the effectiveness and fidelity of LES models when compared to experimental observations.

Figure 6.21 outlines the criteria for assessing mesh resolution suitability, as proposed by Pope [51]. This method considers the ratio of the representative grid width (Δ) to the smallest vortex structures, the Kolmogorov length scales (η). Ideally, this ratio should fall within the range of $\Delta/\eta \approx 10 - 12$ or lower. In the current study, the volume grid cell is adopted as the representative grid width (Δ). This ratio serves as a critical indicator for evaluating mesh resolution suitability. The velocity profile around the rear of the Ahmed body indicates that the grid resolution used in LES modeling is situated near the upper limit of the acceptable range. Given the significant turbulence production in this region, operating at the upper end of the range may introduce potential inaccuracies. Therefore, it can be inferred that the LES results may not fully meet this criterion over the slant, suggesting a grid refinement in the area to align the simulation more closely with experimental data.

Another quality index, $LES - IQ_\eta$ [105], assesses the comparison between grid size and Kolmogorov scale, as defined in Equation (6.3):
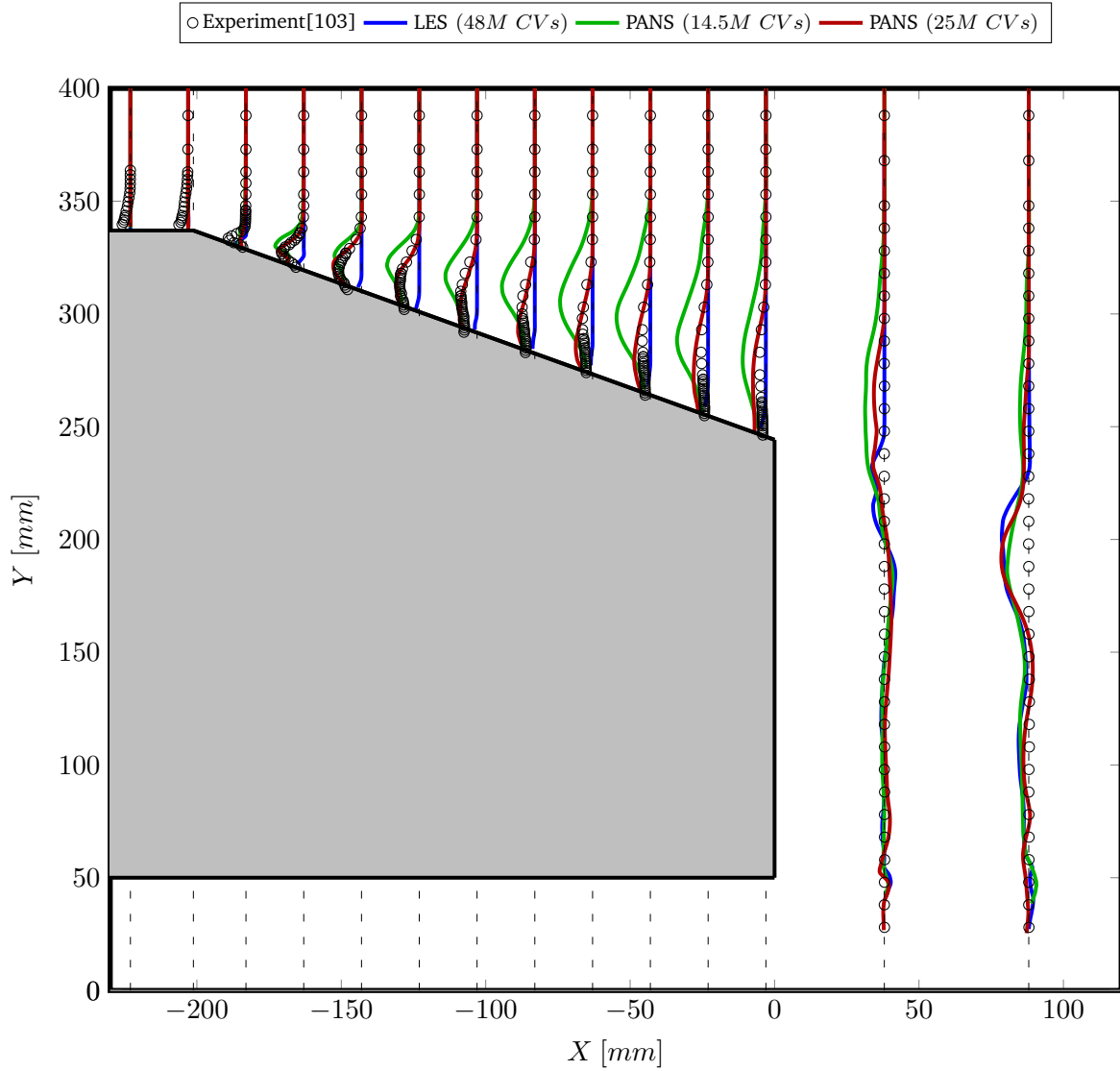
Figure 6.20 Profiles of Reynolds stress distribution ,uv (m^2/s^2), over an Ahmed body, comparing experimental data [103] with LES and SSV-PANS simulations.

$$LES - IQ_\eta = \frac{1}{1 + \alpha_\eta \left(\frac{h}{\eta_k}\right)^m}.$$ (6.3)

In this equation, h represents the grid size, and η_k is the Kolmogorov scale. Using parameters $\alpha_\eta = 0.05$ and $n = 0.5$, $LES - IQ_\eta > 0.8$ indicates a good LES. The profile illustrated in Figure 6.22 over the slant region is of particular interest. It indicates a value slightly lower than 0.8, which may warrant again further consideration for aligning with this criterion. This observation underscores the need for potential refinements to achieve a more robust congruence between

the LES results and the criteria established for mesh resolution suitability.

These LES criteria plots present a comprehensive method for evaluating the robustness of LES results. The discrepancies identified within the context of the slant flow configuration highlight the need for enhanced grid refinement in regions characterized by substantial turbulence production. This refinement aims to bring LES simulations into closer alignment with experimental data. However, it is important to note that enhancing grid refinement comes at the cost of increased computational resources, making it essential to strike a balance between accuracy and computational efficiency in LES simulations.

Despite the observed limitations in LES accuracy, its capability to effectively capture small-scale turbulence structures positions it as a valuable choice, particularly when compared to SSV-PANS. This relevance is especially pronounced in aeroacoustic studies, where the intricacies of turbulence play a pivotal role in influencing the acoustic characteristics of the flow.
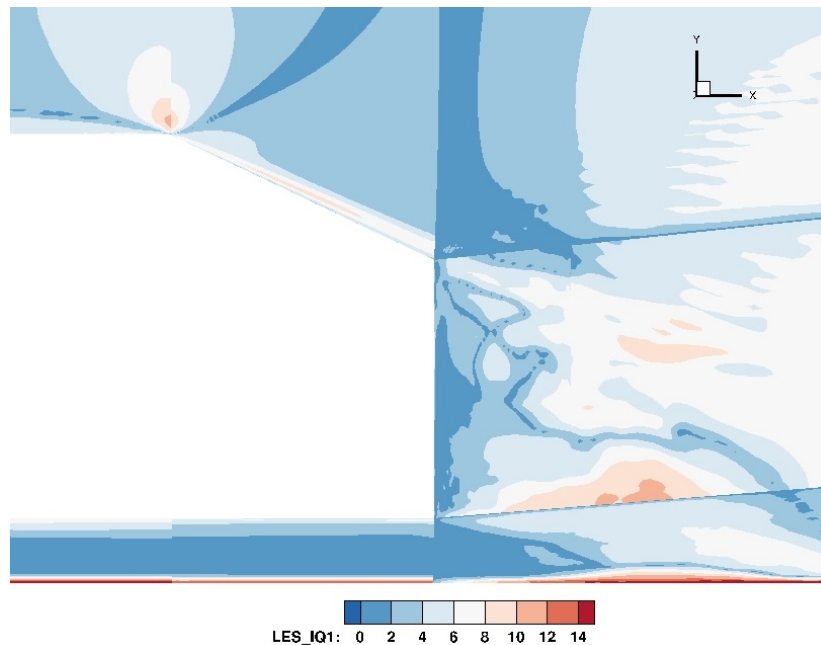
Figure 6.21 LES quality criteria evaluated based on grid width to Kolmogorov length scale ratio.

For the aeracoustic analysis of acoustic sources generated around the Ahmed body the SSV-PANS method is employed. By employing the hydrodynamic/acoustic splitting approach, as discussed in section 4.2, the SSV-PANS method effectively captured and analyzed acoustic waves, particularly in the near- and mid-field regions. This allowed for a comprehensive examination of flow characteristics across the Ahmed body, focusing on the generated acoustic sources in the near field. Additionally, observations were made by an observer positioned in the mid-field at a distance of $14L$, perpendicular to the flow direction.

To evaluate the performance of the SSV-PANS method, especially as the number of CVs
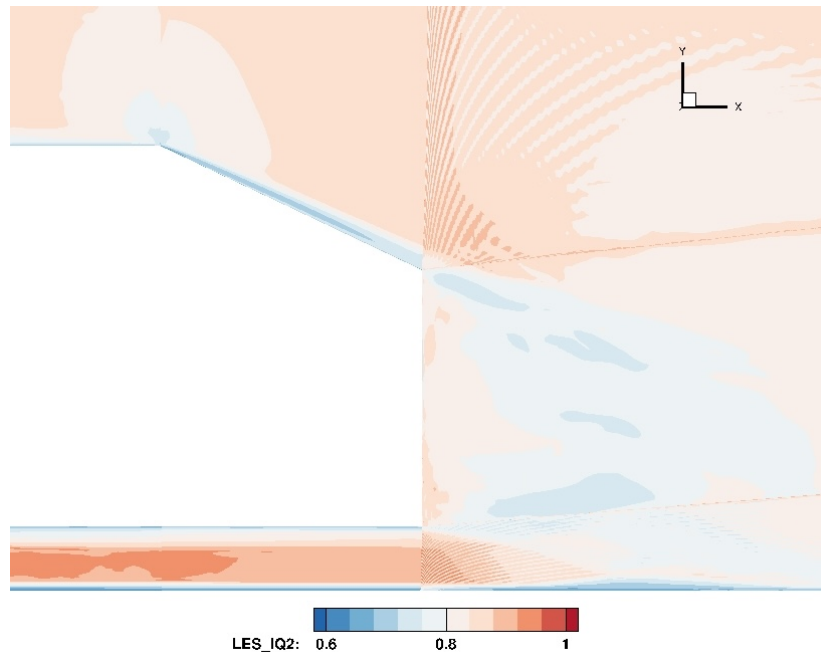
Figure 6.22 LES quality criteria evaluated based on Kolmogorov scale $LES - IQ_\eta$.

increased, a comparison was made with the more computationally intensive LES method. By utilizing a significantly larger number of CVs (48×10^6 CVs), the LES method served as a benchmark for assessing the accuracy and reliability of the SSV-PANS results. The acoustic sources obtained from the simulations, as depicted in Figure 6.23, played a crucial role in analyzing the acoustic behavior and characteristics of the flow around the Ahmed body using the SSV-PANS method.

Notably, Figure 6.23b illustrated the acoustic sources generated by the SSV-PANS method with 25×10^6 CVs. Impressively, these results exhibited a high level of similarity to the acoustic sources obtained from the LES method with 48×10^6 CVs (Figure 6.23c). This finding suggests that the SSV-PANS method, when appropriately configured with a sufficient number of CVs, can achieve comparable accuracy to the more computationally demanding LES method while offering improved computational efficiency.

On the other hand, the acoustic sources obtained with a lower number of CVs, specifically 14.5×10^6 CVs (Figure 6.23a), demonstrated slightly reduced accuracy compared to the LES results. This discrepancy indicates that a lower number of CVs may not fully capture the intricate flow and acoustic phenomena surrounding the Ahmed body, leading to some loss of fidelity in the simulation results.

Consequently, these findings underscore the critical significance of selecting an appropriate number of CVs in the SSV-PANS method to ensure the accurate representation of flow and acoustic phenomena. Increasing the number of CVs, as demonstrated by the comparison

between Figures 6.23a, 6.23b, and 6.23c, results in improved accuracy and reliability of the simulation outcomes.
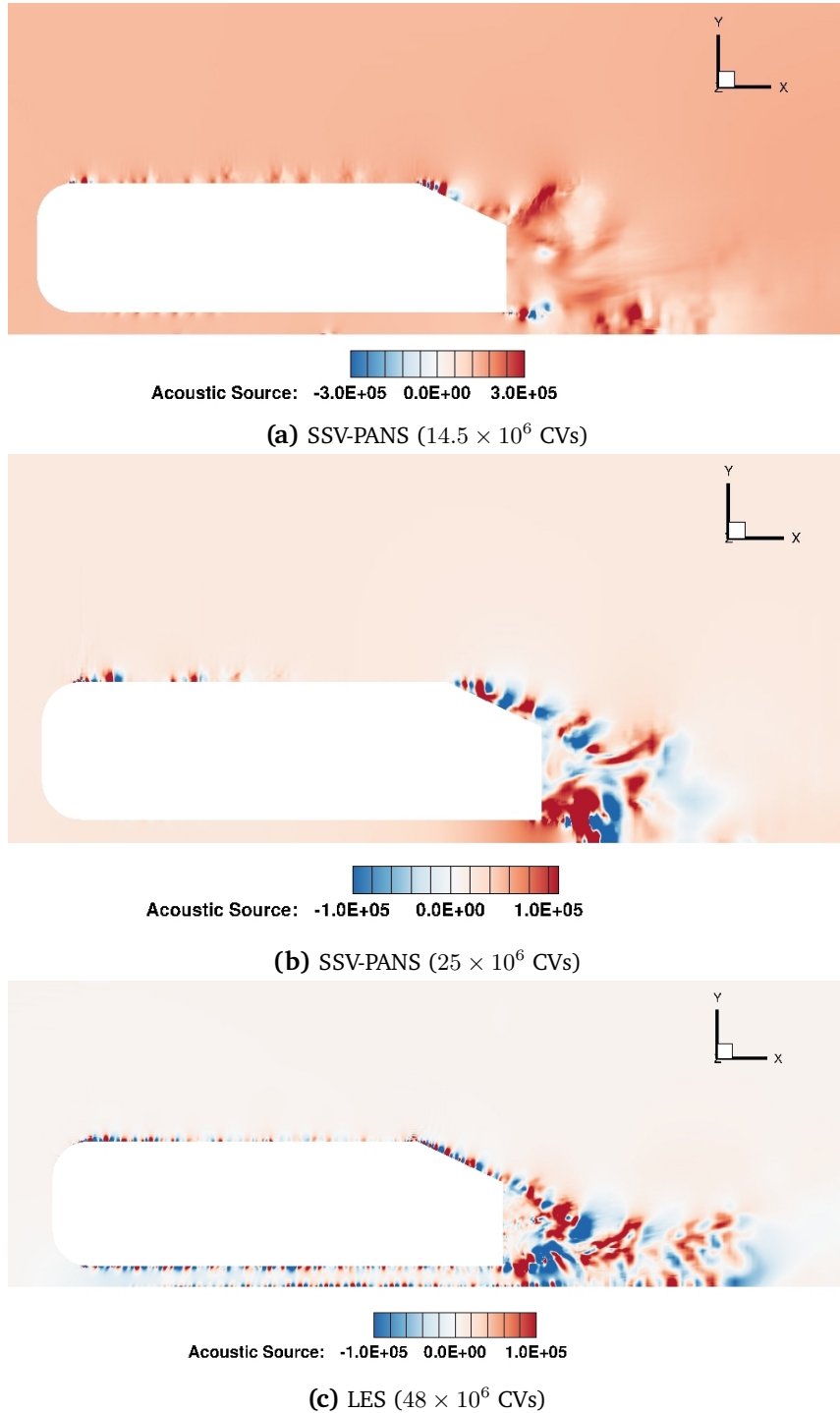

(a) SSV-PANS (14.5×10^6 CVs)

(b) SSV-PANS (25×10^6 CVs)

(c) LES (48×10^6 CVs)

Figure 6.23 Acoustic sources generated around the Ahmed body for different numbers of CVs obtained by SSV-PANS.

The comparison of Sound Pressure Level (SPL) between the SSV-PANS method and the LES method is depicted in Figure 6.24. This SPL comparison offers valuable insights into the distribution of peaks and harmonics in the acoustic field surrounding the Ahmed body.

In Figure 6.24a, corresponding to the coarse grid SSV-PANS method with 14.5 million CVs, some discrepancies in the results are observed. The peak locations exhibit a slight deviation, indicating limited accuracy in peak prediction. Additionally, the SPL value differs from the results obtained from the LES method. These discrepancies further suggest that the 14.5 million grid resolution may not capture the acoustic features with high precision.

However, Figure 6.24b, which corresponds to the medium grid SSV-PANS method with 25 million CVs, shows significant improvements. The peak locations are accurately predicted, and the SPL value demonstrates good agreement with the LES results. This indicates that increasing the number of CVs to 25 million provides better resolution and captures the acoustic features more accurately.

Table 6.7 presents a comparison of the Strouhal frequency among the different models. The results highlight that the SSV-PANS method with 25 million CVs provides a more accurate prediction of the Strouhal frequency compared to the case with 14.5 million CVs. The lower error for the 25 million CVs case, in comparison to the 14.5 million CVs case, demonstrates enhanced accuracy and closer agreement with the LES reference. These findings emphasize the importance of grid resolution in capturing the Strouhal frequency and validate the effectiveness of the SSV-PANS method in simulating complex aerodynamic phenomena.

These results suggest that increasing the grid resolution to 25 million CVs leads to a more accurate prediction of the Strouhal frequency. It is noteworthy that the sensitivity of the aeroacoustic behavior to grid refinement is higher than that of the hydrodynamic behavior. While the hydrodynamic results were satisfactory with the 14.5 million CVs , the aeroacoustic analysis highlights the importance of finer grid resolution. The improved accuracy and peak prediction achieved with the 25 million CVs demonstrate the significance of grid refinement in accurately capturing the intricate acoustic characteristics of the flow.

Table 6.7 Comparison of Strouhal frequency.

Model	CVs (million)	St	Error (%)
SSV-PANS	14	0.223	4.7
SSV-PANS	25	0.218	2.3
LES	48	0.213	-

Table 6.8 provides a comparison of the computational time among the different models. The results demonstrate that the computational time increases with the number of CVs, as expected. Specifically, the SSV-PANS method with 25 million CVs requires a longer computational time compared to the case with 14.5 million CVs. However, both SSV-PANS cases exhibit reduced computational times compared to the LES method. This highlights the advantage of the SSV-
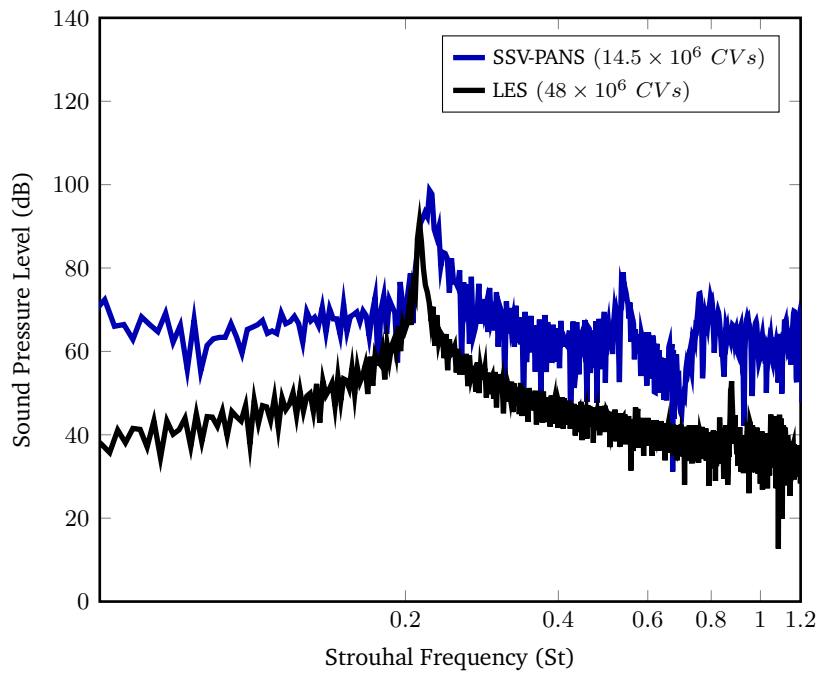
(a) SSV-PANS (14.5×10^6 CVs)
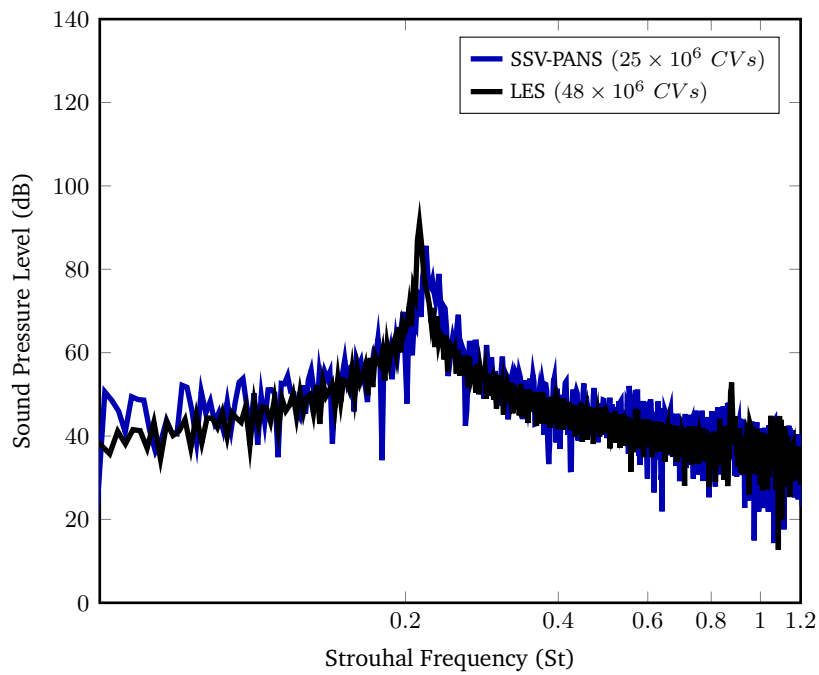
(b) SSV-PANS (25×10^6 CVs)

Figure 6.24 Sound Pressure Level (SPL) comparison of the SSV-PANS method with LES for different numbers of CVs obtained by SSV-PANS.

PANS method in achieving computational efficiency while maintaining reasonable accuracy in simulating the flow around the Ahmed body.

Table 6.8 Comparison of CV ratio and time ratio of SSV-PANS and LES.

Model	CVs (million)	Time ($core \times hour$)	CVs ratio	Time ratio
SSV-PANS	14.5	1079	0.29	0.43
SSV-PANS	25	1822	0.52	0.73
LES	48	2490.8	1.00	1.00

Furthermore, Figure 6.25 visually represents the computational ratios between the different models. The CV ratio and time ratio are depicted for each model. These findings underscore the computational efficiency of the SSV-PANS method while still maintaining acceptable accuracy, making it a viable option for aerodynamic simulations with limited computational resources.
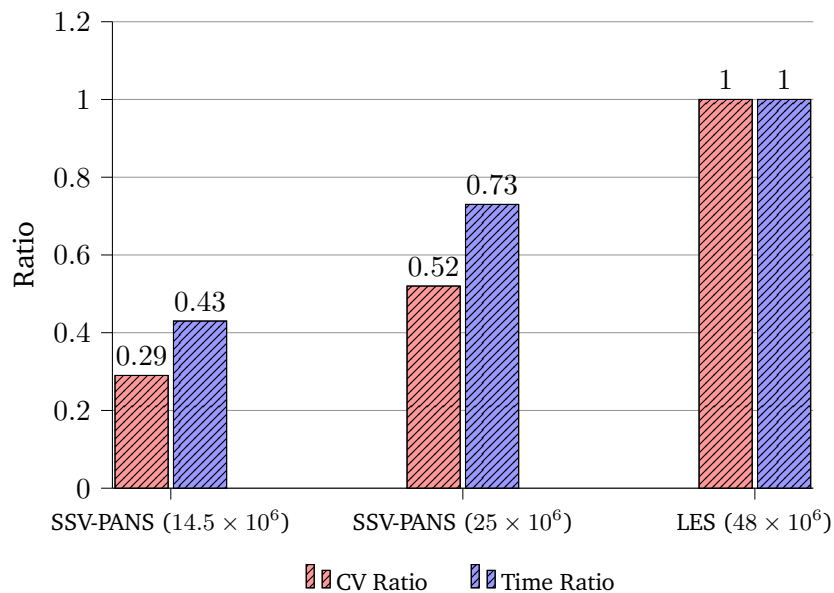
Figure 6.25 Comparison of CV ratio and time ratio of SSV-PANS and LES.

In summary, the application of the SSV-PANS method in aerodynamic and aeroacoustic analyses has been shown to be highly effective in capturing flow structures, accurately predicting aerodynamic forces, and reproducing acoustic sources for Ahmed body. The comparison of the SSV-PANS method with LES has validated its reliability, even when using coarser grid resolutions. However, the study has highlighted the significant impact of grid resolution on improving results.

7 Conclusions and Future Work

7.1 Summary

The study of aeroacoustics is crucial for understanding sound generation, propagation, and control in aerodynamic systems. This research focuses on analyzing the aerodynamic and aeroacoustic performance of the Partially-Averaged Navier-Stokes method utilizing the scale-supplying variable equation (SSV-SSV-PANS) , specifically for flow around circular cylinders and the Ahmed body. The SSV-PANS method, implemented in the FASTEST software, accurately captures complex flow phenomena and acoustic characteristics.

Benchmark cases of channel flow and 2D hill flow were chosen to assess the reliability and effectiveness of the SSV-PANS method. These cases provided well-documented experimental data, serving as reliable references for evaluating the accuracy and reliability of the simulations. By comparing the numerical results from the SSV-PANS method with experimental data and LES simulations, the performance of the SSV-PANS method in reproducing the hydrodynamic characteristics of these benchmark cases was evaluated.

The implemented SSV-PANS method in this research incorporates a hydrodynamic/acoustic splitting approach, allowing for the efficient and accurate simulation of hydrodynamic and acoustic phenomena separately. This approach aims to assess the effectiveness of the SSV-PANS method in capturing the characteristics of flow structures and acoustic behavior.

The first study analyzed the aeroacoustic performance of turbulent flow around a circular cylinder using the SSV-PANS and LES methods. The simulations used carefully designed grid configurations to ensure high resolution near the cylinder surface and in the wake region. The obtained results were compared with reference data, demonstrating the accuracy and effectiveness of the computational approach. The study also explored other methods to investigate flow characteristics, such as the combined splitting/Kirchhoff method and the long-span bodies method. By treating the acoustic field as a two-dimensional problem in the mid-span plane, computational costs were minimized without compromising accuracy. The study validated the results through comparisons of hydrodynamic quantities, confirming the accurate representation of flow dynamics. Increasing the number of control volumes improved flow visualization and enhanced the understanding of flow features. Sound pressure level (SPL) analysis showed strong agreement between the simulated and experimental data.

Furthermore, the study evaluated the computational efficiency of the SSV-PANS method, which demonstrated significant time reductions while maintaining accuracy. This study provided valuable insights into the aerodynamic and acoustic characteristics of flow around a circular cylinder, emphasizing the importance of grid refinement for accurate predictions.

The performance of the SSV-PANS method in capturing the aerodynamic and aeroacoustic behavior of the Ahmed body was also evaluated using two different grid resolutions: 14.5 million and 25 million control volumes (CVs). Remarkably, the SSV-PANS method demonstrated promising results at both resolutions, exhibiting good agreement in predicting the hydrodynamic field compared to experimental data and LES data. The SSV-PANS method demonstrated exceptional predictive capabilities in capturing flow separation over the slant of the Ahmed body. This aspect of its performance adds a crucial dimension to its effectiveness in reproducing complex aerodynamic phenomena. Considering the coarser resolution of 14.5 million CVs, the SSV-PANS method remained reasonably reliable in predicting the acoustic sources around the Ahmed body. It captured the generation and propagation of sound waves, providing fair acoustic predictions that aligned with LES data. However, some inaccuracies were observed in the aeroacoustic results with the coarser resolution, due to the limited spatial resolution of the grid. These limitations affected the representation of small-scale turbulence structures and their influence on noise generation. However, the medium grid SSV-PANS method with 25 million CVs demonstrated significant improvements. It accurately predicted the peak locations and exhibited good agreement in the SPL values with the LES results. Therefore, despite these observed limitations, the SSV-PANS method demonstrated its capability to accurately predict the aeroacoustic characteristics of the Ahmed body. The findings suggest that further refinement of the grid resolution could potentially enhance the accuracy of the results and provide even more reliable predictions for aeroacoustic analysis.

The results obtained from the benchmark cases emphasize the crucial role of grid resolution in accurately simulating complex aerodynamic phenomena. Higher grid refinement leads to improved prediction of the Strouhal frequency, which is essential for understanding flow dynamics. This finding emphasizes the significance of grid resolution in capturing intricate flow physics and underscores the importance of careful grid selection in aeroacoustic simulations.

One notable advantage of the SSV-PANS method is its computational efficiency compared to LES simulations. The reduced computational time required by the SSV-PANS method makes it particularly appealing for practical engineering applications with limited computational resources. Furthermore, the SSV-PANS method demonstrates reasonable accuracy in predicting flow structures and acoustic sources, positioning it as a promising tool for aerodynamic and aerodynamic-acoustic simulations.

In conclusion, this thesis has provided significant insights into the aerodynamic and aeroacoustic characteristics of flow around circular cylinders and the Ahmed body using the SSV-PANS method implemented in the FASTEST software. Through comprehensive comparisons with

experimental data and LES simulations, the accuracy and efficiency of the SSV-PANS method have been effectively demonstrated. The investigation of aeroacoustics, enabled by the SSV-PANS method implemented in the FASTEST software, contributes to the advancement of noise-reduction technologies with wide-ranging applications in industries such as transportation, energy, and aerospace. By improving our understanding of flow behavior and acoustic sources, this research paves the way for the development of more efficient and quieter systems in various engineering disciplines.

7.2 Outlook

The findings of this study open up opportunities for future advancements in aerodynamics and aeroacoustics based on insights gained from the implementation of the SSV-PANS method in the FASTEST software. Several key areas warrant further exploration and improvement, including:

Aeroacoustic Noise Reduction Strategies: Future research can explore novel strategies for mitigating noise based on the SSV-PANS method. This may involve optimizing geometries, implementing control techniques, or exploring new materials to reduce noise generation.

Multi-Objective Optimization: The computational efficiency and reasonable accuracy of the SSV-PANS method make it suitable for multi-objective optimization. Integrating optimization algorithms with SSV-PANS can lead to designs that optimize both aerodynamic performance and aeroacoustic noise reduction.

Practical Engineering Applications: The efficiency of the SSV-PANS method makes it valuable for real-world engineering applications, particularly in resource-limited contexts. Applying SSV-PANS to practical problems, such as vehicle design or wind turbines, and validating its performance in these scenarios will contribute to its wider adoption.

Experimental Validation and Validation Databases: Further experimental validation in benchmark cases and real-world scenarios can enhance the validation of the SSV-PANS method. Establishing comprehensive validation databases specific to aeroacoustic simulations will provide reliable references for assessing SSV-PANS accuracy and reliability.

Addressing these areas of future research will advance the accuracy, efficiency, and applicability of aerodynamics and aeroacoustics. The insights gained from this study, coupled with ongoing advancements in computational methods and experimental techniques, contribute to the development of noise-reducing technologies in various industries, ensuring a more sustainable and quieter future.

References

[1] "FASTEST-Manual ". In: *Fachgebiet für numerische Berechnungsverfahren im Maschinenbau, Technische Universität Darmstadt* (2005).

[2] P. Moin and J. Kim. *Fundamentals of Turbulent and Multi-Phase Combustion*. Cambridge University Press, 1998.

[3] P. Sagaut. *Large Eddy Simulation for Incompressible Flows: An Introduction*. Springer Science & Business Media, 2006.

[4] V. Voller and F. Porté-Agel. "Moore's law and numerical modeling ". In: *Journal of Computational Physics* 179.2 (2002), pp. 698–703.

[5] J. Smagorinsky. "General circulation experiments with the primitive equations: I. The basic experiment ". In: *Monthly Weather Review* 91.3 (1963), pp. 99–164.

[6] M. Germano, U. Piomelli, P. Moin, and W. H. Cabot. "A dynamic subgrid-scale eddy viscosity model ". In: *Physics of Fluids A: Fluid Dynamics* 3.7 (1991), pp. 1760–1765.

[7] O. Reynolds. "On the dynamical theory of incompressible viscous fluids and the determination of the criterion ". In: *Philosophical Transactions of the Royal Society of London A* 186 (1895), pp. 123–164.

[8] P. R. Spalart. "Comments on the feasibility of LES for wings, and on a hybrid RANS/LES approach ". In: *Proceedings of first AFOSR international conference on DNS/LES*. Greyden Press. 1997.

[9] M. Strelets. "Detached eddy simulation of massively separated flows ". In: *39th Aerospace sciences meeting and exhibit*. 2001, p. 879.

[10] C. Speziale. "Turbulence modeling for time-dependent RANS and VLES ". In: *AIAA journal* 36.2 (1998), pp. 173–184.

[11] P. Batten, U. Goldberg, and S. Chakravarthy. "Sub-grid turbulence modeling for unsteady flow with acoustic resonance ". In: *38th Aerospace Sciences Meeting and Exhibit*. 2000, p. 473.

[12] P. Batten, U. Goldberg, and S. Chakravarthy. "LNS-An approach towards embedded LES ". In: *40th AIAA Aerospace Sciences Meeting & Exhibit*. 2002, p. 427.

[13] S. Girimaji and K. Abdol-Hamid. "Partially-averaged Navier-Stokes model for turbulence: Implementation and validation ". In: *43rd AIAA Aerospace Sciences Meeting and Exhibit*. 2005, p. 502.

[14] S. S. Girimaji. "Partially-Averaged Navier-Stokes Model for Turbulence: A Reynolds-Averaged Navier-Stokes to Direct Numerical Simulation Bridging Method ". In: *Journal of Applied Mechanics* 73.3 (2005), pp. 413–421.

[15] S. Krajnović, R. Lárusson, and B. Basara. "Superiority of PANS compared to LES in predicting a rudimentary landing gear flow with affordable meshes ". In: *International Journal of Heat and Fluid Flow* 37 (2012), pp. 109–122.

[16] M. Mirzaei, S. Krajnović, and B. Basara. "Partially-Averaged Navier–Stokes simulations of flows around two different Ahmed bodies ". In: *Computers & Fluids* 117 (2015), pp. 273–286.

[17] B. Basara. "PANS method as a computational framework from an industrial perspective ". In: *Progress in Hybrid RANS-LES Modelling: Papers Contributed to the 5th Symposium on Hybrid RANS-LES Methods, 19-21 March 2014, College Station, A&M University, Texas, USA*. Springer. 2015, pp. 3–17.

[18] K. S. Abdol-Hamid and S. S. Girimaji. "A two-stage procedure toward the efficient implementation of PANS and other hybrid turbulence models ". In: (2004).

[19] H. Foroutan and S. Yavuzkurt. "A partially-averaged Navier–Stokes model for the simulation of turbulent swirling flow with vortex breakdown ". In: *International Journal of Heat and Fluid Flow* 50 (2014), pp. 402–416.

[20] R. Huang, X. Luo, B. Ji, and Q. Ji. "Turbulent flows over a backward facing step simulated using a modified partially averaged Navier–Stokes model ". In: *Journal of Fluids Engineering* 139.4 (2017).

[21] S. Lakshmipathy. *Partially averaged Navier-Stokes method for turbulence closures: characterization of fluctuations and extension to wall bounded flows*. Texas A&M University, 2009.

[22] D. Luo, C. Yan, H. Liu, and R. Zhao. "Comparative assessment of PANS and DES for simulation of flow past a circular cylinder ". In: *Journal of Wind Engineering and Industrial Aerodynamics* 134 (2014), pp. 65–77.

[23] S. Krajnović, G. Minelli, and B. Basara. "Partially-averaged Navier–Stokes simulations of two bluff body flows ". In: *Applied mathematics and computation* 272 (2016), pp. 692–706.

[24] S. Lakshmipathy and S. Girimaji. "Partially-averaged Navier-Stokes method for turbulent flows: kw model implementation ". In: *44th AIAA aerospace sciences meeting and exhibit*. 2006, p. 119.

[25] B. Basara, S. Krajnovic, S. Girimaji, and Z. Pavlovic. "Near-wall formulation of the Partially Averaged Navier Stokes turbulence model ". In: *AIAA journal* 49.12 (2011), pp. 2627–2636.

[26] B. Basara, Z. Pavlovic, and S. Girimaji. "A new approach for the calculation of the cut-off resolution parameter in bridging methods for turbulent flow simulation ". In: *International Journal of Heat and Fluid Flow* 74 (2018), pp. 76–88.

[27] M. J. Lighthill. "On sound generated aerodynamically I. General theory ". In: *Proceedings of the Royal Society of London. Series A. Mathematical and Physical Sciences* 211.1107 (1952), pp. 564–587.

[28] M. J. Lighthill. "On sound generated aerodynamically II. Turbulence as a source of sound ". In: *Proceedings of the Royal Society of London. Series A. Mathematical and Physical Sciences* 222.1148 (1954), pp. 1–32.

[29]   N. Curle. "The influence of solid boundaries upon aerodynamic sound ". In: *Proceedings of the Royal Society of London. Series A. Mathematical and Physical Sciences* 231.1187 (1955), pp. 505–514.

[30]   J. E. Ffowcs Williams and D. L. Hawkings. "Sound generation by turbulence and surfaces in arbitrary motion ". In: *Philosophical Transactions of the Royal Society of London. Series A, Mathematical and Physical Sciences* 264.1151 (1969), pp. 321–342.

[31]   C. Bogey, C. Bailly, and D. Juvé. "Noise investigation of a high subsonic, moderate Reynolds number jet using a compressible large eddy simulation ". In: *Theoretical and Computational Fluid Dynamics* 16 (2003), pp. 273–297.

[32]   H. M. Frank and C.-D. Munz. "Direct aeroacoustic simulation of acoustic feedback phenomena on a side-view mirror ". In: *Journal of sound and vibration* 371 (2016), pp. 132–149.

[33]   C. Bailly, C. Bogey, and O. Marsden. "Progress in direct noise computation ". In: *International Journal of Aeroacoustics* 9.1-2 (2010), pp. 123–143.

[34]   J. Hardin and D. Pope. "An acoustic/viscous splitting technique for computational aeroacoustics ". In: *Theoretical and computational fluid dynamics* 6.5 (1994), pp. 323–340.

[35]   J. E. Ffowcs Williams. "Hydrodynamic Noise ". In: *Annual Review of Fluid Mechanics* 1 (1969), pp. 197–222.

[36]   J. H. Seo and Y. J. Moon. "Aerodynamic noise prediction for long-span bodies ". In: *Journal of Sound and Vibration* 306.3-5 (2007), pp. 564–579.

[37]   W. Z. Shen and J. N. Sörensen. "Aeroacoustic modelling of low-speed flows ". In: *Theoretical and Computational Fluid Dynamics* 13.4 (1999), pp. 271–289.

[38]   W. Z. Shen and J. N. Sorensen. "Comment on the aeroacoustic formulation of Hardin and Pope ". In: *AIAA journal* 37.1 (1999), pp. 141–143.

[39]   C. Bailly and D. Juve. "A stochastic approach to compute subsonic noise using linearized Euler's equations ". In: *5th AIAA/CEAS aeroacoustics conference and exhibit*. 1999, p. 1872.

[40]   M. Kornhaas, M. Schäfer, and D. C. Sternel. "Efficient numerical simulation of aeroacoustics for low Mach number flows interacting with structures ". In: *Computational Mechanics* 55.6 (2015), pp. 1143–1154.

[41]   C. Wagner, T. Hüttl, and P. Sagaut. *Large-Eddy Simulation for Acoustics*. Cambridge: Cambridge University Press, 2007.

[42]   R. Langtry, E. Gren, J. Larssen, and P. Spalart. "Evaluation of structured and unstrucutred grids for detached eddy simulation of flap edge noise ". In: *15th AIAA/CEAS Aeroacoustics Conference (30th AIAA Aeroacoustics Conference)*. 2009, p. 3102.

[43]   G. Kirchhoff. "Zur Theorie der Lichtstrahlen ". In: *Annalen der Physik* 254.4 (1883), pp. 663–695.

[44]   E. Manoha, C. Herrero, S. Ben Khelil, P. Guillen, P. Sagaut, and I. Mary. "Numerical prediction of airfoil aerodynamic noise ". In: *8th AIAA/CEAS Aeroacoustics Conference & Exhibit*. 2002, p. 2573.

[45] E. Kolb and M. Schäfer. "Aeroacoustic simulation of flexible structures in low Mach number turbulent flows ". In: *Computers & Fluids* 227 (2021), p. 105020.

[46] M. Schäfer. *Computational engineering: Introduction to numerical methods*. Vol. 321. Springer, 2006.

[47] J. H. Ferziger and M. PeriC. *Computational methods for fluid dynamics*. Springer, 2002.

[48] M. Kornhaas. "Effiziente numerische Methoden für die Simulation aeroakustischer Probleme mit kleinen Machzahlen ". PhD thesis. Technische Universität Darmstadt, 2011.

[49] X. Gloerfelt. "Cavity noise ". In: *VKI Lecture series: Aerodynamic noise from wall-bounded flows*. 2009.

[50] O. Reynolds. "XXIX. An experimental investigation of the circumstances which determine whether the motion of water shall be direct or sinuous, and of the law of resistance in parallel channels ". In: *Philosophical Transactions of the Royal society of London* 174 (1883), pp. 935–982.

[51] S. B. Pope and S. B. Pope. *Turbulent flows*. Cambridge university press, 2000.

[52] D. C. Wilcox. *Turbulence modeling for CFD*. Vol. 2. DCW industries La Canada, CA, 1998.

[53] J. Piquet. *Turbulent flows: models and physics*. Springer Science & Business Media, 2001.

[54] R. D. Moser, J. Kim, and N. N. Mansour. "Direct numerical simulation of turbulent channel flow up to $Re_\tau = 590$ ". In: *Physics of fluids* 11.4 (1999), pp. 943–945.

[55] A. N. Kolmogorov. "The local structure of turbulence in incompressible viscous fluid for very large Reynolds numbers ". In: *Proceedings of the Royal Society of London. Series A: Mathematical and Physical Sciences* 434.1890 (1991), pp. 9–13.

[56] T. Kármán. "Mechanische Änlichkeit und Turbulenz ". In: *Nachrichten von der Gesellschaft der Wissenschaften zu Göttingen, Mathematisch-Physikalische Klasse* 1930 (1930), pp. 58–76.

[57] J. W. Deardorff. "A numerical study of three-dimensional turbulent channel flow at large Reynolds numbers ". In: *Journal of Fluid Mechanics* 41.2 (1970), pp. 453–480.

[58] M. Breuer. "Numerical and modeling influences on large eddy simulations for the flow past a circular cylinder ". In: *International Journal of Heat and Fluid Flow* 19.5 (1998), pp. 512–521.

[59] J. Meyers and P. Sagaut. "On the model coefficients for the standard and the variational multi-scale Smagorinsky model ". In: *Journal of Fluid Mechanics* 569 (2006), pp. 287–319.

[60] D. K. Lilly. "A proposed modification of the Germano subgrid-scale closure method ". In: *Physics of Fluids A: Fluid Dynamics* 4.3 (1992), pp. 633–635.

[61] J. Boussinesq. *Essai sur la théorie des eaux courantes*. Impr. nationale, 1877.

[62] P. Spalart and S. Allmaras. "A one-equation turbulence model for aerodynamic flows ". In: *30th aerospace sciences meeting and exhibit*. 1992, p. 439.

[63] B. E. Launder and B. I. Sharma. "Application of the energy-dissipation model of turbulence to the calculation of flow near a spinning disc ". In: *Letters in heat and mass transfer* 1.2 (1974), pp. 131–137.

[64] W. P. Jones and B. E. Launder. "The prediction of laminarization with a two-equation model of turbulence ". In: *International journal of heat and mass transfer* 15.2 (1972), pp. 301–314.

[65] F. Menter. "Zonal two equation $k - \omega$ turbulence models for aerodynamic flows ". In: *23rd fluid dynamics, plasmadynamics, and lasers conference*. 1993, p. 2906.

[66] F. R. Menter. "Two-equation eddy-viscosity turbulence models for engineering applications ". In: *AIAA journal* 32.8 (1994), pp. 1598–1605.

[67] M. Popovac and K. Hanjalic. "Compound wall treatment for RANS computation of complex turbulent flows and heat transfer ". In: *Flow, turbulence and combustion* 78 (2007), pp. 177–202.

[68] K. Hanjalić, M. Popovac, and M. Hadžiabdić. "A robust near-wall elliptic-relaxation eddy-viscosity turbulence model for CFD ". In: *International Journal of Heat and Fluid Flow* 25.6 (2004), pp. 1047–1051.

[69] R. Manceau, J. P. Bonnet, and J. J. Chattot. "A partially-averaged Navier–Stokes approach for turbulence ". In: *Journal of Turbulence* 13.37 (2012), pp. 1–28.

[70] P. R. Spalart, W. H. Jou, M. K. Strelets, and S. R. Allmaras. "Comments on the feasibility of LES for wings, and on a hybrid RANS/LES approach ". In: *In Advances in DNS/LES* (2009), pp. 137–148.

[71] P. R. Spalart. "Detached-eddy simulation ". In: *Annual review of fluid mechanics* 41 (2009), pp. 181–202.

[72] F. Menter and Y. Egorov. "The scale-adaptive simulation method for unsteady turbulent flow predictions. Part 1: theory and model description ". In: *Flow, turbulence and combustion* 85.1 (2010), pp. 113–138.

[73] P. Spalart, S. Deck, M. Shur, K. Squires, and M. Strelets. "A new version of detached-eddy simulation, resistant to ambiguous grid densities ". In: *Theoretical and Computational Fluid Dynamics* 20.3 (2006), pp. 181–195.

[74] J. Fröhlich and D. Von Terzi. "Hybrid LES/RANS methods for the simulation of turbulent flows ". In: *Progress in Aerospace Sciences* 44.5 (2008), pp. 349–377.

[75] S. S. Girimaji, R. Srinivasan, and E. Jeong. "PANS turbulence model for seamless transition between RANS and LES: fixed-point analysis and preliminary results ". In: *Fluids Engineering Division Summer Meeting*. Vol. 36975. 2003, pp. 1901–1909.

[76] S. Girimaji and B. Basara. "Modelling the cut-off scale supplying variable in bridging methods for turbulence flow simulation ". In: *Proc. of 4th Int. Conference on Jets, Wakes and Separated Flows*. Vol. 2013.4. 2013, pp. 1099-1-1099–6.

[77] H. Versteeg and W. Malalasekera. *An Introduction to Computational Fluid Dynamics: The Finite Volume Method*. Pearson Education Limited, 2007.

[78]   B. P. Leonard. "A stable and accurate convective modelling procedure based on quadratic upstream interpolation ". In: *Computer methods in applied mechanics and engineering* 19.1 (1979), pp. 59–98.

[79]   A. Harten. "High resolution schemes for hyperbolic conservation laws ". In: *Journal of computational physics* 135.2 (1997), pp. 260–278.

[80]   P. K. Sweby. "High resolution schemes using flux limiters for hyperbolic conservation laws ". In: *SIAM journal on numerical analysis* 21.5 (1984), pp. 995–1011.

[81]   B. Leonard. "Locally modified QUICK scheme for highly convective 2-D and 3-D flows ". In: *Numerical methods in laminar and turbulent flow* 5 (1987), pp. 35–47.

[82]   P. Gaskell and A. Lau. "Curvature-compensated convective transport: SMART, a new boundedness-preserving transport algorithm ". In: *International Journal for numerical methods in fluids* 8.6 (1988), pp. 617–641.

[83]   T. Reimann. "Numerische Simulation von Fluid-Struktur-Interaktion in turbulenten Strömungen ". de. PhD thesis. TU Darmstadt, 2013.

[84]   R. J. LeVeque. *Finite volume methods for hyperbolic problems*. Vol. 31. Cambridge university press, 2002.

[85]   E. F. Toro. *Riemann solvers and numerical methods for fluid dynamics: a practical introduction*. Springer Science & Business Media, 2013.

[86]   E. Kolb. "Aeroacoustic Simulation of Turbulent Fluid-structure Interactions at Low Mach Numbers ". PhD thesis. Technische Universität Darmstadt, 2022.

[87]   R. J. LeVeque. "Wave propagation algorithms for multidimensional hyperbolic systems ". In: *Journal of computational physics* 131.2 (1997), pp. 327–353.

[88]   C. Kato, A. Iida, Y. Takano, H. Fujita, and M. Ikegawa. "Numerical prediction of aerodynamic noise radiated from low Mach number turbulent wake ". In: *31st aerospace sciences meeting*. 1993, p. 145.

[89]   A. A. Oberai, F. Roknaldin, and T. J. Hughes. "Computation of trailing-edge noise due to turbulent flow over an airfoil ". In: *AIAA journal* 40.11 (2002), pp. 2206–2216.

[90]   R. Ewert and W. Schröder. "Acoustic perturbation equations based on flow decomposition via source filtering ". In: *Journal of Computational Physics* 188.2 (2003), pp. 365–398.

[91]   The MathWorks Inc. *MATLAB version 9.5.0 (R2018b)*. The MathWorks Inc. Natick, Massachusetts, U.S.A., 2018.

[92]   X. Gloerfelt, C. Bailly, and D. Juvé. "Direct computation of the noise radiated by a subsonic cavity flow and application of integral methods ". In: *Journal of sound and vibration* 266.1 (2003), pp. 119–146.

[93]   K. Iwamoto, Y. Suzuki, and N. Kasagi. "Reynolds number effect on wall turbulence: toward effective feedback control ". In: *International journal of heat and fluid flow* 23.5 (2002), pp. 678–689.

[94]   J. Fröhlich, C. P. Mellen, W. Rodi, L. Temmerman, and M. A. Leschziner. "Highly resolved large-eddy simulation of separated flow in a channel with streamwise periodic constrictions ". In: *Journal of Fluid Mechanics* 526 (2005), pp. 19–66.

[95] M. C. Jacob, J. Boudet, D. Casalino, and M. Michard. "A rod-airfoil experiment as a benchmark for broadband noise modeling ". In: *Theoretical and Computational Fluid Dynamics* 19.3 (2005), pp. 171–196.

[96] W. K. Blake. "Mechanics of flow-induced sound and vibration. Volume 1 General concepts and elementary source. Volume 2-Complex flow-structure interactions ". In: *Aplikace Matematiky, Applied Mathematics* 1 (1986).

[97] S. Szepessy and P. Bearman. "Aspect ratio and end plate effects on vortex shedding from a circular cylinder ". In: *Journal of Fluid Mechanics* 234 (1992), pp. 191–217.

[98] A. Moosavifard, E. Kolb, M. Schäfer, and S. Jakirlic. "Investigation of the PANS Method for the Prediction of Aerodynamic Noise Around a Circular Cylinder ". In: *8th European Congress on Computational Methods in Applied Sciences and Engineering*. 2022.

[99] S. R. Ahmed, G. Ramm, and G. Faltin. "Some salient features of the time-averaged ground vehicle wake ". In: *SAE Transactions* (1984), pp. 473–503.

[100] *ERCOFTAC Ahmed Body EST Case*. URL: https://www.kbwiki.ercoftac.org/w/index.php/Abstr:Ahmed_body.

[101] S. Jakirlic, R. Jester-Zürker, and C. Tropea. "9th ERCOFTAC/IAHR ". In: *COST workshop on refined turbulence modelling*. 2001, pp. 36–43.

[102] ERCOFTAC (SIG-15), IAHR, and QNET-CFD. *Report on the 10th joint ERCOFTAC (SIG-15)/IAHR/QNET-CFD Workshop on Refined Turbulence Modelling*. Technical report. Poitiers, France, 2002.

[103] H. Lienhart, C. Stoots, and S. Becker. "Flow and turbulence structures in the wake of a simplified car model (ahmed modell) ". In: *New results in numerical and experimental fluid mechanics III*. Springer, 2002, pp. 323–330.

[104] E. Serre, M. Minguez, R. Pasquetti, E. Guilmineau, G. B. Deng, M. Kornhaas, M. Schäfer, J. Fröhlich, C. Hinterberger, and W. Rodi. "On simulating the turbulent flow around the Ahmed body: A French–German collaborative evaluation of LES and DES ". In: *Computers & Fluids* 78 (2013), pp. 10–23.

[105] I. B. Celik, Z. N. Cehreli, and I. Yavuz. "Index of Resolution Quality for Large Eddy Simulations ". In: *Journal of Fluids Engineering* 127.5 (Sept. 2005), pp. 949–958.